INVESTIGATING THE SIZE EFFECT IN SENB SPECIMENS WITH A TRIAXIALITY AND LODE ANGLE BASED DAMAGE MODEL

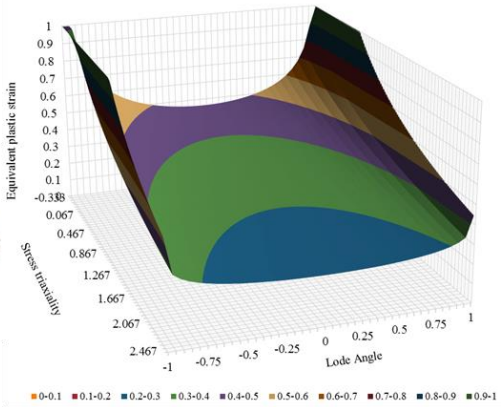

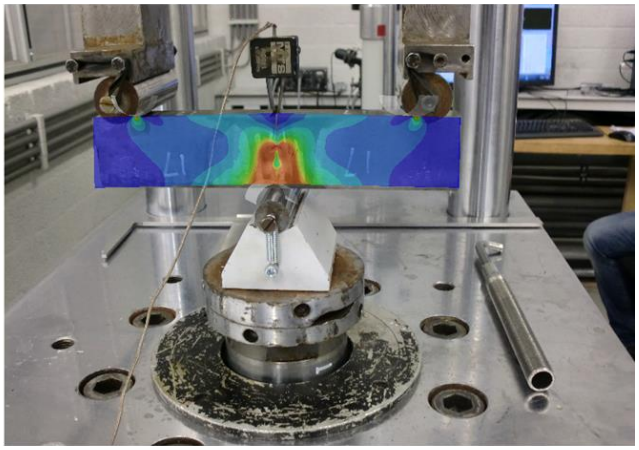

Okko Coppejans
TU Delft & TNO

INVESTIGATING THE SIZE EFFECT IN SENB SPECIMENS WITH A TRIAXIALITY AND LODE ANGLE BASED DAMAGE MODEL

By

Okko Jan Coppejans

in partial fulfilment of the requirements for the degree of

Master of Science
in Civil Engineering

at the Delft University of Technology,
to be defended publicly on 31-8-2017.

Supervisor:	Prof. dr. L.J. Sluys,	TU Delft
Thesis committee:	Dr. C. Kassapoglou,	TU Delft
	Dr. V. Popovich,	TU Delft
	Dr. C.L. Walters,	TNO

SUMMARY / ABSTRACT

This master thesis is built up around two questions. First: Is it possible to calibrate a ductile failure model, where the strain at failure is a function of stress triaxiality and Lode angle, using only a single SENB specimen? The failure model that is referred to describes local failure in a finite element model to simulate ductile fracture. In this thesis, an orthotropic damage constitutive material model is constructed to accommodate the most realistic fictitious crack growth. Simple isotropic element erosion or deletion was found to have severe effects on the stress states of neighbouring elements due to a major loss of constraint. The damage model is based on the stress triaxiality and Lode angle, derived from the invariants of the stress tensor. For any combination of stress triaxiality and Lode angle, an equivalent plastic strain to failure is required in the form of a three-dimensional failure surface. Typically, multiple experiments with varying dominant stress states are needed to accurately calibrate such a failure surface or model. This research project shows that one can not only calibrate a failure surface from a single three-point bending specimen, but also obtains more calibration points than other approaches that are typically used for this purpose along the way. These calibration points are collected during a fully automated iterative procedure, where points are added every time the force in the simulation exceeds the force found in the experiment by more than 1%. As soon as enough calibration points with distinct stress states were found, the Hosford-Coulomb model was fitted using the least squares method. Finally, the obtained failure model was verified by using it to simulate the specimen on which it was calibrated. From these results, it can be concluded that it is possible to calibrate a failure model using only a single SENB specimen. In addition to this thesis, this procedure is outlined in a paper (Coppejans & Walters, 2017).

The second part of the thesis revolves around whether a ductile failure model obtained from the procedure presented in this thesis can be successfully used to predict failure in different geometries. To verify this, the differences in stress states that occur in specimens with different dimensions and aspect ratios is researched both theoretically and numerically. From that study, it is found that indeed the geometry has an influence on the stress states that are present and where they are present. This influence is great enough that simple fracture mechanics approaches such as the *J*-Integral and CTOD are only transferable if strict requirements are met between SENB specimen from the same material but with different dimensions. Standards such as BS7448 and ASTM E1820 describe the validity of the experimentally obtained fracture toughness parameters with respect to the specimen size to deal with these requirements. Where the global approach (fracture mechanics) fails, the local approach (damage mechanics) finds a natural application due to its revolving around stress states. Application of the failure model obtained from the smallest specimen to the specimen with greater size and to the specimen with a different aspect ratio strengthens this claim. The failure model is able to predict the onset of element failure, used to simulate crack growth, within 2.5% deviation in experimental and simulated force at crack initiation. The force during crack propagation is simulated with 99% accuracy for crack mouth opening diameters (CMOD) at least twice and up to four times the CMOD due to plastic deformation. For greater amounts of CMOD, the reaction force is simulated with decreasing accuracy. The crack path on the free surface is verified by comparing the simulated crack path, visualised by removing all damaged elements from view, to a picture that was taken after the experiment. This reveals that while the extent of the crack is fairly accurately simulated, the width of the crack is both not accurately represented by simply removing all damaged elements from view, and the created damage model may require more development.

ACKNOWLEDGEMENTS

This entire thesis was fully supported by the department of Structural Dynamics of TNO in Delft. TNO provided the resources to carry out the experiments that are used in this thesis, as well as many knowledgeable people and a great graduation environment. Special thanks go out to Dr. Carey Walters, my supervisor at TNO, for taking good care of me at TNO, being an indispensable source of knowledge and a fair critic of my comma abuse in writing.

Secondly, it has to be mentioned that this work draws from an earlier thesis by Nii Dagadu, who showed that it is possible to set up a (semi)-automated calibration procedure using Matlab and Abaqus. While the procedure in this thesis has been programmed from scratch, Mr. Dagadu's insights provided the fundamentals that were of great help.

My professor, Bert Sluys, has been of great help during the many input sessions that shape the goal and overall direction of my thesis. Prof. Sluys has had a great amount patience during the slow process that was my thesis.

Thanks also go out to the other people in my committee, Dr. Christos Kassapoglou and Dr. Vera Popovich for the great feedback. Lars Voormeeren was of great help during the beginning of my thesis and most progress meetings.

TABLE OF CONTENTS

LIST OF TABLES

List of Figures

LIST OF APPENDICES

1 INTRODUCTION

This chapter outlines the motivation behind this research project, the scope wherein it is carried out and the research questions that are posed.

1.1 Motivation

Describing ductile crack growth in steel has been a topic for decades. For safety reasons, it is important that local failure does not immediately result in collapse of the structure. In pressure vessels and pipes, the leak-before-break methodology works with the assumption that a leak must occur before the entire structure fails. For this, an accurate description of the effect of a small crack on the load bearing capacity is created. This can then be used to provide information about the maximum size of i.e. a fatigue crack, before this crack propagates and results in structural failure. Naturally, this knowledge can be used both in design of new structures, as well as lifetime assessment of existing structures to ensure safety. Accurate characterisation of crack initiation and propagation has therefor major consequences for both finance and safety of existing and new structures. Analyses of ductile fracture was at first dominated by approaches that globally describe the fracture toughness of materials. The field of fracture mechanics is concerned with finding the fracture toughness parameters. Fracture toughness parameters such as the stress intensity factor (K), energy release rate and J-integral are dependent on the stress fields that exist near the crack front. Consequently, these parameters are dependent on the geometry of the specimen from which it was measured, as well as the way this specimen was loaded. Standards describe the validity of experimentally found fracture toughness parameters for structures. Mainly in the last two decades, focus shifted from two-dimensional to three-dimensional modelling of fracture. With the addition of this third dimension and the stress states that result from this, the demand for fracture toughness parameters that are valid for more states than plane stress and plane strain increased. Stress state dependent fracture toughness formulations were conceived, such as the J-Q and J-A_2 theory. On the other hand, increased computer power allows scientists to use techniques like continuum damage mechanics to simulate crack growth on a local level in three dimensions. In the continuum damage mechanics approach taken here, the plastic strain to failure is a function of the stress state of an element. To find the material calibration parameters of the function that accurately describes the relation between plastic failure strain and stress state, a considerable amount of experiments has to be carried out with different dominant stress states. This expensive way of finding the material parameters is the motivation for this thesis. It is known that in a single edge notched bending (SENB) specimen, failure occurs during many different stress states as the crack progresses. Through accurate inverse engineering of crack growth in such a specimen using finite element analysis, a plethora of stress states and their respective failure strain can be found. Inverse engineering one SENB experiment thusly results in a complete failure

model, considerably reducing the cost of the experiments compared to previous methods. Whether the obtained failure model can be used to predict failure in different geometries is also tested in this thesis to examine the validity of the obtained failure model.

1.2 Scope

The main themes in this thesis are on one hand the calibration procedure and on the other hand the size effect in SENB specimens. Size effect refers to the effect of the geometry to the stress states present in the model and consequently the effect of the size on crack initiation and propagation as modelled using the Finite Element Method (FEM). This effect is studied both theoretically and numerically. To get the most realistic crack-tip behaviour in terms of stress states, a custom continuum damage model is introduced. Developing this orthotropic damage model was at first not in the scope of the thesis, as its necessity became apparent only when the isotropic damage model was found to lack realistic simulation of a crack. The softening function belonging to this damage model is briefly introduced, but this tangential subject is covered no further.
This thesis is focussed on finding and applying failure criteria describing ductile fracture. While there is some attention given to deriving the plasticity model from a tensile test, the isotropic Von Mises model is assumed to correctly describe plasticity in this material even though these specimens originate from a rolled plate.
In order to obtain the plastic stress-strain characteristic, tensile tests were performed. The Force-CMOD data of the SENB specimens was obtained by doing three experiments for three different geometries of SENB specimen. The experiments were carried out at Element material labs in Breda and were observed by the author. The material that is used throughout the thesis, is Weldox 700, a structural steel conforming to the S690 standard. For every experiment, Force-CMOD data is available to a CMOD of approximately 7mm. This was the maximum extension of the clip gage and is also used as the maximum for the simulations.

1.3 Sub questions

Answering the main question relies on an accurate description of the stress states around the crack tip, and therefore it is necessary to review the effect of the specimen size on the stress states around the crack tip. This is done both theoretically, in chapter 3, and experimentally using the finite element method (chapter 6 and 7). Using both existing theory and detailed modelling can shed a light on the first two sub questions:

How does the size of the specimen effect the stress triaxiality and Lode parameter at the crack tip?
How does the size of the specimen effect the stress ahead of the crack tip?

Strong stress gradients are present near the crack tip, due to excessive straining and crack blunting. In order to accurately capture these gradients, a large number of finite elements might be required. Whether this is feasible, is the motivation behind the third sub question:
Is it feasible to use a mesh so fine that the high stress gradients near the crack tip are accurately captured?

The way crack growth is modelled, using methods belonging to the domain of continuum damage mechanics, relies on a well-motivated damage description. The discretisation of this problem using finite elements creates a certain amount of artificial effects on the stress states around a growing crack. Crack growth through damage, as well as two ways this can be accomplished, are reviewed based on observations and their effect on the elements surrounding a damaged element. This review is then used to answer the following sub-questions, which can help determine the validity of the approach taken in this model:
Is the continuum damage approach variant that is used here appropriate for the simulation of fracture in SENB specimen?
Is it possible to accurately simulate tunnelling and shear lips with this damage mechanics model?

1.4 Main question

The sub questions are used to help answer the main question, presented here, and provide guidance and limitations. The final goal of this research project is to answer the following question:

Is a stress triaxiality, Lode angle and plastic strain based failure model, calibrated from a single SENB specimen, able to correctly predict failure in different sized SENB specimen?

This can be split in two parts:

1. Is it possible to calibrate a failure model, where the strain at failure is a function of stress triaxiality and Lode angle, using only a single SENB specimen?
2. Is this failure model able to correctly predict crack growth in SENB specimen with different geometries?

Correct crack growth prediction is defined in the following ways:

1. No or small differences between the force-CMOD measured in the experiment and the simulation.
2. Agreement between the crack path in the experiment and simulation.

The failure model is used to model element failure and therefor the prediction of failure is the prediction of element failure.

2 THEORETICAL BACK-GROUND

Starting from a basic notion of mechanics and exploring fundamental material models to ending with the method of continuum damage mechanics, this chapter covers the theoretical background with which this thesis is written.

2.1 Basic notions in solid mechanics

In order to establish the terms, conventions and abbreviations later used in this thesis, a short introduction into solid mechanics is given. The starting point is an arbitrary body or volume (V) in the XYZ coordinate system as shown in Figure 2-1. This volume is subjected to body forces (f_b) and surface forces (f_s). The volume is constrained by boundary conditions (S_d).

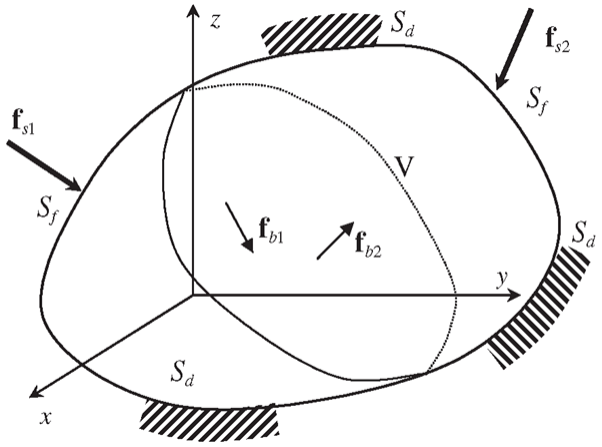

Figure 2-1 An arbitrary three-dimensional body

In this volume, an infinitesimal cube is considered such as in Figure 2-2. When such a cube is subjected to a force on one of its faces, stress is defined as the force subjected to the face divided by the area of face. The main challenge in solid mechanics is to find the deformation of a body subjected to a force. In Figure 2-2, the stress components for every direction in the XYZ coordinate system are shown.

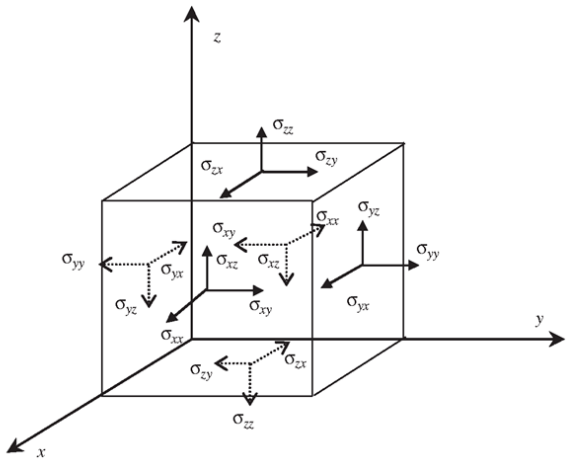

Figure 2-2 Stress components in a three-dimensional body

Shear forces (forces that are applied parallel to a face) result in shear stresses. Shear stresses are denoted with mixed indices (such as σ_{xy}), where the first index indicates the normal of the face which is considered and the second index indicates the direction of the shear stress on that face. Normal stresses (such as σ_{xx}) follow that same convention and are stresses that act perpendicular to the considered face.

The stress tensor is a second order tensor Σ, which describes the state of stress of the element, and has the following form in matrix notation:

$$\Sigma = \begin{bmatrix} \sigma_{xx} & \sigma_{xy} & \sigma_{xz} \\ \sigma_{yx} & \sigma_{yy} & \sigma_{yz} \\ \sigma_{zx} & \sigma_{zy} & \sigma_{zz} \end{bmatrix} \quad (2.1)$$

In such an infinitesimal and static element, moment equilibrium applies. The application of this equilibrium results in the conclusion that not all stresses are independent of each other. This can be summarised by stating that since the body is not rotating nor translating, all moments and forces must be in equilibrium. The moment equilibrium then dictates that the shear stresses σ_{xy}, σ_{yz} and σ_{xz} must be equal to respectively σ_{yx}, σ_{zy} and σ_{zx}. This means that the matrix $\sum$ is symmetric. From this symmetric stress tensor $\sum$, a few things must be considered. First of all, the values in this stress tensor are dependent on the coordinate system. Secondly, it can be noted that the cube can undergo a change in volume as well as a change of shape. The part of the stresses that cause a change of volume is referred to as the volumetric or hydrostatic stress and can be calculated from the normal stresses with the formula below:

$$\mathrm{p} = -\frac{\sigma_{xx} + \sigma_{yy} + \sigma_{zz}}{3} = -\sigma_{mean} \quad (2.2)$$

When the hydrostatic stress is subtracted from the normal stresses, the deviatoric part of the stress component remains. The deviatoric part is defined as the part of the stress that causes a change in shape and is written using the matrix notation of S in equation (2.3).

$$\Sigma = \begin{bmatrix} \sigma_{xx} & \sigma_{xy} & \sigma_{xz} \\ \sigma_{yx} & \sigma_{yy} & \sigma_{yz} \\ \sigma_{zx} & \sigma_{zy} & \sigma_{zz} \end{bmatrix} \quad \text{with } s_{ii} = \sigma_{ii} + p \quad for\ i = [x, y, z] \quad (2.3)$$

Even now, the coordinate system still defines the values of the deviatoric stress components. From linear algebra, it is known that for the stress tensor in(2.4), the following must be true, where λ represents the eigenvalues or principal stresses and I represents the identity matrix.

$$det\left(\begin{bmatrix} \sigma_{xx} & \sigma_{xy} & \sigma_{xz} \\ \sigma_{yx} & \sigma_{yy} & \sigma_{yz} \\ \sigma_{zx} & \sigma_{zy} & \sigma_{zz} \end{bmatrix} - \lambda I\right) = 0 \quad (2.4)$$

For the stress tensor displayed in(2.4) the eigenvalues can be calculated using the following formulae:

$$\lambda^3 - I_1\lambda + I_2\lambda^2 - I_3 = 0 \quad (2.5)$$

$$I_1 = \sigma_{xx} + \sigma_{yy} + \sigma_{zz} \quad (2.6)$$

$$I_2 = \sigma_{xx}\sigma_{yy} + \sigma_{yy}\sigma_{zz} + \sigma_{zz}\sigma_{xx} - \sigma_{xy}^2 - \sigma_{yz}^2 - \sigma_{zx}^2 \quad (2.7)$$

$$I_3 = \sigma_{xx}\sigma_{yy}\sigma_{zz} + 2\sigma_{xy}\sigma_{yz}\sigma_{zx} - \sigma_{zz}\sigma_{xy}^2 - \sigma_{xx}\sigma_{yz}^2 - \sigma_{yy}\sigma_{zx}^2 \quad (2.8)$$

Important to note here is that the equations in(2.5)-(2.8) together form nothing more than the determinant of (2.3) and therefore must hold for any chosen coordinate system. The values of I_1, I_2 and I_3 are respectively called the first, second and third invariant of the stress tensor. As the name suggests, these values are invariant to the chosen reference coordinate system. Likewise can be done for the deviatoric stress tensor S.
In the calculation of the deviatoric stress tensor and its eigenvalues, the first deviatoric invariant is not present by definition. The second and third invariant of the deviatoric stress tensor are formulated by:

$$\lambda^3 - J_2\lambda - J_3 = 0 \quad (2.9)$$

$$J_2 = s_{xx}s_{yy} + s_{yy}s_{zz} + s_{zz}s_{xx} - s_{xy}^2 - s_{yz}^2 - s_{zx}^2 \quad (2.10)$$

$$J_3 = s_{xx}s_{yy}s_{zz} + 2\sigma_{xy}\sigma_{yz}\sigma_{zx} - s_{zz}\sigma_{xy}^2 - s_{xx}\sigma_{yz}^2 - s_{yy}\sigma_{zx}^2 \quad (2.11)$$

The third invariant of the stress tensor is a recurring quantity in this thesis and is used as a basic quantity in the material model. The principal stresses, or eigenvalues, of the stress matrix in (2.3)are the stresses that are by definition independent of the coordinate system. The eigenvectors belonging to these eigenvalues have the physical meaning of the direction of the principal stresses.
Like the stress tensor, one can define the strain tensor. The strain tensor consists of values that signify the deformations of the same infinitesimal cube shown in the beginning of this paragraph. As stated before, the challenge is to relate the response of a body to the force exerted on that body. More directly, this means that the relation between the strain tensor and stress tensor is needed. The relations between stress and strain are known as the constitutive equations and are briefly discussed in the next paragraph on material models.

2.2 Material models

In this paragraph, the material models used in this thesis are discussed starting from a basic linear elastic isotropic model and concluding with the plasticity model.

2.2.1 Isotropic and linear elastic

The simplest constitutive model is the isotropic linear elastic model following Hooke's law. A constitutive model relates the stresses and strains in a body, which in a more physical sense means that it represents the behaviour of a specific material. Many different materials exist, but with the assumption that a material can be modelled with an isotropic linear model two material parameters are required. In this research, the material parameters for this linear isotropic material model, are the Young's modulus E and the viscosity ν. According to Hooke's law, the relations between the stresses and strains in an isotropic linear elastic material model are presented in the following way. μ and λ are the Lamé parameters.

$$\sigma_t^{trial} = \begin{bmatrix}\sigma_{xx}^t\\ \sigma_{yy}^t\\ \sigma_{zz}^t\\ \sigma_{xy}^t\\ \sigma_{yz}^t\\ \sigma_{zx}^t\end{bmatrix} = \begin{bmatrix}\sigma_{xx}^{t-\Delta t}\\ \sigma_{yy}^{t-\Delta t}\\ \sigma_{zz}^{t-\Delta t}\\ \sigma_{xy}^{t-\Delta t}\\ \sigma_{yz}^{t-\Delta t}\\ \sigma_{zx}^{t-\Delta t}\end{bmatrix} + \begin{bmatrix}\lambda+2\mu & \lambda & \lambda & & & \\ \lambda & \lambda+2\mu & \lambda & & & \\ \lambda & \lambda & \lambda+2\mu & & & \\ & & & \mu & & \\ & & & & \mu & \\ & & & & & \mu\end{bmatrix}\begin{bmatrix}\Delta\varepsilon_{xx}^t\\ \Delta\varepsilon_{yy}^t\\ \Delta\varepsilon_{zz}^t\\ \Delta\varepsilon_{xy}^t\\ \Delta\varepsilon_{yz}^t\\ \Delta\varepsilon_{zx}^t\end{bmatrix} \quad (2.12)$$

This can also be presented as $\varepsilon = C^e\sigma$, where C^e is the compliance matrix. The relationship between strains as a function of stresses in (2.12) can also be inverted to relate the stresses as functions of strains. The inverse compliance matrix carries the name stiffness matrix (D). Since an isotropic material is assumed, the compliance and stiffness matrices are both symmetric. When the values of the Young's modulus and Poisson's ratio are considered constant, a linear relation exists between stresses and strains in the model and therefore also between forces and displacements in the body. In this thesis steel is used, which can be modelled as an isotropic material and as an elastically linear material until some point. As with most transformations, in reality, there is no such point, but within a small interval, the material behaviour changes from elastic to plastic. This transition is commonly referred to as yielding of the material. In the elastic stage, the material returns to its original shape after being deformed by a force, whereas when the material is loaded into its plastic stage, permanent deformation ensues. To accurately describe this behaviour, the

relation between stresses and strains in the plastic stage must be derived, as well as a function for the onset of yielding.

2.2.2 Plasticity modelling

The modelling of plasticity is an enormous field of study, which is not the focus of this work. For the sake of clarity in this thesis, the important concepts are explained briefly in this paragraph.
The yield function, which was briefly mentioned in the last paragraph, describes the state of stress which marks the end of elastic behaviour. When considering the elementary cube from paragraph 2.1, the state of stress is described by the stress tensor $\sum$, and a certain combination of those components describes a stress state at which yield occurs. In the 19th century, the French engineer Henri Tresca laid the groundwork for the field of plasticity in ductile materials. After extensive experiments, he discovered that the onset of yield occurred due to a maximal shear stress being reached in a ductile material such as steel. The criterion was appropriately named the maximum shear criterion and is more commonly known the Tresca criterion. Looking at the principal stresses in the two-dimensional stress space (where σ_3=0), Tresca states that any combination of stresses σ_1 and σ_2 that lies within the shape circumscribed by the dotted line is not in yield. Conversely, any combination that lies outside the shape is said to be in yield. In Figure 2-3, both Tresca's yield criterion and Von Mises' yield criterion are shown. Tresca's yield function is clearly not continuous, whereas the latter is. This property gives the Von Mises criterion a distinct advantage in computational elastic-plasticity, where the normal to the yield contour becomes important in a process called return mapping.

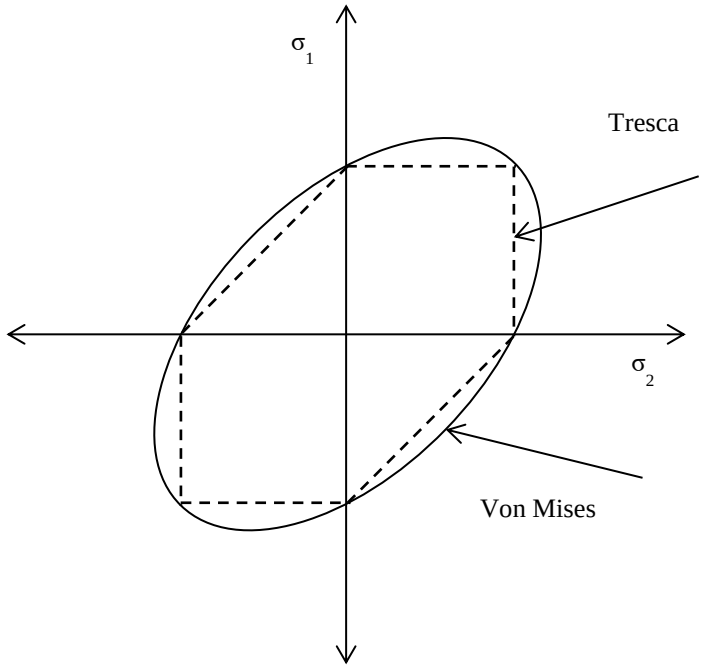

Figure 2-3 Yield contours of Tresca's and Von Mises' criterion in 2D

Both the Von Mises and Tresca yield function are said to be pressure independent yield criteria, which means that yielding depends on a combination of the deviatoric stresses only. The Von Mises yield criterion can be expressed most compactly as either a function of the principal stresses or the second invariant of the deviatoric stresses (derived in paragraph 2.1). In equation (2.13) and (2.14), both equivalent formulas that form the Von Mises yield criterion are displayed.

$$\sqrt{\frac{(\sigma_1-\sigma_2)^2+(\sigma_2-\sigma_3)^2+(\sigma_3-\sigma_1)^2}{2}} = \sigma_Y \qquad (2.13)$$

$$\sqrt{3J_2} = \sigma_Y \qquad (2.14)$$

In the latter equation, the second invariant of the deviatoric stresses (J_2) is used, which has led to naming it the J_2 flow theory. In this thesis, the Von Mises yield criterion is used. The Von Mises yield criterion can be used because the steel used in this thesis is assumed to be an isotropic material. The SENB specimen and tensile tests were machined from the same plate, and the orientations of the specimens with respect to

the plate were identical. For this reason, any anisotropy that may be introduced by the rolling process has the same effect on all specimen.

2.3 Damage mechanics

In this paragraph, a brief introduction is given to continuum damage mechanics in this model and the combination with element deletion.

It is customary for phenomenological damage models for metals to work with a modified stress space, known as the Haigh-Westergaard or Lode stress space. This stress space is derived from the stress space of principal stresses, but instead of using a Cartesian coordinate system (σ_1,σ_2,σ_3), the cylindrical Haigh-Westergaard or Lode coordinate system (z,r,θ) is used. Like the principal stresses, the parameters that make up the Lode coordinate system are deviatoric invariants. The value of the axial coordinate z can be seen as the magnitude of the orthogonal projection of the stress state onto the hydrostatic axis. The radial coordinate r is the magnitude of the orthogonal projection of the stress state onto the deviatoric plane, and the angular coordinate θ is a certain ratio of the second and third deviatoric stress invariant. These three parameters are detailed in equation (2.15),(2.16) and (2.17).

$$z = \frac{I_3}{\sqrt{3}} \tag{2.15}$$

$$r = \sqrt{2J_2} \tag{2.16}$$

$$\theta = \frac{J_3}{2} * \left(\frac{3}{J_2}\right)^{\frac{3}{2}} \tag{2.17}$$

With the introduction of the stress triaxiality parameter η, defined in derivation (2.19) as the ratio between the mean stress and the von Mises stress, the coordinates r and z can be expressed in the following way:

$$\bar{\sigma} = \sigma_{mises} = \sqrt{3J_2} \quad \xrightarrow{yields} \quad J_2 = \frac{\bar{\sigma}^2}{3} \tag{2.18}$$

$$\eta = \frac{\sigma_{mean}}{\bar{\sigma}} = \frac{I_1}{3\bar{\sigma}} \tag{2.19}$$

$$z = \frac{I_1}{\sqrt{3}} = \sigma_{mean}\sqrt{3} = \sqrt{3}\eta\bar{\sigma} \tag{2.20}$$

$$r = \sqrt{2J_2} = \sqrt{\frac{2}{3}} * \bar{\sigma} \tag{2.21}$$

These new definitions of axial coordinate, z, and radial coordinate, r, allow the stress state to be defined with parameters η, θ and σ_{mises}. In consideration of the damage model that is used here, the failure stress of a material can be expressed as a function of stress triaxiality and Lode angle. Additionally, the von Mises stress at failure can be directly related to the strain, since the von Mises plasticity model is used. This allows the failure strain to be a function of stress triaxiality and Lode angle, which is very convenient in this research. The introduction of the normalised Lode angle $\bar{\theta}$ reduces the range of the angle to -1 and 1, which too will be convenient later in this research.

$$\bar{\theta} = 1 - \frac{2}{\pi}\arccos\left(\frac{3\sqrt{3}}{2} * \frac{J_3}{J_2^{3/2}}\right) \tag{2.22}$$

A physical representation of the relation between the two coordinate systems is shown in Figure 2-4. This coordinate system using η, θ and σ_{mises} is called the modified Haigh-Westergaard coordinate system.

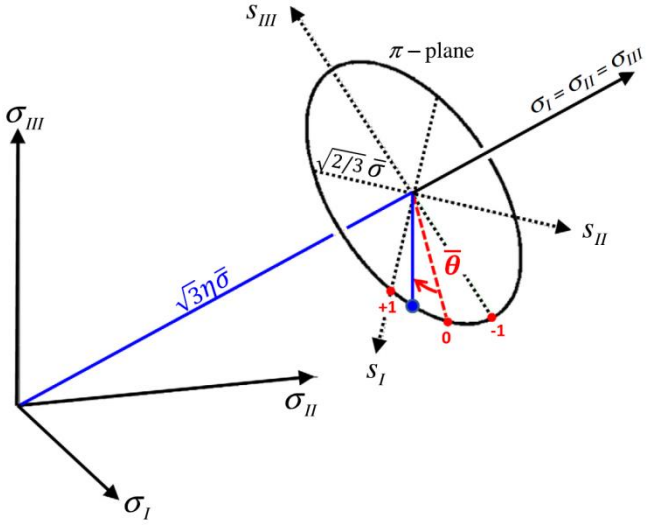

Figure 2-4 Principal stress space in Cartesian coordinates and Lode coordinates for $\sigma_1>\sigma_2>\sigma_3$. Image by (Mohr & Marcadet, 2015)

In Figure 2-5, the common stress states are shown in the Lode angle-stress triaxiality space.

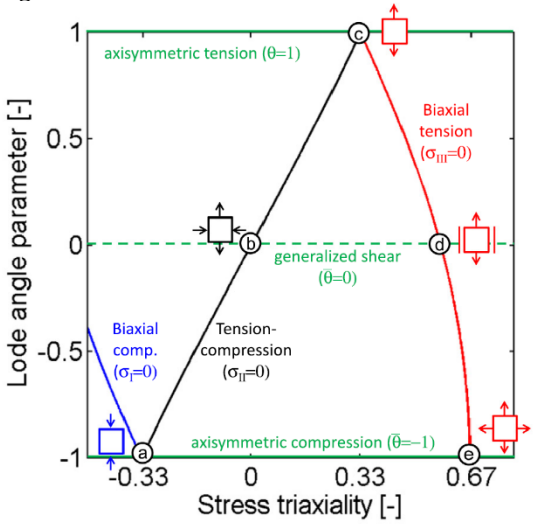

Figure 2-5 Common stress states in the Haigh-Westergaard coordinate system, from (Mohr & Marcadet, 2015). (a) uniaxial compression, (b) pure shear, (c) uniaxial tension, (d) plane strain tension, (e) equibiaxial tension.

In continuum damage mechanics, the material history has an influence on the stress evolution, much like in plasticity. In this thesis, the damage is applied using the formulation of the effective stress tensor for isotropic damage postulated by Lemaitre and Chaboche in 1978, presented in equation (2.23).

$$\sigma_{eff} = w \cdot \sigma \qquad \text{(Lemaitre \& Chaboche, 1978)} \qquad (2.23)$$

This way of applying damage is suited for use in ductile failure and is based on the hypothesis of strain equivalence formulated by Lemaitre and Chaboche. (Murakami, 2012)

> *Hypothesis of Strain Equivalence*
> *The inelastic constitutive equation of a damaged material is given by the corresponding constitutive equation for an undamaged material by replacing the stress tensor σ in the equation with the corresponding effective stress tensor σ_{eff}. (Lemaitre & Chaboche, 1978)*

The implementation in the material subroutine is presented in Chapter 6.

3 DUCTILE CRACK GROWTH AND CRACK TIP STRESS STATES

The process of ductile crack growth is of great importance in the fracture behaviour assessment of structures. Existing fatigue cracks can extend by ductile crack growth and reduce the bearing capacity of the structures. Furthermore, ductile crack growth can promote the transition to a more unstable form of crack growth, such as cleavage or brittle failure in the ductile to brittle transition region. In this chapter, the process of ductile crack growth is briefly explained and is followed by a discussion of the stress states near the crack tip.

3.1 Ductile crack growth

The process of ductile crack growth, in a microscopic framework, is commonly characterised by three main stages.

1. Nucleation of microscopic voids at inclusions or material impurities.
2. Growth of the microscopic voids through plastic straining.
3. Coalescence of microscopic voids form a new crack path.

These processes, and the influence of the stress and strain state of the element on these processes, have been extensively researched in the past. When looking at ductile crack growth within a framework of stress and strain state of elements, crack growth is ultimately caused by plastic straining. As such, it is common to use maximum plastic strain as a failure parameter. But, as can be seen from the stages of ductile crack growth, the entire process depends on more than plastic straining. (Bridgman, 1952) was the first to relate the plastic strain to failure to the stress triaxiality, a parameter then mainly influences the nucleation of voids. This was later analytically modelled by (McClintock, 1968). Both the stress triaxiality and the plastic strain are high in front of the crack tip, which causes the void nucleation, void growth, and coalescence to be concentrated in front of the crack tip. It was found by (Rice & Tracey, 1969) that, in addition to stress triaxiality, another parameter influences the growth of ductile cracks. This other parameter is known as the Lode angle, and together with the stress triaxiality and plastic strain to failure, they characterise the stress state of an isotropic material in terms of invariants. However, the influence of the Lode angle was marked as insignificant by Rice and Tracey and was dismissed. Many years later, (Xue, 2007) revisited the effect of the Lode angle and showed that it could have a significant effect on the strain to failure.

3.1.1 Stress states and crack growth from a fracture mechanics point of view

In the field of fracture mechanics, the fracture toughness of a material is characterised by, until recently, a single parameter. The origin of fracture mechanics dates to the early 20th century, and a brief overview is given to show the important assumptions and their flaws.

Early on, fracture mechanics was limited to linear elastic fracture mechanics (LEFM). The fracture toughness was at that time formulated as the energy release rate by (Griffith, 1920). Griffith considered an energy balance in a material flaw using the first law of thermodynamics. A flaw develops into a crack when the energy that is released from an increment in crack growth is great enough to overcome the surface energy of a material. While his energy release rate worked great for glass and perfect brittle materials, attempts to

use it on metals were unsuccessful. This was because of the energy balance being limited to the surface energy of the material, while for metals a great amount of energy is dissipated in plastic flow. (Irwin, 1956) incorporated plastic flow and later related it to the stress intensity factor K (Irwin, 1957) based on work of (Westergaard, 1939). Among others, Westergaard, Irwin and (Williams, 1957) published analytical solutions of the stress field ahead of the crack tip for a geometry such as shown in Figure 3-1.

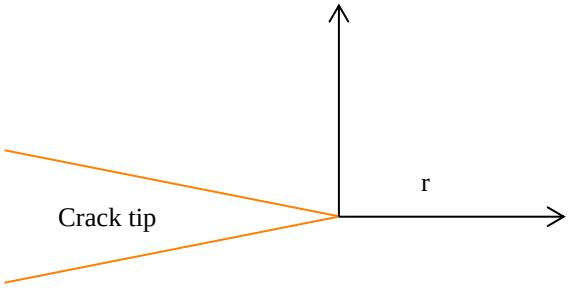

Figure 3-1 Crack tip as assumed in LEFM for plane strain (mode 1) crack loading

Assuming isotropic linear behaviour, Williams showed that the stress field at the crack tip as a function of distance r can be expressed as an infinite series with a leading term proportional to $1/\sqrt{r}$, a second term independent of r, followed by more terms dependent on r. This representation of the stress field creates a singularity in r=0, and in classical fracture mechanics, all terms except the singular are neglected. The second term in this series however does not reduce to 0 near the crack tip and influences the stresses in the plastic zone. In fracture mechanics, this term is referred to as the T-stress. The T stress provides a better insight in the stability of a crack in linear elastic materials. It was found that for small amounts of crack growth, a straight crack path remained straight for values of $T<0$, while for $T>0$, the crack will be unstable and deviate from being straight (Cotterell & Rice, 1980).
In case of plasticity, it was found that the crack tip was not sharp anymore but was blunted as shown in Figure 3-2 and the LEFM approach was no longer valid.

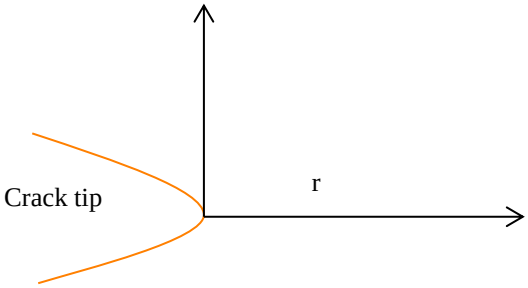

Figure 3-2 Blunted crack tip due to plastic deformation

What followed was corrections for small scale plasticity to the LEFM model and (Wells, 1961) developed a parameter called the Crack Tip Opening Displacement (CTOD or δ), which uses the displacement of the crack faces. A few years later (Hutchinson, 1968) and (Rice & Rosengren, 1968) developed a theory relating the dominant term of the singularity field near the crack tip to the J-integral for plane strain mode-I cracks (Rice J. , 1968). This solution became known as the HRR solution and the stress field corresponding to this solution is known as the HRR field. The J-integral is based on the idealisation of plastic deformations as nonlinear elastic deformations. The HRR solution predicts infinite stresses at r=0, just like the solution that Williams proposed using LEFM. However, the blunted crack tip can be seen as a free surface and therefore it stands to reason that at least the stress with normal r should reduce to 0 at r=0. The HRR solution is valid only for small scale plasticity and blunting of the crack tip results in strains outside of this assumption. Using finite elements with large strain formulation, it was shown that the actual stress state deviates from the HRR solution due to crack blunting (McMeeking & Parks, 1979). The results that McMeeking and Parks obtained is presented alongside with the HRR field in Figure 3-3. In this graph, it can be seen that the maximum stress occurs at a distance of ~2δ, with δ being the CTOD as hypothesized by Wells. This solution becomes of importance when establishing the mesh size of a finite element model of the fracture specimen and is discussed in paragraph 5.2.2. From the work of McMeeking and Parks it can be

concluded that the maximum stress triaxiality can be found not at the border of the crack tip, but at some distance from that tip.
As an intermezzo, it is important to examine the different kinds of crack loading that is commonly referred to in fracture mechanics. The fracture toughness parameters K, J and CTOD, as well as the stress state characterisation parameter T and Q, assume a state of plane strain. K is often used with a subscript denoting the cracking mode for which it was established. K_I refers to the stress intensity found for mode I cracking, which corresponds to an opening crack under plane strain loading conditions. A crack subjected to in-plane shear forces is said to undergo mode II loading of the crack and finally there is mode III loading of a crack, which corresponds to a crack driven by out of plane shear (tearing). These modes rarely occur in practice on their own, but many experiments can be characterised by a combination of 2 or 3 of these modes. This too applies to the Single Edge Notched Beam (SENB) experiments that are used in this thesis, where a combination of plane strain (mode I) and out-of-plane shear cracking (mode III) is found.

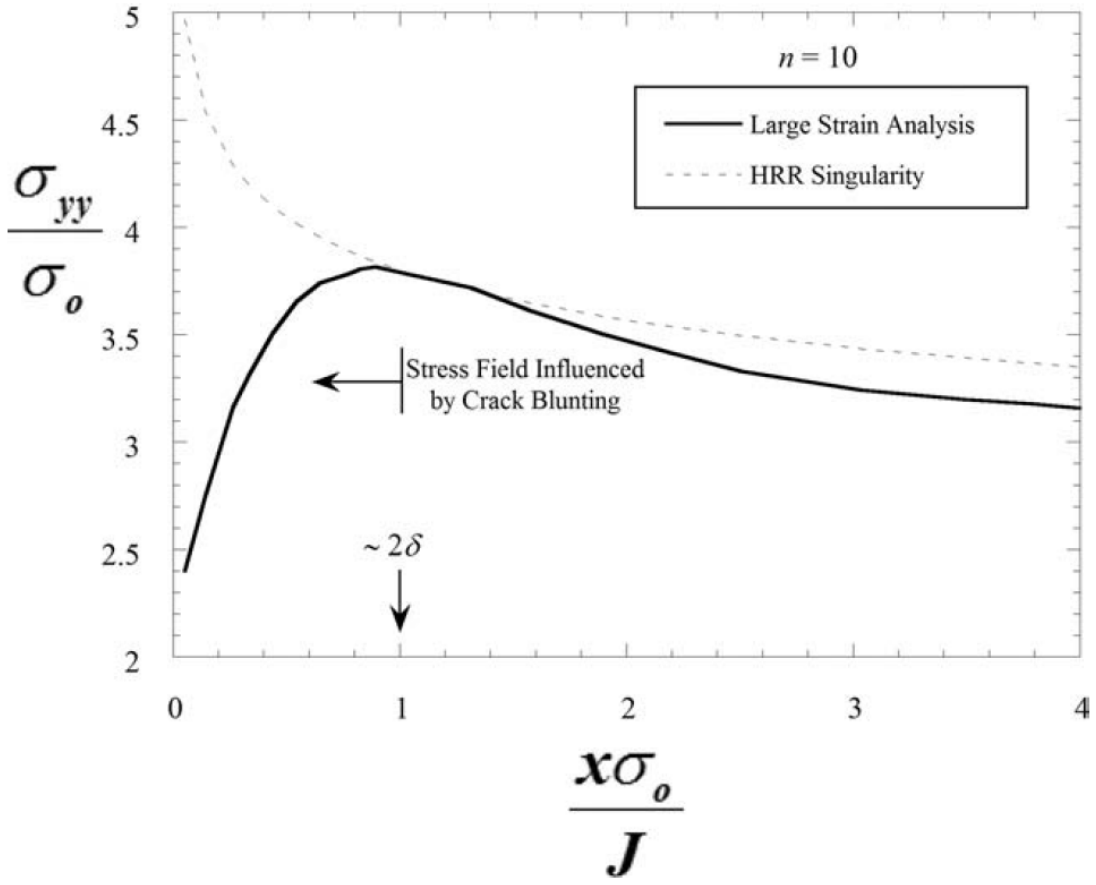

Figure 3-3 Large strain analysis of the stress field near the crack tip using FEM compared with the HRR field. (McMeeking & Parks, 1979)

The T-stress, which was discussed briefly in the context of LEFM, also plays a role in elastic-plastic fracture mechanics. (Larsson & Carlsson, 1973) and (Rice J. , 1974) showed that the T-stress has an effect of the plastic zone size and shape in small scale yielding (SSY). Furthermore, they found that through including the T-stress, small plastic zones found in actual specimen can be predicted. That the T-stress also had a strong effect on the stress triaxiality, was first shown by (Bilby, Goldthorpe, & Howard, 1986) for a non-hardening material. (Betegón & Hancock, 1991), (Du & Hancock, 1991) and (Parks, 1991) gave further insight in the correlation between stress triaxiality and the T-stress. It was found that the stress triaxiality ahead of the crack tip can be reduced by a negative T-stress. A positive T-stress, on the other hand, indicates a high stress triaxiality and it was found that in this case the crack-tip field can be accurately described by the HRR field. This also means that the fracture toughness can be accurately described by the J-integral in this case. Consequently, a two-parameter characterisation of the fracture toughness, by a combination of T-

stress and the J-integral was born (Betegón & Hancock, 1991). (Tvergaard & Hutchinson, 1994) found that from measured values of J, the fracture toughness increases for increasingly negative values of the T-stress. Increasing computer power in the 1990's enabled (Nakamura & Parks, 1990) to do detailed finite element analysis on thin cracked panels. In these panels, the crack front field was dominated by the plane strain solution only when the loads were very small. In other cases, the plane-stress solution dominated the field if the in-plane dimension of the plastic zone was larger than 1.5 times the panel thickness. These findings suggest that the effect of plane stress like fields cannot be neglected for thin cracked specimen under large plastic deformations. Moreover, the results from (Nakamura & Parks, 1990) showed that the crack front fields are significantly different from the plane strain SSY solution.
For large scale yielding (LSY), the use of the T-stress and J-Integral as a two-parameter fracture toughness characterisation is less successful. The T-stress is derived from a purely elastic framework and works in combination with the HRR field. Higher order terms, dependent on r, where neglected. These higher order terms form a group that can be called a difference field. The amplitude of that difference field corresponds to a uniform hydrostatic shift of the stress field in front of the crack tip. (O'Dowd & Shih, 1991,1992) named this amplitude the Q parameter, and with the relation between the constraint and Q, the J-Q theory was born. This Q parameter is a direct measure of the stress triaxiality. Even with the Q parameter, in bending specimens that experience large scale yielding, the J-Q solution loses validity. This is due to the global bending influence that occurs only under fully plastic conditions (O'Dowd & Shih, 2002).

3.1.2 Constraint

In this short intermezzo, the use of the constraint and its relation to T-stress, Q and stress triaxiality is given. It is important to note that constraint and triaxiality are not the same thing. Constraint can best be described as a structural resistance, caused by geometry, against plastic deformation. Consequently, stress triaxiality, T-stress and the Q parameter are effects of the constraint of the specimen or structural component. For the sake of clarity and in preparation for the size effect discussion, it is necessary to distinguish the in-plane constraint and out-of-plane constraint. The in-plane constraint is caused by the length of the ligament, or the dimension in the direction where the crack grows. Additionally, it can be influenced by the loading of the specimen (bending or tension) and crack depth. The out of plane constraint is affected by the specimen thickness, or more specifically, the dimension parallel to the crack. It can also be effected by tension in the direction of the crack tip, such as in biaxial loading conditions. The influence of the free surface is very important in the aspect of three-dimensional crack fields, as was pointed out by (Rice J. , 1974).

3.2 Size effect in SENB specimen

The effect of the cross-sectional size in a SENB (Single Edge Notched Beam) specimen is discussed in this chapter. Investigating the size effect in SENB specimen is not a new topic of research when looking at fracture mechanics and the relation of fracture mechanics parameters such as the CTOD and the J-integral. The experiment itself is further explained in Chapter 5.1, while the theoretical background for the size effect of SENB experiments is discussed in this paragraph. A SENB specimen is schematically shown in Figure 3-4.

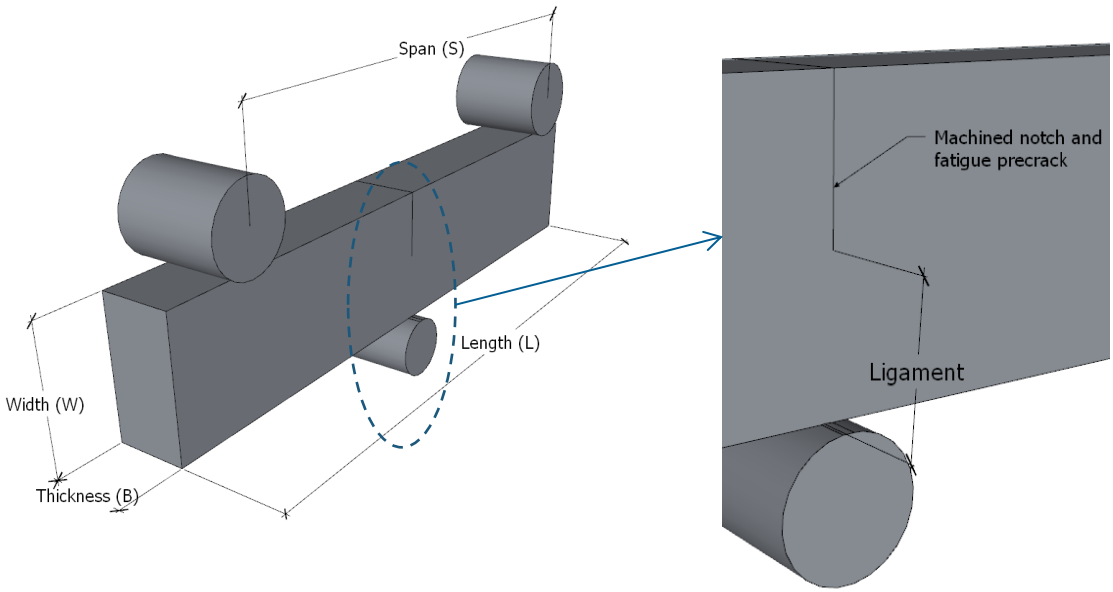

Figure 3-4 SENB specimen schematic; Ligament is equal to the height (W) minus the length of the machined notch and fatigue pre-crack (a).

The investigation into the effect of cross-sectional size of a SENB specimen is the most important part of answering the main research question. Whether or not a damage model calibrated from one specimen can be used to correctly simulate a different sized specimen, can be considered in multiple ways. This thesis limits the investigation of the size effect to the influence of the height of the specimen, more specifically the ligament, and the influence of the thickness on the damage model.

The reasons for a size effect in ductile metals such as the steel used in this thesis can be found in (Anderson, 2005). The major contributing factors to the size effect are:

i. The constraint at the crack tip, influencing the first principal stress to yield to be very high.
ii. The development of shear lips and their size relative to the cross-section.
iii. The size of the plastic zone can be too large compared to the ligament, causing full plastic bending as mentioned in chapter 3.1.1.

3.2.1 Ligament size

The influence of the ligament of the specimen on the fracture toughness is a topic that that has been thoroughly investigated, and fracture toughness experiments, such as British Standards 7448, contain various requirements on the ligament size. An important requirement in literature is that the plastic zone that is ahead of the crack-tip must be contained within the ligament in order to provide valuable fracture toughness parameters (Shih & German, 1981). Furthermore, Shih and German found that single parameter (J, K, CTOD) fracture toughness characterisation is only valid if the plastic zone is small compared to the ligament size. This is the case for small scale yielding, as was mentioned in section 3.1. An illustration of the development of the plastic zone in the specimen can be seen in Figure 3-5.
In Figure 3-5, the specimen has been loaded to a point before a crack has extended but has significant plastic

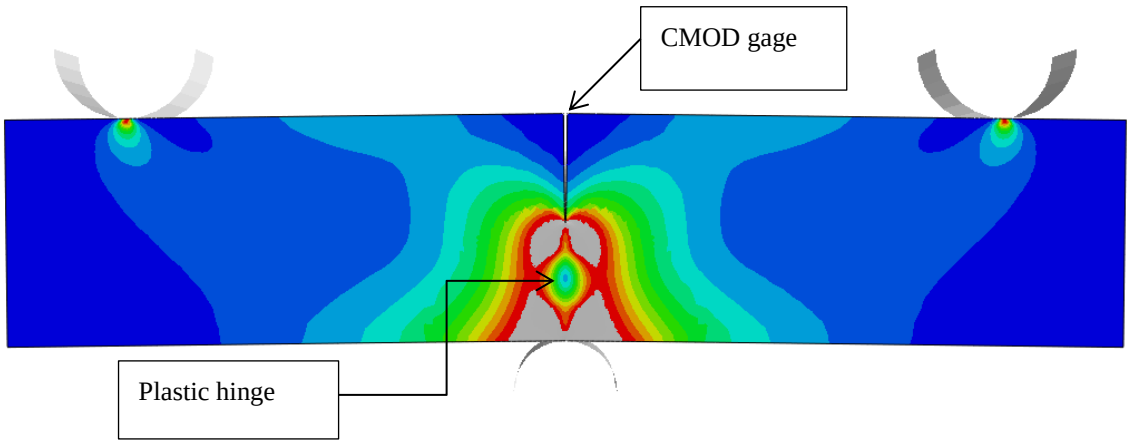

Figure 3-5 Development of the plastic zone (grey) in the SENB specimen Blue indicates stress close to 0, red indicates stresses close to 821MPa.

deformation. The plastic zone originating from the crack and from the backside have almost met each other, which is a clear indication that SSY assumptions are no longer valid. (Dodds, Anderson, & Kirk, 1991) generalised a requirement from the works of (McMeeking & Parks, 1979), (Shih & German, 1981) for the ligament length in order for the single parameter HRR field to be valid. The limit from this requirement is found at deformations well into the large scale yielding range, as indicated by a plastic hinge. Figure 3-5 shows the existence of a plastic hinge, which manifests itself as an oval-shaped, low-stress area in the plastic zone.
The plastic zone ahead of the crack tip as plotted in Figure 3-5 is, as long as the ligament size is large enough, not influenced by the plastic zone developing at the back of the specimen where the roller is located. For this reason, there are certain requirements in fracture toughness experiments to the size of the ligament. The requirement set by BS7448-1 for calculation of K_{IC}, shown in Equation 3.1, was converted to CTOD by a standard formula given by (Barsom & Rolfe, 1987).

$$\delta_C \leq 0.235 \frac{\sigma_Y}{E}\{a, B, W-a\} \qquad \text{(LEFM)} \qquad (3.1)$$

The specimens used in this thesis, their dimensions, measured critical CTOD and maximum CTOD as set by BS7448-1 to ensure that LEFM theory (e.g. K_{IC}) is representative are presented in Table 3-1. All specimens fail this requirement due to their large plastic zones at the time where the critical CTOD is found. From this, it can be concluded that these specimens are not suited to determine a maximum K_{IC}. In the case of CTOD testing and J-integral testing, the requirement for the size of the plastic zone is less strict. In ASTM E1820, a size requirement is given to ensure that the results are insensitive to the in-plane dimensions of the specimen. Again, all specimens fail this requirement.

Table 3-1 Validation of specimen's dimensions using BS7448-1 for LEFM and ASTM E1820

Specimen	a [mm]	B [mm]	W[mm]	Measured (δ_c) [mm]	Max δ_c LEFM [mm]	Max δ_c ASTM E1820 0.00333min{a,W-a}
24x48mm	23.9-24.0	24.0	48.1	0.53-0.58	0.0185	0.08 mm
24x24mm	11.9	24.0	24.0	0.41-0.43	0.0093	0.04 mm
12x24mm	12.0-12.1	12.5	25.0	0.36-0.41	0.0093	0.04 mm

The requirement that all specimens do meet is the requirement for ductile tearing as specified by ASTM E1820. This requirement and its results are presented in Table 3-2.

Table 3-2 Validation of specimen's dimensions using ASTM E1820 for ductile tearing

Specimen	Measured (δ_c) [mm]	Max δ_c ASTM E1820 ductile tearing 0.06*min{B,W-a} [mm]
24x48mm	0.53-0.58	0.72
24x24mm	0.41-0.43	1.43
12x24mm	0.36-0.41	1.43

To get back to the effect of ligament size, a step is made to a parameter that can help identify the difference in stress state by ligament size. In (Yuan & Brocks, 1998), an interesting observation is made concerning the Q parameter, stress triaxiality and the plastic limit load. The stress triaxiality is only slightly affected by the load intensity and crack length, until the plastic zone spreads over the un-cracked ligament. Until this point is reached, the Q parameter is close to zero for plane strain cases. This changes quickly as soon as the plastic hinge has fully developed, at which point the Q parameter becomes negative. The ligament has a direct effect on the moment at which the plastic hinge forms, and therefore on the Q parameter. It has been observed that for shallow cracked specimens (a/W=0.1), an immediate loss of constraint is observed upon loading (Nevalainen & Dodds, 1995). For the deep notched SENB specimens (a/W=0.5), Q values are positive at low loads, which agrees well with the known positive T-stress for this geometry in the greatest part of the specimen. Only near the free surface, negative values for Q are found. Q only becomes negative when larger deformations are found, corresponding to the loss of constraint due to the fully formed plastic hinge at that moment. In conclusion, it can be stated that contrary to a shallow notch, a specimen with a deep notch has:

i. A higher level of constraint
ii. A positive T-stress and Q parameter for small deformations and therefore a higher stress triaxiality.
iii. The highest constraint in the mid plane of the specimen (B/2)

In the paper by (Nevalainen & Dodds, 1995), the constraint effect, measured by Q, was found for a deep notched beam and a shallow notch in SENB specimen.

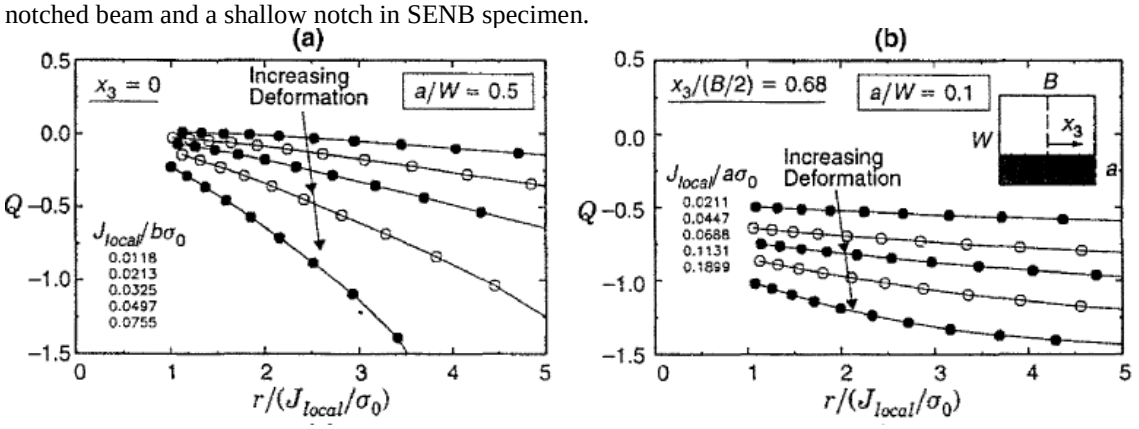

Figure 3-6 The effect of ligament size on the maximum Q as function of the normalized distance ahead of the crack front for various deformed states. (a) is for the deep notch, (b) is for the shallow notch. (Nevalainen & Dodds, 1995)

3.2.2 Thickness

Recalling the growth of ductile cracks from the previous paragraph, the formation of voids at a small distance from the crack tip dictate the direction of the growth of the crack. In a somewhat simplified way, this principle can be used to explain the existence of shear lips in some SENB experiment. In Figure 3-7, one half of a fully fractured SENB specimen is shown. In the centre, the crack is roughly in the same plane as the machined notch, but at the edges, lips develop with an approximate angle of 45 degrees to the tunnelling region.

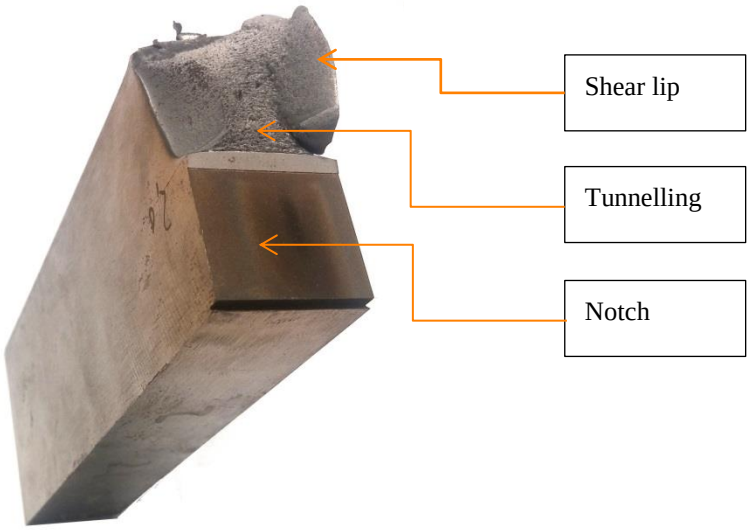

Figure 3-7 Half of a SENB specimen showing a shear lip and tunnelling

In the centre where the crack is tunnelling, the dominant crack mode is mode I, corresponding to a plane strain situation. Moving along the crack tip, starting from the centre towards the free surface, the shear cracking mode becomes more predominant as the stress state transforms from plane strain to plane stress. It is important to note that the theoretical concepts such as plane stress and plane strain and the cracking modes in practice always show up in a combination. References made in this thesis to cracking modes, plane strain and plane stress always indicate that that particular concept is the most dominant, but not necessarily exclusive. The fracture toughness parameters such as the stress intensity K, the J-integral and CTOD are dependent on the most dominant stress state. In chapter 3.1, it was shown that for simplified stress concepts as plane stress and plane strain closed form solutions were derived. The relative amount of material being subjected to any crack mode or a combination thereof decides the fracture toughness of the entire specimen. The amount of material being predominantly subjected to plane strain increases as the thickness of the SENB specimen increases. Likewise, the amount of material subjected predominantly to plane stress increases as thickness of the specimen is made bigger, but not in the same proportion as the material subjected to plane strain loading.

The effect of the thickness on the fracture toughness parameter J is shown in Figure 3-8. The J-Q trajectories of specimen with different W/B ratios are shown. From these finding two observations can be made. Firstly, while all specimens start at a constraint of greater than or equal to zero, thicker specimens lose their constraint much less quickly than specimens with a high W/B ratio. Secondly, a specimen with side-grooves was included in this test (denoted by SG), prohibiting the growth of shear lips. Compared to the other specimen with W/B of 2, the specimen with side grooves experiences less loss of constraint.

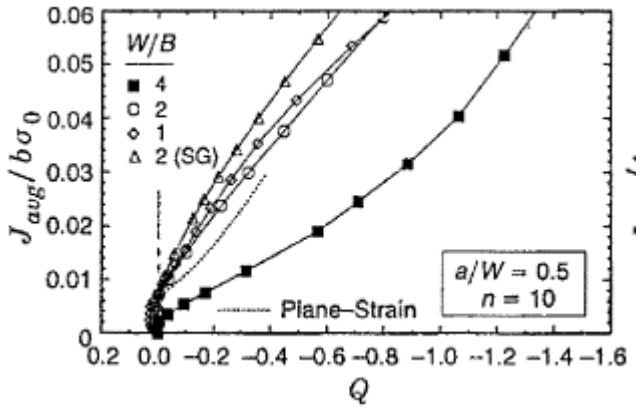

Figure 3-8 J–Q trajectories under increased loading, for various thicknesses in a deep notched specimen (Nevalainen & Dodds, 1995).

In mode I crack loading, the maximum plastic strain occurs at 45-degree angle to the crack plane. Thus, the preferred direction of the path of void coalescence, and as such the crack path, occurs at a 45-degree angle. The high constraint in the centre of the specimen causes the crack to grow in the direction of the ligament on a macroscopic level, while on a microscopic level a zig-zag pattern can be discerned. Naturally, the level of constraint (and stress triaxiality) near the free surface is much lower, and not great enough to force the crack to grow in the ligament direction.

In conclusion, it can be stated that there are two factors that give thickness dependence for SENB specimen. On the one hand, the shear lips, and on the other hand the constraint. While the influence of the shear lips and the influence of the constraint are certainly connected, the origin of shear lips lies more within the difference between plane stress and plane strain. The size of the shear lips however, seems to be related to the constraint. The SENB specimen examined in this thesis with identical ligament size (24x48mm prop and 24x24mm), have approximately the same size shear lips.

4 PLASTICITY MODEL CALIBRATION

In this chapter, the elastic and plastic material parameters that are used throughout this thesis are derived. These parameters are determined using a tension bar test specimen and multiple finite element models with an approach of iterative calibration, known as the “inverse method”.

4.1 Experiment

A tensile test has been carried out with a round bar specimen according to the ISO 6892-1 standard. The elongation of the specimen is recorded by an extensometer, and the experiment is displacement driven. The white dots in Figure 4-1 are the places where the extensometer is fixed and are small indentations 50 mm apart. In other words, the displacement between these two points is provided by the measuring equipment. To improve accuracy, another set of indentations with an approximate offset of 5 mm with respect to the original set is created. At the end of the experiment, the final displacement is reported as the average of displacements between these two sets. During this procedure, the specimen is loaded until fracture, and the extensometer is present during the entire experiment. Finally, the force versus elongation data can be extracted from the measuring devices and provides the curve displayed in Figure 4-2.

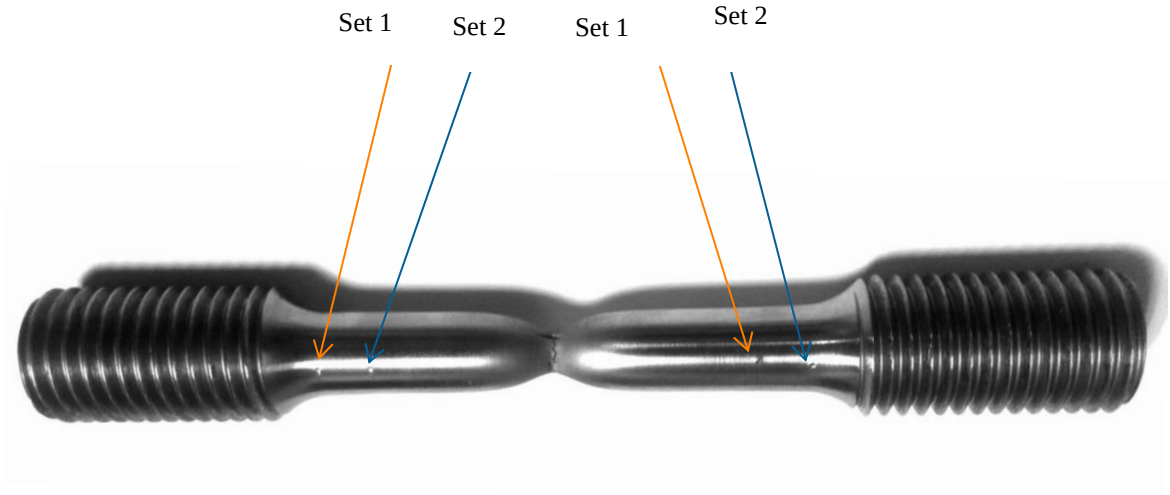

Figure 4-1 Experiment schematics and test specimen SW3A-2

4.1.1 Results

In the obtained results, various stages of material behaviour characteristic to steel are present, starting with the linear elastic behaviour displayed in orange in Figure 4-2. As the elongation increases, an almost horizontal plateau arises in the force and displacement curve. This is called the Lüders band and is caused by localised bands of plastic deformation. Then an increase in force characterises the onset of a process called strain hardening, which is the second stage of plastic or non-linear behaviour. In this process, the material is strained past its yield point, resulting in the movement of dislocations (irregularities in the crystal structure). At first, this provides little resistance, but as the density of dislocations increases, so does the stiffness. During this process of hardening, the elongation of the specimen results in a reduced cross-section determined by the conservation of volume. Ultimately, the cross-section starts to reduce by a greater proportion

than the hardening can compensate for, and at that point, the ultimate tensile strength of the material is found. In Figure 4-2 this is the point where the red line changes colour to the blue and according to the Considére condition this is where the maximum force is found. Additionally, the sudden change in gradient of the purple line showing the cross-sectional area of the specimen supports the statement that the maximum force is the onset of necking. This deformed area is obtained from a FEM simulation with the finest mesh size and is discussed in 4.2.2. The stage described by the blue line is referred to as necking of the material, where the term necking is used because of the local decrease in cross-section similar to a neck. This process continues until a strain is reached for which the material fractures. In Figure 4-2, this is shown in green and is displayed as a sudden drop in force.

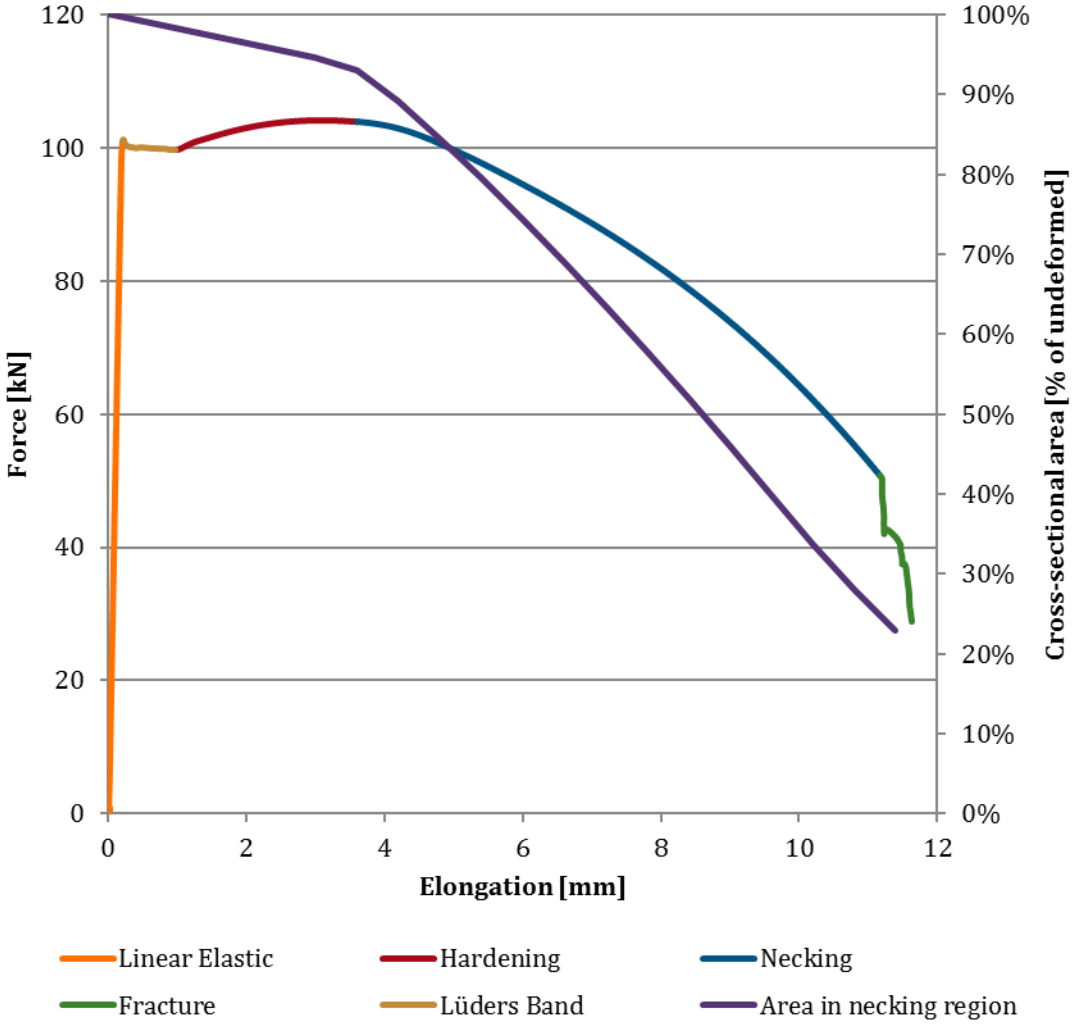

Figure 4-2 Force-elongation curve of tensile experiment and area in necking cross-section from FEM simulation.

4.2 Model

In this paragraph, the model that is used in the finite element simulation of the experiment is described. The software package Abaqus 6.14.1 is used in this analysis.

4.2.1 Geometry

In deciding on the most suitable geometry for this model, a few basic principles were used and verified. An accurate model for the calibration of the tensile data can be generated by copying the complete geometry of the tensile test specimen and transforming it into a finite element model by meshing this geometry. This results in the finite element model shown in Figure 4-3. The top of the specimen is pulled upwards while the bottom is clamped. The geometry has multiple planes of symmetry, notably rotational symmetry around

the vertical axis (yellow dotted line), and the top and bottom are symmetric about the plane displayed with the orange dotted line. The rotational symmetry implies also quarter and half symmetry about the vertical planes. Applying symmetry has the major advantage that the number of elements is decreased and thereby the computation time. Additionally, using the properties that the displacement was actually measured in between the indentations in the specimen, as described in Chapter 4.1 and Figure 4-1, the geometry can be simplified to a less complex geometry. This new geometry is presented in Figure 4-4, and the use of this geometry versus the complete geometry is justified in paragraph 4.2.2.

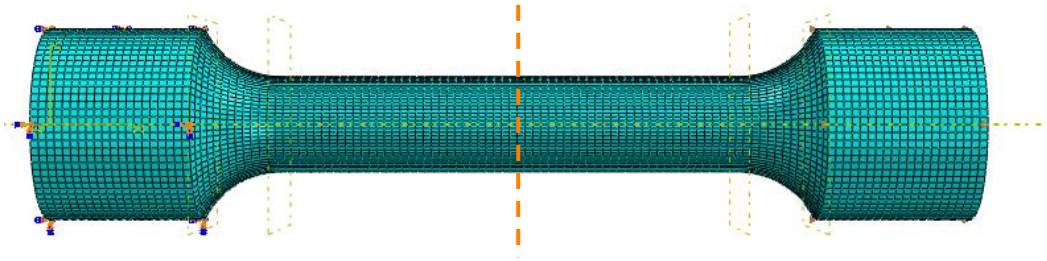

Figure 4-3 Model geometry

The following key assumptions have been made:

1. The location of the concentrated displacement resulting in necking along the length axis does not influence the results of the experiment.
2. The elongation is concentrated in the absolute centre along the axial direction of the specimen.
3. The neck occurred at a great enough distance from the contacts of the extensometer that no portion of the neck fell outside the measurement points of the extensometer. Any significant elongation occurred between the measurement points and is therefore captured by the extensometer and assumed geometry.
4. The elongation of the top half is equal to the elongation of the bottom half and is therefore equal to half the total deformation.

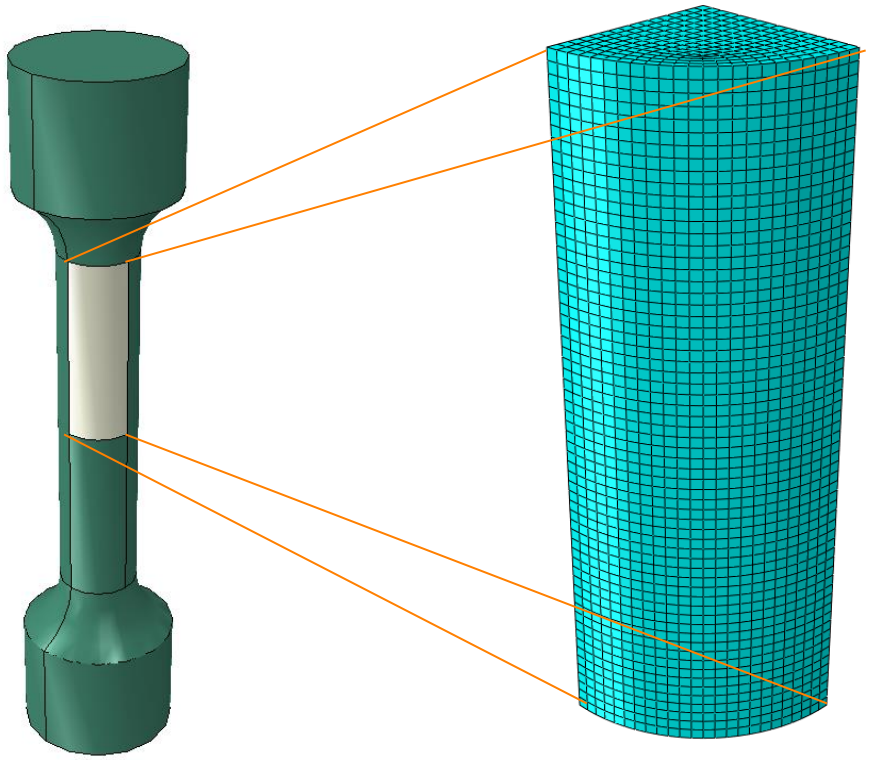

Figure 4-4 Full geometry (left) and assumed geometry (right)

4.2.2 Mesh and refinement

In the development of the model, a mesh convergence study is required to determine the minimum number of elements to obtain a converged solution. Additionally, the claims made in the previous paragraph that

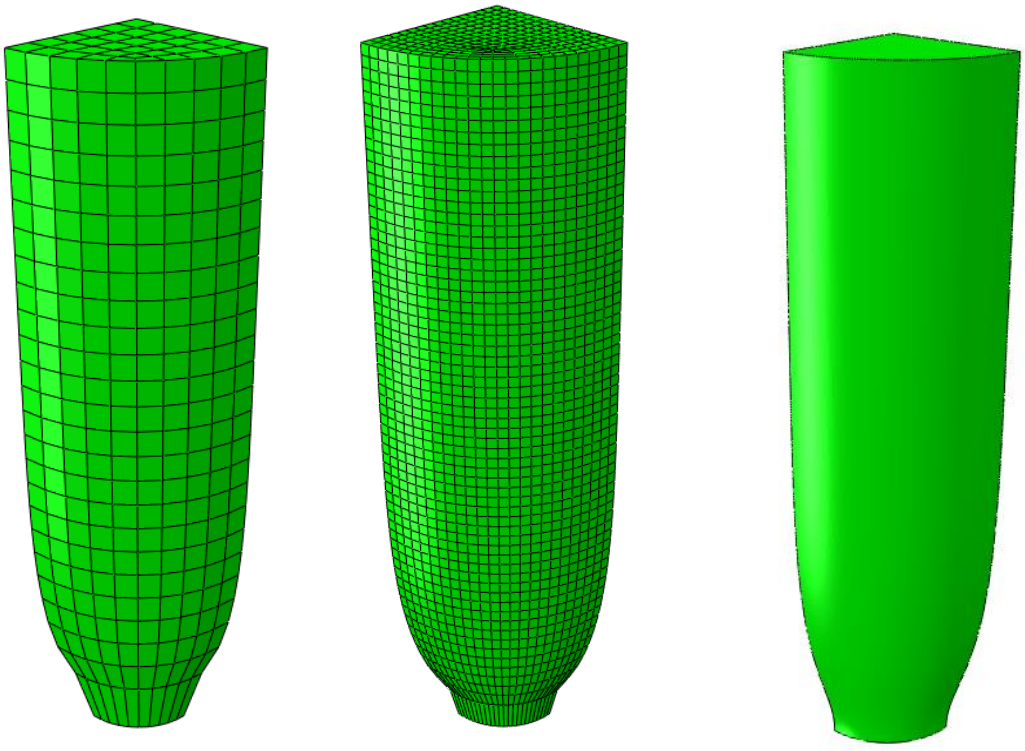

Figure 4-5 Deformed coarse mesh (left) and medium mesh (middle) and ultrafine (right). All meshes and details are listed in Appendix A.

form the basis on which the simplified geometry is made are tested. This is done by comparing the results for the full geometry with the results of the partial geometry presented below. A full overview of the meshes that were used, their element size, dimensions and properties are presented in Appendix A. Three of these meshes are presented below to illustrate the difference in deformation shape between different sized elements.

In the fine meshes, the necking predominantly features a steep decrease of cross-sectional area, whereas the coarse mesh shows a more gradual decrease in area. In the ultrafine mesh, the elements are hidden as Abaqus is not able to properly display them on the account of the large amount. Apart from making a visual difference, the coarse mesh shows less stiff behaviour overall and requires higher stress values in the plasticity model to fit with the experimental data. The plasticity model is calibrated on models with different mesh sizes in order to investigate the mesh size dependency of the problem. The results of this mesh refinement analysis are presented in Appendix A. Since the stress states in the SENB model range from plane strain to plane stress, using a plasticity model calibrated to a uniaxial tensile test is not entirely correct for every element. The assumption is made in this thesis that the plasticity model derived here is adequate to simulate the plastic behaviour of the SENB specimen until crack growth. While it is hard to say whether the assumption is valid, there is some evidence from experimental results that the point of deviation between the SENB experiment and its FEM simulation is within a range where one would expect crack growth. The plastic behaviour of the SENB specimen until the first deviation is shown in paragraph 4.5. The range of displacement in which crack growth is expected to happen is further discussed in paragraph 5.1.2.

To address the assumptions made in the previous paragraph, the necessary verifications have been made. Starting with the third claim from the previous paragraph, which states that any significant elongation of the specimen occurs in between the measuring points, this claim can be tested by looking at the deformations in the full model as shown below.

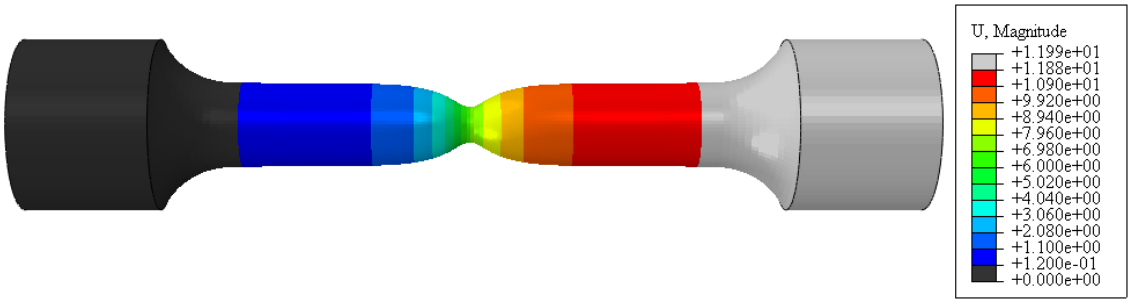

Figure 4-6 Deformation of the full model

The dark grey shaded part of the full model shows a deformation of zero with an accuracy of $1*10^{-3}$ mm, which is considered negligible compared to the total deformation of 12 mm at the point of failure. The measuring points are located well within the grey sections, suggesting that the assumption that any significant deformation occurs within reach of the extensometer. Based on this information, the assumption that the thick part of the model can be replaced by a boundary condition at the top of the simplified mode presented in Figure 4-5 is justified. Furthermore, the deformed model shows that the use of the quarter symmetry is justified since the deformation is constant over the cross-section at any given point along the horizontal axis in Figure 4-5. The fourth claim, stating that the deformation of half the model (i.e. the left part of Figure 4-5) is half the deformation of the total model, is justified by these results. The elongation in the neck is 6 mm, whereas the total deformation is 12 mm using the same accuracy as before.

Finally, all claims are tested by comparing the results of the full model with the calibrated plasticity model to the experimental results and to the results of the simplified model. The findings of this comparison can be seen in Figure 4-7.

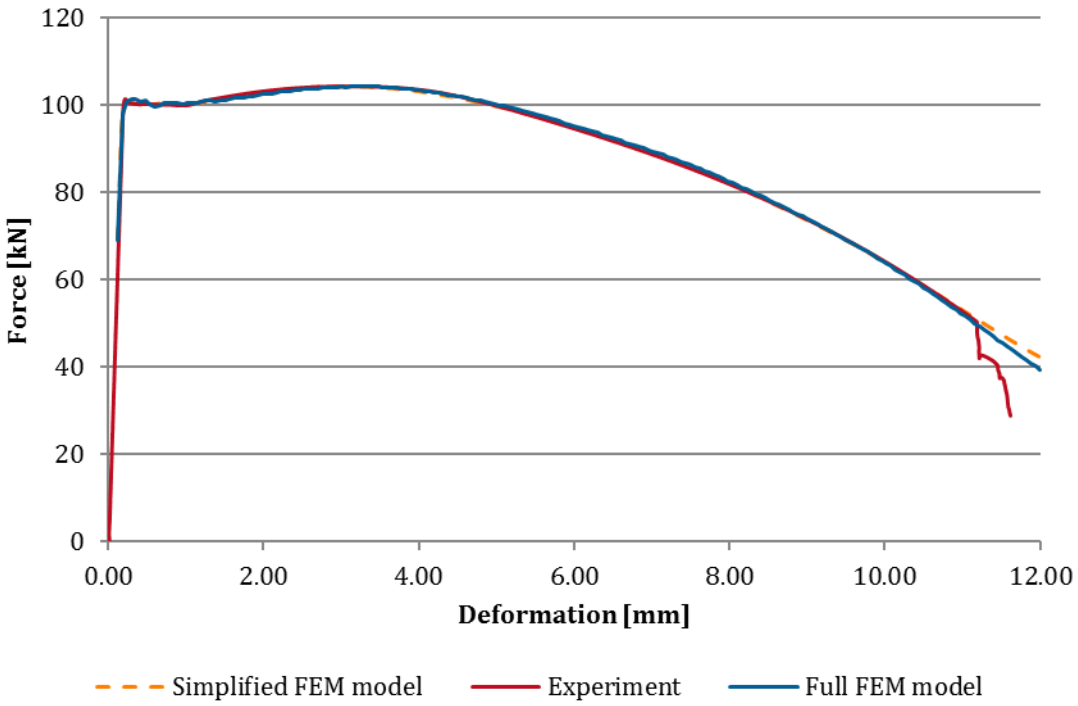

Figure 4-7 Simplified model versus full model and experiment

These results are considered as proof that the assumptions are justified for use in these calibration procedures. The largest deviation from the experimental values is where the fracture of the specimen occurred, which is at a deformation of approximately 11 mm. The deformed states at that point are presented in Figure 4-5. Figure 4-8 shows the deformed mesh of the ultrafine mesh overlaid on a picture of the tensile specimen to give an impression of the similarity between the deformed mesh and the experiment. While this provides little proof in itself that the calibrated plasticity model is correct, the overall shape does match. Additionally, the test report by (Element materials technology, 2016) provides the area reduction at failure as 75%. This is the same as is found in the finite element simulation for the (ultra)fine mesh at the point of fracture (see Figure 4-2). The error in terms of area reduction are less than 1% for the coarse mesh and the fine mesh.

Figure 4-8 Deformed mesh overlaid on specimen.

4.3 Calibration of the plasticity model

As stated before, the plasticity model is derived using an iterative procedure starting from the derived stress-strain relationship of the tensile experiment. Firstly, this is done to have a plasticity model that also simulates the experiment correctly during necking, since the conversion formula of engineering and true stresses does not take necking into account. Secondly, this is done to obtain a more accurate model than is obtained when simply converting the experimental (engineering) stresses and strains to true stresses and strains.

4.3.1 Procedure

The procedure starts with calculating the true stress-strain relationship from the force, displacement and cross-section before and after failure. This starting procedure is described by the steps indicated in Figure 4-9.

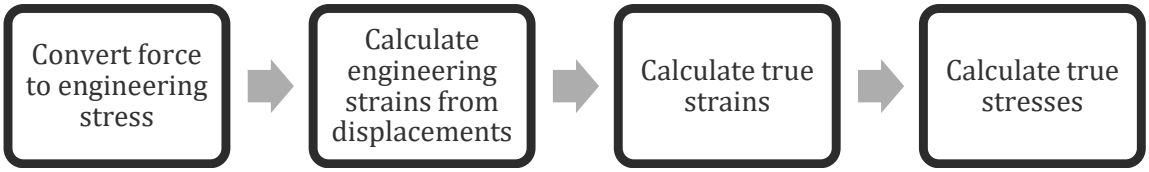

Figure 4-9 Processing experimental data to true stress-strain relationship

The engineering stress is calculated using the original cross-section, whereas the true stress is calculated using a basic formula that accounts for the reduction in cross-section due to conservation of volume. The formulas used are presented in appendix A. After this initial procedure, a starting point for the stress strain curve is obtained, which is then inserted into the material data of a finite element model using any of the meshes presented earlier. This data tends to give a small underestimation of the stress-strain relationship that is required to obtain a fit with the experimental data. Through an iterative procedure described in Figure 4-10, the stress-strain input data is tuned to fit the experimental results.

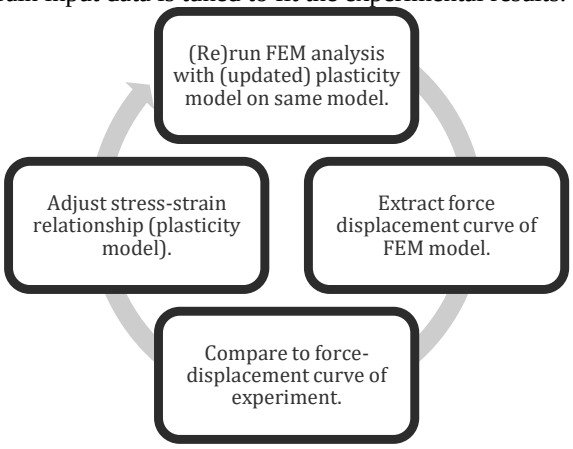

Figure 4-10 Steps of the iterative plasticity model calibration

The starting point of the iterative procedure is running the FEM analysis with the true stress-strain relationship. Then the force and displacement of the finite element procedure is extracted and compared to the data from the experiment. As long as there is a difference of more than one percent, the stress-strain relationship is adjusted, the analysis is rerun and the results compared again.

4.3.2 Analysis

After some iterations, varying per mesh size, a relationship between stresses and strains is found that provides a result that is comparable to the experiment when input into the model. The results from the calibration procedure is shown in the Figure 4-11, which was for the case of the fine mesh consisting of elements of 0.2 mm.

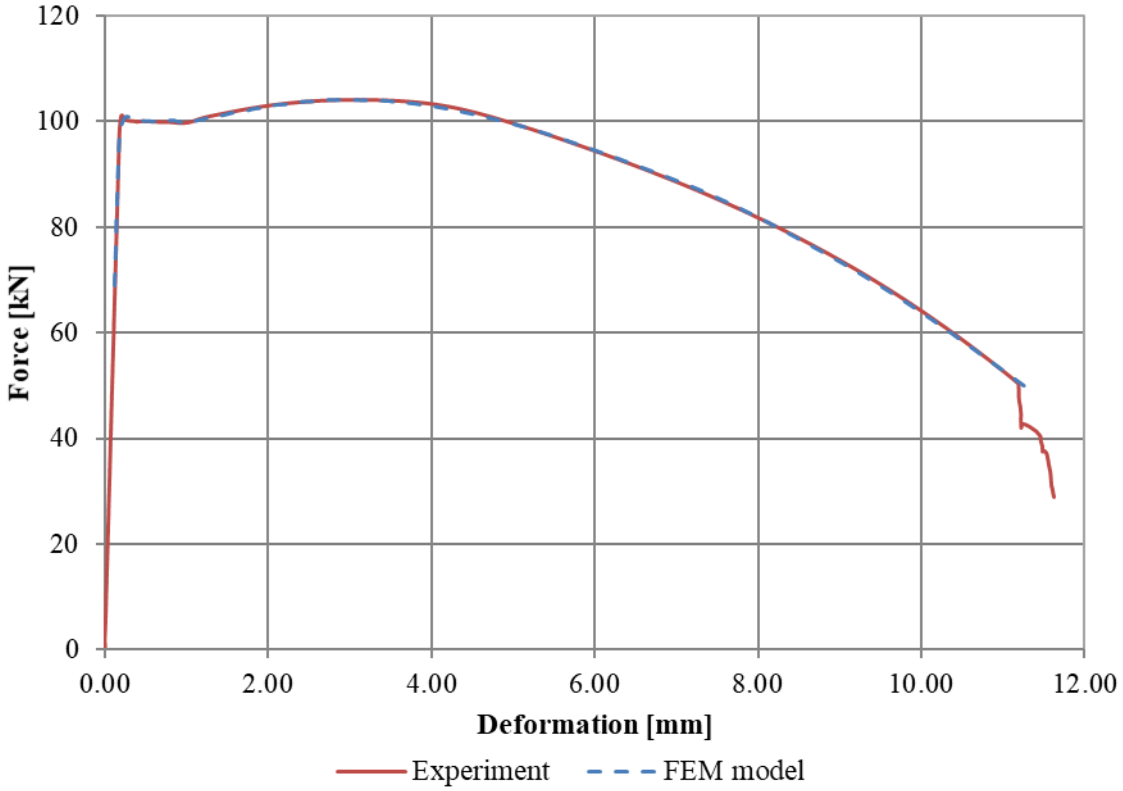

Figure 4-11 Results of calibrated plasticity model versus experiment data

The line describing the experimental data and the line describing the simulation data almost fully overlap, except for the part where the specimen breaks. The stress strain data corresponding to this result is thus considered valid for this material and is used in the model of the SENB experiments later in this thesis. While it has been established that the full model and simplified model provide results that agree to the extent where fracture occurs, the model might still be influenced by a geometry size effect. Further investigation of this possible issue is done by introducing a proportional model that undergoes proportional displacement but has the same plasticity model. This proportional model is again a part of a tensile test specimen, but with half the dimensions of the models used in this chapter.
The dimensions and mesh information are presented in Table 4-1.

Table 4-1 Dimensions and mesh information proportional model

Name	Height [mm]	Radius [mm]	Elements	Element size [mm]
25x01mm	25	6.25	1876982	0.1
25x02mm	25	6.25	118000	0.2
12.5x01mm	12.5	3.125	118000	0.1

The proportional model is geometrically an exact scaled version of the other models, so one would expect the results to be an exact scaled version of the results in the normal sized simulations. The geometry is scaled by a factor 2 and consequently the cross-sectional area by a factor 4. This is tested by comparing the force-displacement values of both experiments, while scaling the forces of the proportional model by a factor 4. The 25x02mm mesh has the same element size relative to the geometry as the proportional mesh. The relative difference between the recorded forces is presented in Figure 4-12.

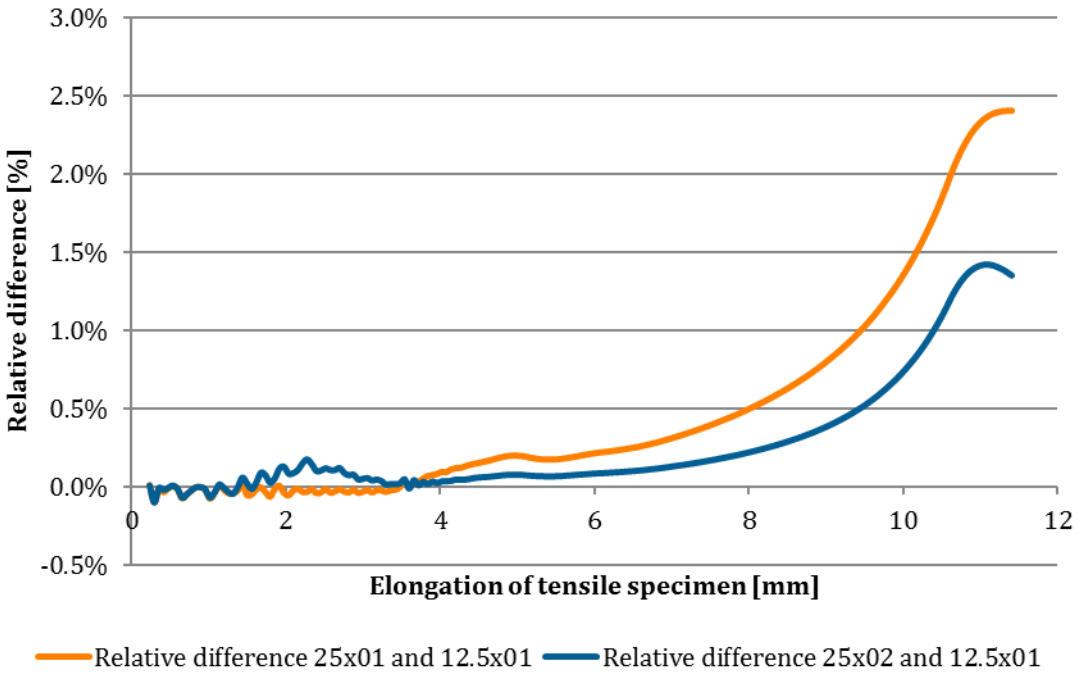

Figure 4-12 The effect of specimen size in numerical experiments

The difference between the two models seems to be related to the onset of necking. After the necking occurs at an elongation of about 3.8mm, the relative difference between the two increases fast, while the difference before that is negligible. The relative difference is calculated with respect to the 25x01mm mesh results and therefore a positive difference shows that the response of the proportional model is stiffer, while a negative difference shows that the response of the proportional model is less stiff. In conclusion, it can be stated that during necking, the smaller geometry results in 2.4% stiffer behaviour than the larger geometry with the same element size and up to 1.4% stiffer compared to a larger geometry with the same relative element size. In literature, it is shown that the plastic strain inside the neck depends on the aspect ratio of the minimum diameter of the neck to the radius of curvature of the neck (Bridgman, 1952). From this one can state that if proportional dimensions are chosen the difference in strains and stresses between scaled versions of the same specimen is small. This however also means that when the simulations have different aspect ratios the necking will be different.

4.4 Results

The results of the plasticity model calibration procedure are described by Figure 4-13. The stress-strain relationship as derived from the experiment and the calibration later are shown is this graph. There are a few key differences between the three different stress-strain relationships. The engineering stresses and strains are based on the initial cross-section of the material being constant and therefore have a lower maximum stress than the true stress curve. The true stresses are obtained while taking into account the reduction of the cross-section, which works until the point of necking. To obtain a stress-strain relationship after that, a power law was fitted to the true stress-strain values until necking and used to extrapolate stresses even after necking. Paragraph 4.3.1 explains the procedure of calibration of the plasticity model and this true stress strain curve complimented with the power law extrapolation after necking serves as starting point in the calibration procedure. During the calibration procedure, the true stresses had to be adjusted upwards one to three percent to provide the fit seen in Figure 4-11.

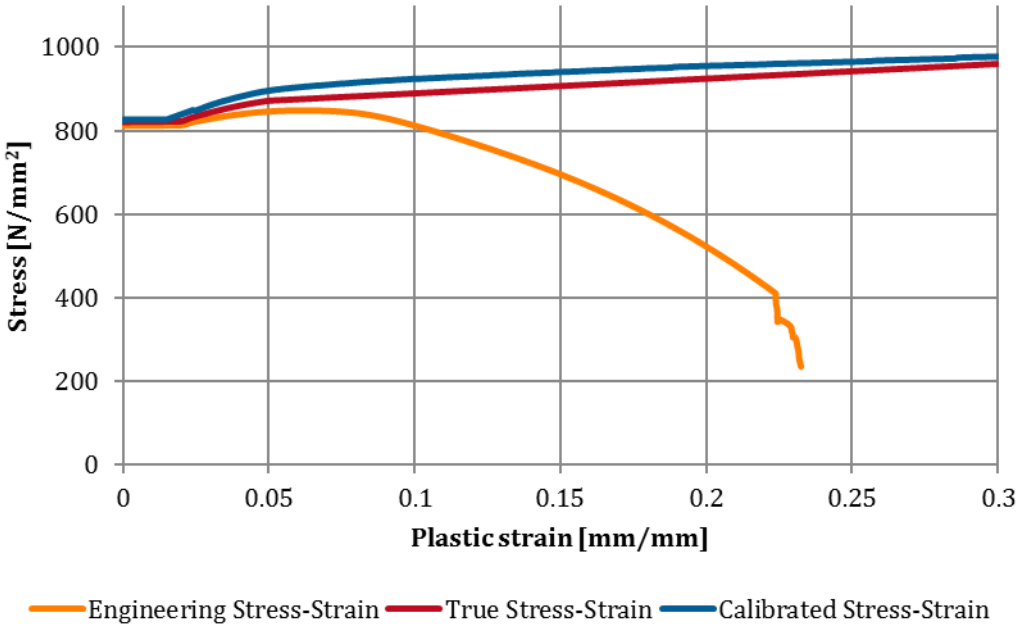

Figure 4-13 Engineering vs true vs calibrated stress-strain curve for the ultrafine mesh.

4.5 Verification of the plasticity model

The validity of the plasticity model derived in this chapter is first of all verified by comparing it with the experimental data as presented in Figure 4-11. Keeping in mind that this data is used later in the simulation of the fracture (SENB) specimen, the plastic behaviour of that experiment should be well simulated with this plasticity model. At some point in time, a crack starts developing in the fracture specimen, but for a large force domain, the results of the experiment and simulation before that first crack should overlap.
The results from a fracture experiment and a simulation using the derived plasticity model are presented in Figure 4-14. A simulation without the plasticity model would follow the green dotted line denoted by "Linear part", while the simulation with the plasticity model overlaps the experimental data to a significantly greater extent. Therefore, it is concluded that the plasticity model derived in this chapter adequately describes the plastic behaviour of this steel type. The line showing the linear part is an extrapolation of the result obtained at a crack mouth opening displacement of 0.3, which is just before where the plasticity model is first used.

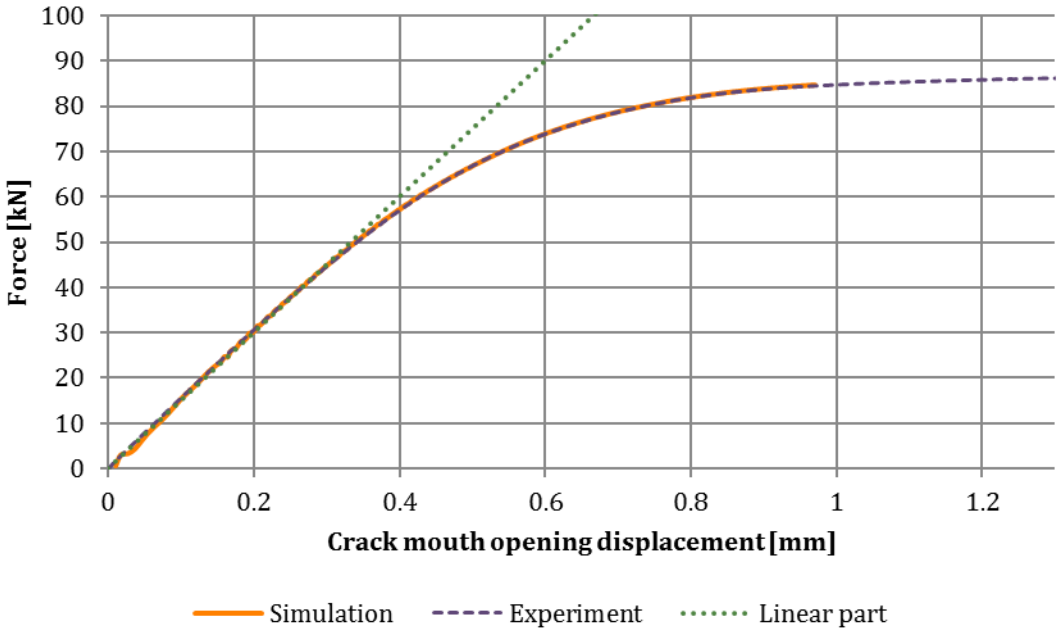

Figure 4-14 SENB experiment data versus simulation with plasticity model but no failure

5 DAMAGE MODEL CALIBRATION

In this chapter, the procedure for the calibration of the damage model is presented. First, the goal of the calibration of the damage model with respect to the thesis questions is briefly recalled. Secondly the experiments that were necessary to obtain the damage model are presented and their simulated counterparts follow in paragraph 5.2.
Then, the procedure of calibration is explained in theory in the paragraph called Calibration of the damage model. In the last paragraph of this chapter, the damage model that is obtained in this chapter is verified. The damage model used here is meant to allow a finite element simulation to agree with reality where the elasticity and plasticity model does not suffice anymore. In this thesis, the damage model describes the physical growth of cracks.

The main research question is as follows:

Is a stress triaxiality, Lode angle and plastic strain based failure model, calibrated from a single SENB specimen, able to correctly predict failure in differently sized SENB specimen?

This can be split in two parts:

1. Is it possible to calibrate a failure model, where the strain at failure is a function of stress triaxiality and Lode angle, using only a single SENB specimen?
2. Is this failure model able to correctly predict crack growth in SENB specimen with different geometries?

Correct crack growth prediction is defined in the following ways:

3. No or small differences between the force-CMOD measured in the experiment and the simulation.
4. Agreement between the crack path in the experiment and simulation.

This chapter deals with the first part of the research question: calibrating a failure model using a single SENB specimen.

5.1 Experiments

The experiments that are used in this chapter use single edge notch bending (SENB) specimens. These specimens are described by British Standards 7448 and are briefly introduced in this paragraph. The single edge notch bending specimen is a prismatic beam with a machined notch on one side, which has been extended by a fatigue crack due to cyclic loading. The specimen is placed in a displacement controlled three-point bending machine that measures the force, transverse displacement and crack mouth opening diameter (CMOD). Currently, these standardised experiments are used to obtain the fracture toughness of materials in various expressions such as the opening mode plane strain fracture toughness (K_{IC}), the critical crack tip opening displacement (CTOD) and the *J*-integral. The reason a SENB specimen is so useful to derive a damage model in the way that is described in this thesis is that a wide range of stress states occur along the crack front. The theory behind the different existing stress states and why they occur was outlined in Chapter 3.

5.1.1 Setup

The testing apparatus is displacement controlled and measures the displacement of the bottom roller going up and the opening of the crack mouth with a gage located between the two top rollers. The experiment is continued until either the crack mouth gage reaches its maximum value of about 7mm, at which point a significant crack has developed, or until the top rollers show significant movement (more than 0.5 cm) in the horizontal direction.

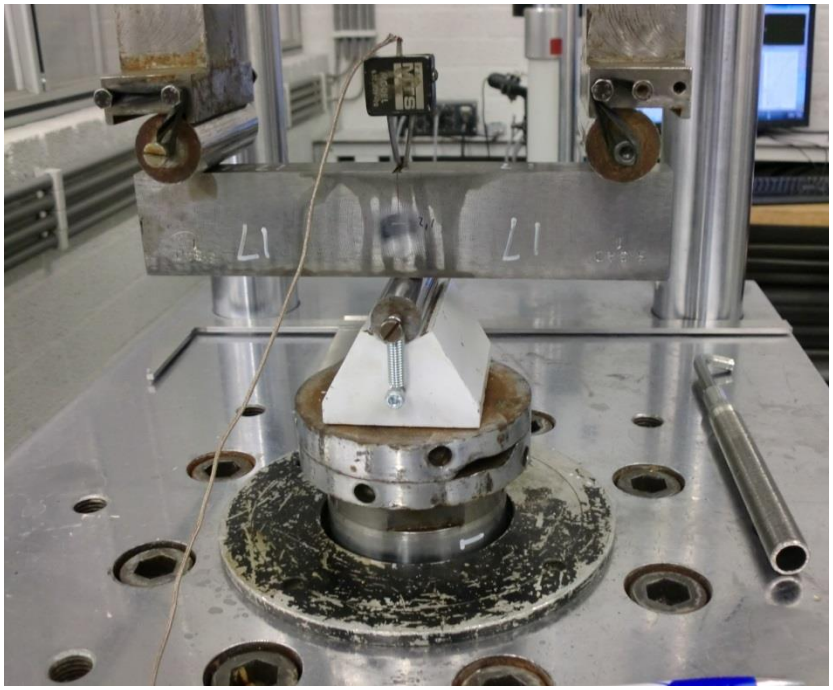

Figure 5-1 Picture of the SENB testing equipment.

After the crack mouth opening gage reaches its maximum value, a different device is used to fully fracture the specimen. No additional data is acquired in this final procedure. A close-up of the specimen at the end of the procedure with CMOD gage is shown in Figure 5-2.

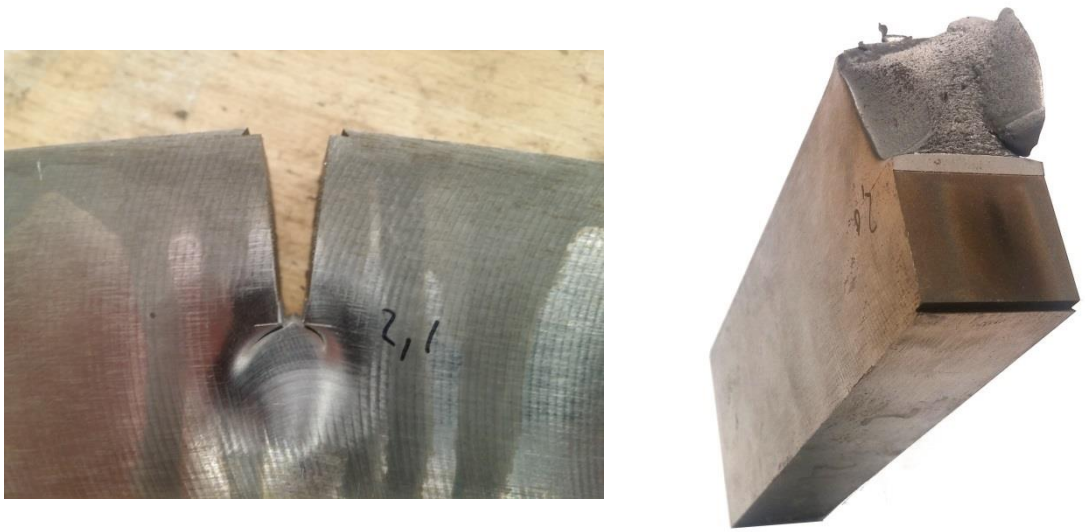

Figure 5-2 Close-up of crack mouth after the initial procedure (left) and half of the fully fractured specimen after the final procedure (right).

The specimen is schematically drawn in Figure 5-3.

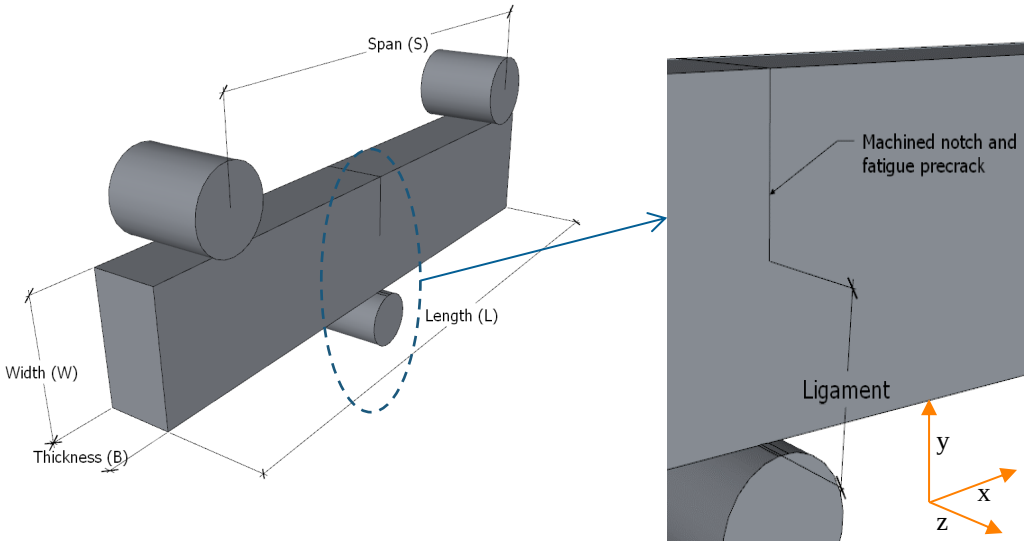

Figure 5-3 SENB specimen schematic

The three different specimen sizes that were used are listed in Table 5-1. For each size, three specimens were tested to show reproducibility. Testing errors include the occurrence of small cracks running perpendicular to the fatigue pre-crack, a phenomenon known as split. This small crack is caused by micromechanical irregularities and cause jumps in the force-CMOD curves presented in paragraph 5.1.2. The failure and plasticity models are not equipped to work with the failure mode connected to a split, and the specimens that showed splits are therefore left out of the damage calibration procedure.

Table 5-1 SENB specimen dimensions

Name	Length[mm]	Width [mm]	Thickness [mm]	Span [mm]
24x48mm	237.0±0.1	48.05±0.01	24.01±0.03	186.0±0.1
24x24mm	116.0±0.1	24.04±0.03	24.05±0.03	100.0±0.1
12x24mm	122.0±0.1	25.04±0.03	12.53±0.02	100.0±0.1

5.1.2 Results of the experiments

The results of the experiments are reported in this paragraph. The 24x48mm specimen are presented first, followed by 24x24mm and 12x24mm. The force versus crack mouth opening diameter (CMOD) diagrams are the most important results in this research, as they are used to determine a deviation between the experimental results and the finite element simulation. Furthermore, the force-CMOD relationship is relatable to work that has been done in this field before, and is directly relatable to fracture mechanics parameters as mentioned in paragraph 5.1. The results of all similarly sized experiments are presented in one graph.

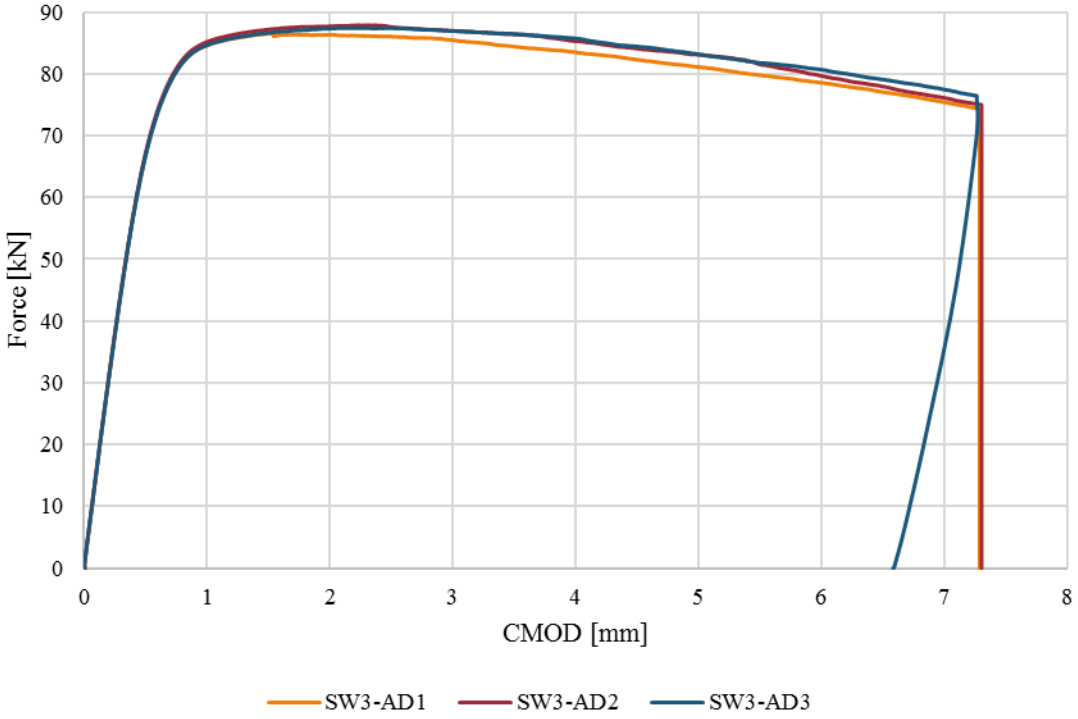

Figure 5-4 Force-CMOD curves for the 24x48mm experiments with 25x50mm cross-section

The results of the specimen SW3AD-3 are used in the calibration of the damage model, but specimen SW3AD-2 could also be used. Specimen SW3AD-1 shows the occurrence of split, causing a small drop in force around a CMOD of 1.5. The occurrence of a split does have one useful feature, namely that it provides an indication on both the force versus CMOD curve and the fracture surface as it happens and therefore might shine some light on when the crack is growing. The fracture surfaces of two specimens are shown in Figure 5-5. The EDM (Electrical Discharge Machining) notch and fatigue pre-crack are characteristic for the SENB experiment.

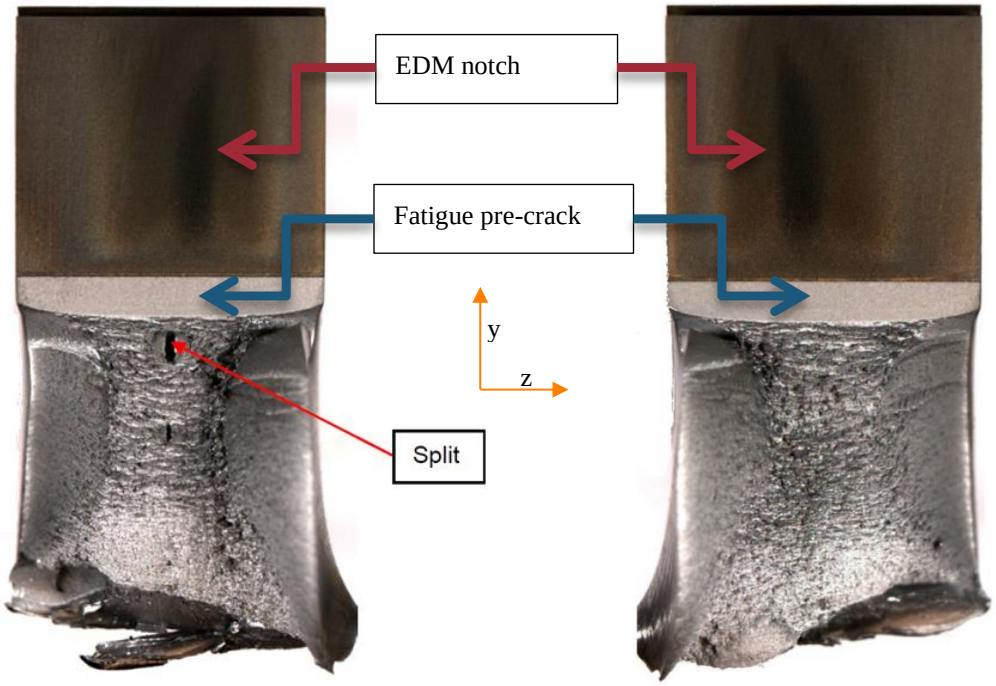

Figure 5-5 Fracture surfaces of specimen SW3AD-1 (left) and SW3AD-3 (right) with 24x48mm cross-section.

Whether the growth of the crack has advanced to the point where the split occurred at the point in time when the small force drop is recorded does not really matter. More important is the indication that at that point, the material has started failing and is therefore not accurately simulated by either the elastic or the plastic FEM model.
Similar results are obtained from the other geometries, displayed in Figure 5-6 and Figure 5-7.

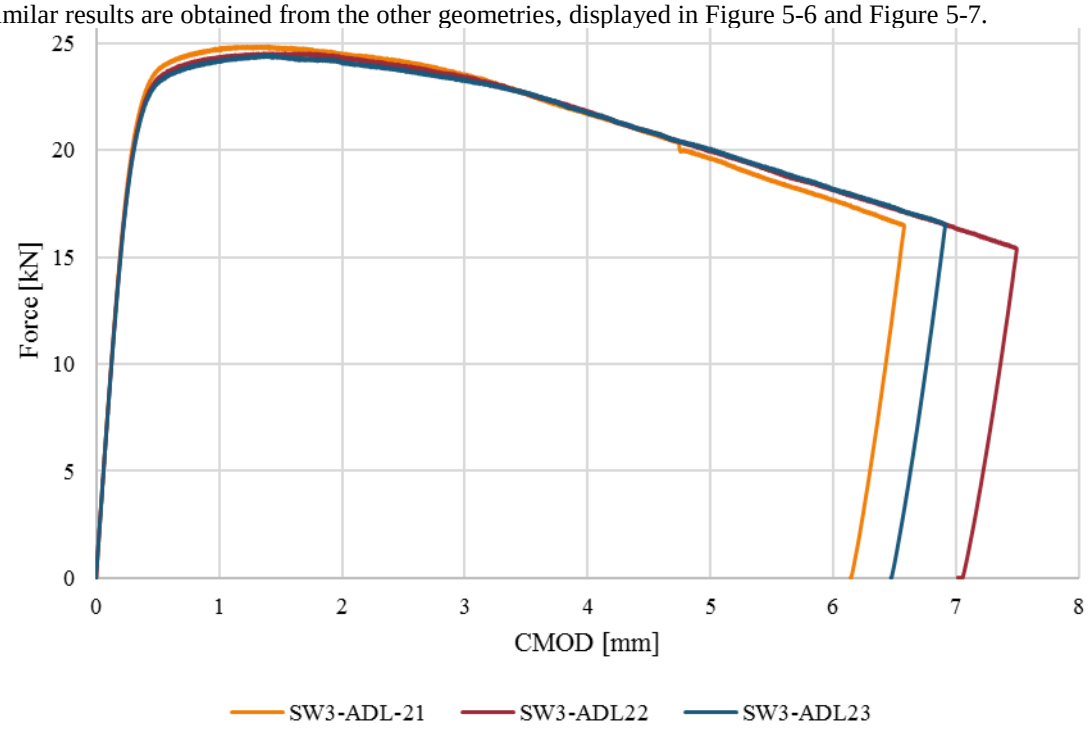

Figure 5-6 Force-CMOD curves for the 12x24mm. specimen with 12x24mm cross-section.

In specimen SW3-ADL21, the split occurred at a CMOD of approximately 4.7mm, after the maximum force plateau. For this reason, such a specimen does meet the requirement of the BS7448 standard, where the fracture toughness parameters are calculated based on the maximum force.

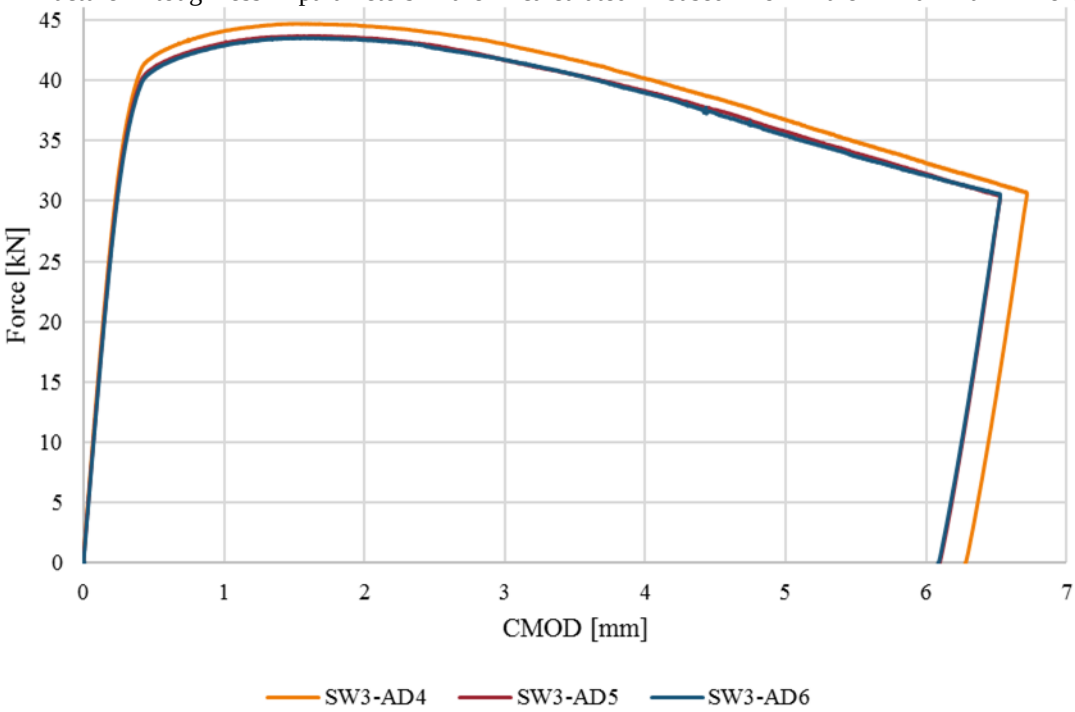

Figure 5-7 Force-CMOD curve of the 24x24mm specimen with 24x24mm cross-section.

5.2 Model

In this paragraph, the assembly of the model is presented. First some general considerations about the use of the finite element method for this particular case are discussed. Then the development of the geometry for the model is discussed, followed by the mesh and the type of analysis.

5.2.1 Geometry

The geometry as seen in Figure 5-3 is almost fully imported as a geometry for the finite element analysis, with one major difference. Only half the beam is considered since the crack growth is symmetric in the length axis of the beam as was hypothesized by (Dagadu, 2015).

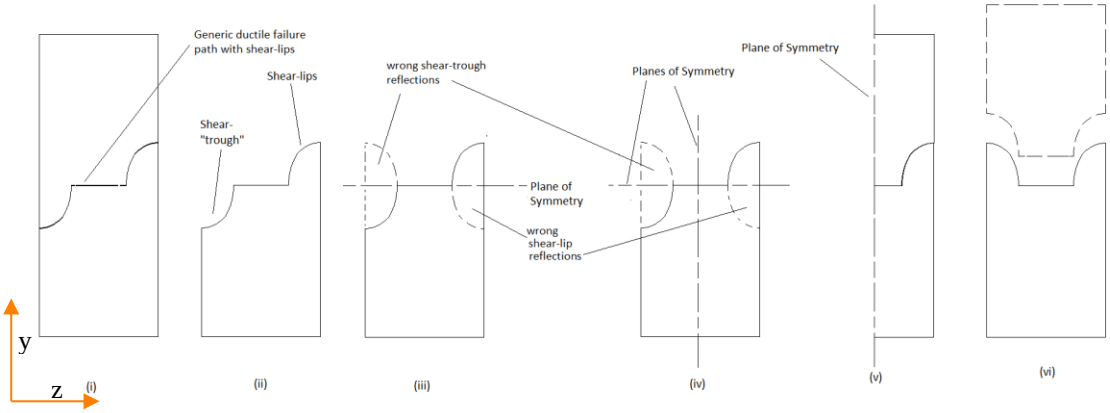

Figure 5-8 Symmetry in fracture surface and permissible planes of symmetry for FEM by (Dagadu, 2015).

Using this knowledge, the suggested plane of symmetry labelled v in Figure 5-8 is used to create the geometry for this model. This plane of symmetry does not only exist when looking at the fracture surface, but also in the stress and strain ranges.

5.2.2 Mesh and refinement

The mesh used in this simulation must be able to accurately describe the behaviour of the beam under the influence of contact with the rollers and physical crack growth by element erosion. Both areas require a certain degree of refinement of the mesh, while in other parts the strain gradients are both of little importance and negligible in magnitude. Detailed information about the meshes is presented in Appendix B. A typical mesh of the xy-plane is shown in Figure 5-9.

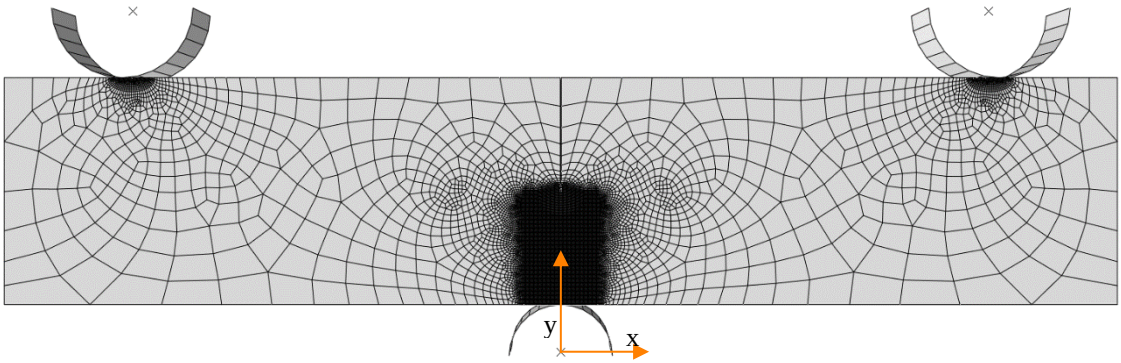

Figure 5-9 Mesh overview on the xy-plane.

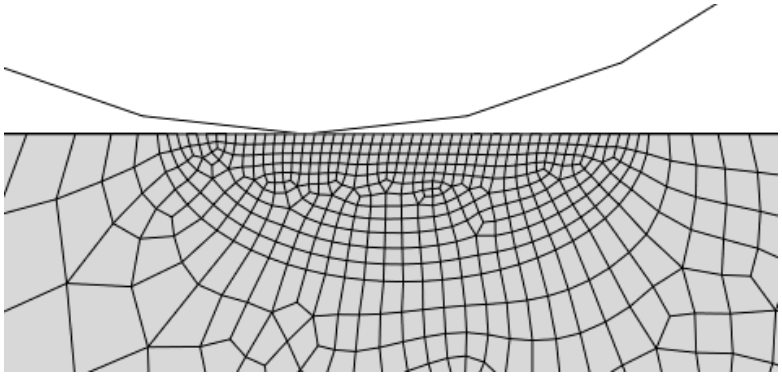

Figure 5-10 Mesh refinement near analytical rigid surfaces representing the rollers. While the roller is modelled as a perfect cylinder, the user interface of Abaqus represents it as a faceted surface.

In Figure 5-11, the mesh is shown projected onto the real specimen, with important locations magnified. Note the refinement in the area where the crack is expected to grow and the curved mesh along the fatigue pre-crack. In the planes where the crack is present in the specimen, the mesh has a constant cubic element size.

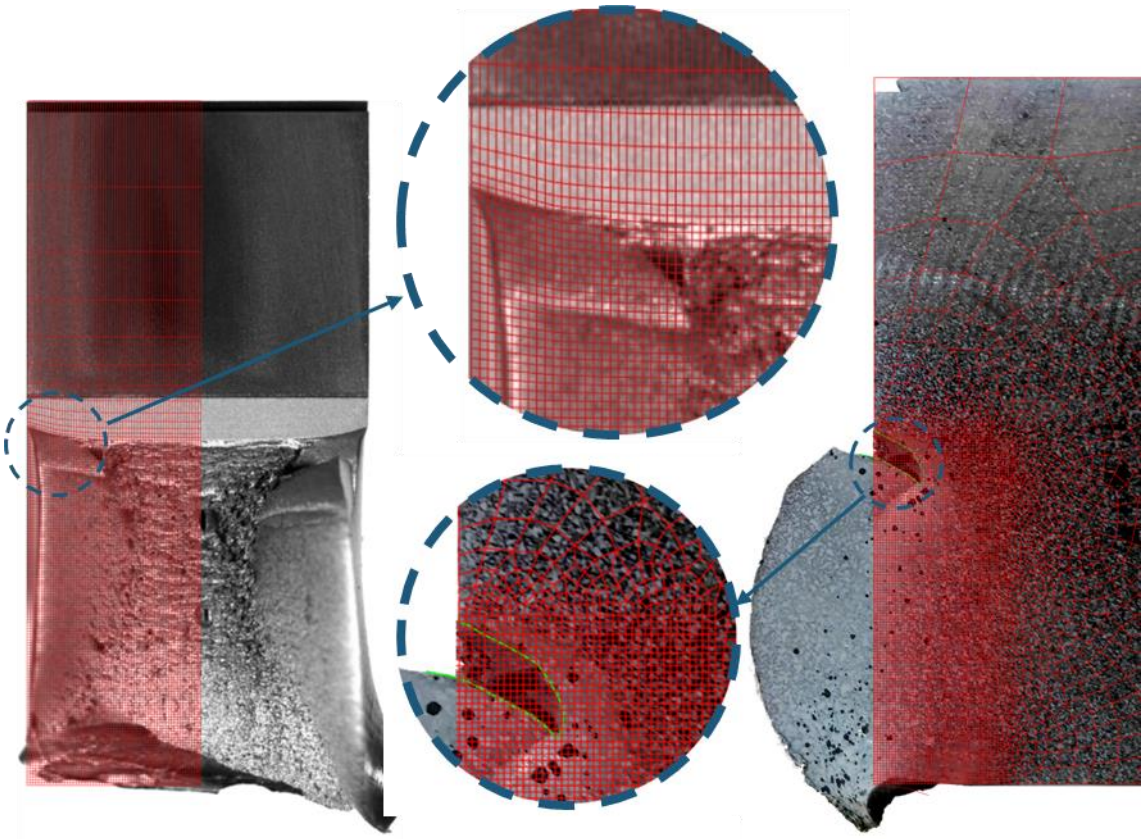

Figure 5-11 Mesh with 0.2mm element size projected on specimen. (Left)The mesh is curved along the fatigue pre-crack, as shown in the crack plane. (Right) The crack in the specimen is highlighted in green and covers about 60 elements along its path, as shown by looking at the side.

The mesh near the crack tip requires some additional explanation. Since the crack tip is the end of the fatigue pre-crack, it is often assumed that the radius of the tip is infinitely small. This is usually combined with a symmetry boundary condition on the yz-plane, effectively cutting the specimen in half along the x-direction. It was established that due to the existence of the shear lips, which grow asymmetrically, this is not the best way to create the model. The advantage of meshing both the negative x-domain as the positive x-domain in Figure 5-9 is that there is a little more freedom with meshing the crack tip. For example, a mesh such as presented in Figure 5-12 (right) is impossible with a symmetry boundary condition in the yz-plane.

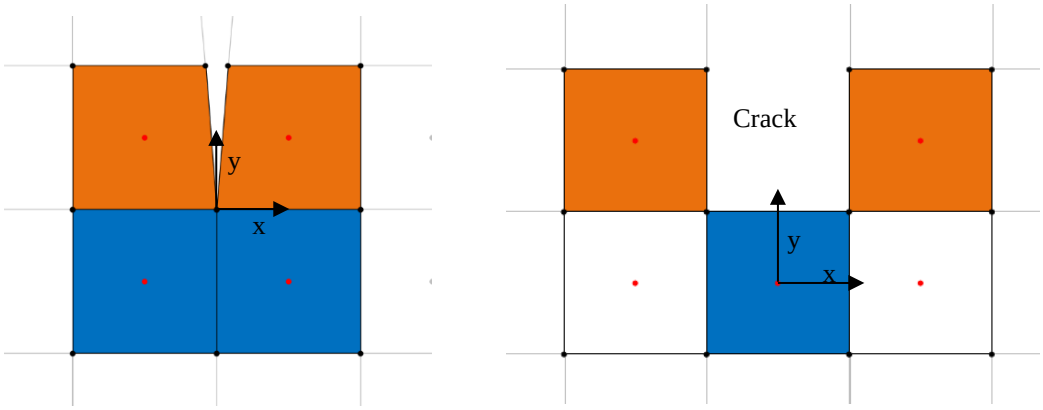

Figure 5-12 (left) Infinitely small crack tip, (right) crack tip that is one element wide

The mesh of the crack tip is important for a few reasons. First, in steel such as used in this thesis, considerable blunting of the crack tip occurs before the crack propagates due to plastic deformation. The mesh as presented in Figure 5-12 (left), where the crack terminates in a node, can accommodate blunting only at some distance from the termination node. By design, the actual width of the crack-tip in the origin is always infinitely small in that model. In the modelling of the crack by using a crack that is one element wide, a blunt crack tip is assumed, which can become blunter as the blue element deforms. Secondly, the stress states of both configurations are very different as well. In Figure 5-13, the stress states are plotted for elements along the crack front in the z-direction, from the centre in the thickness direction to the free surface. To create this plot, models were made with elements with the same size (0.2mm), and the analyses were halted at the same CMOD of 0.7mm. The number of elements along the z-axis, from the centre of the thickness of the specimen to the free surface, is 31. From these graphs, a few observations can be made. First, both configurations show that the highest stress triaxiality can be found in the centre element. Considering the effect of constraint, as explained in chapter 3, this is no surprise. The slightly higher value of stress triaxiality in the element wide crack is mainly caused by a numerical effect, namely that the integration point of the element in the ligament direction is exactly in the direction of the ligament. This is where one would theoretically expect a higher stress triaxiality (see the HRR field in chapter 3). Secondly, the trend in stress triaxiality is roughly the same along the z-axis, with both configuration showing descending stress triaxialities. In Table 5-2 and Table 5-3, the stress states at the extremities of the model are presented, for elements in the ligament or y-direction and elements in the crack flank or x-direction respectively.

Table 5-2 Stress and strain states in numbers for the elements on the crack tip

Ligament direction	**Nodal crack tip**		**Element crack tip**	
	Z=0	Free surface	Z=0	Free surface
Stress triaxiality	1.87	0.63	1.91	0.81
Lode angle	0.04	0.46	0.00	0.32
Equivalent plastic strain	0.07	0.07	0.25	0.15

Table 5-3 Stress and strain states in numbers for the elements on the crack flank

Flank direction	**Nodal crack tip**		**Element crack tip**	
	Z=0	Free surface	Z=0	Free surface
Stress triaxiality	1.11	0.47	1.12	0.38
Lode angle	0.02	0.21	0.00	0.25
Equivalent plastic strain	0.18	0.23	0.18	0.20

While in both configurations the element at z=0 has a very small Lode angle, the configuration with the element-wide crack tip is the closest to the plane strain state. Furthermore, the element-wide crack configuration shows the smallest stress triaxiality at the free surface. Another interesting observation can be made about the equivalent plastic strain. Focussing on the infinitely small crack tip, one can see that anywhere along the crack front, the elements on the crack flank show the highest plastic strain. Using a failure criterion based solely on maximum strain, this would mean that in simulations, the crack always grows in the x-direction. From the experiments and theory however, we know that that is not true. For the elements in the ligament direction to fail at z=0, one would therefore need a strong dependency of the stress triaxiality

on the strain to failure. Johnson and Cook showed the necessity for a stress triaxiality dependent failure model in 1985 (Johnson & Cook, 1985). The necessity of the Lode angle as variable in the failure strain, together with the stress triaxiality was shown by (Xue, 2007). Knowing that the crack starts growing at the location of the highest stress triaxiality, it is important to notice that the graphs in Figure 5-13 change as the crack grows in both ligament and z-direction.

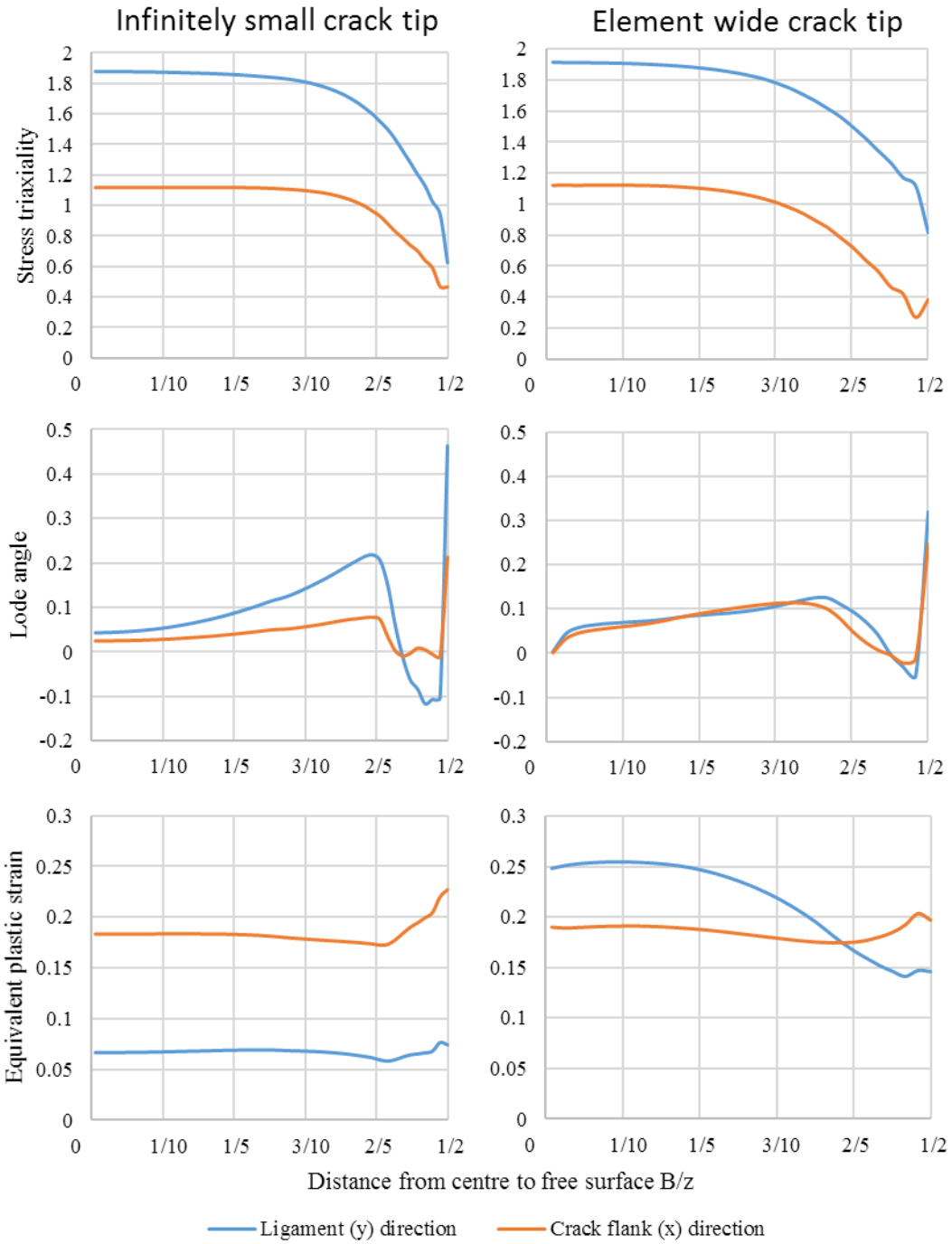

Figure 5-13 Stress states in elements on the crack front along the z-direction (centre to free surface). (left) is the case of the infinite crack tip, (right) the case of the element wide crack tip. The colours of the lines correspond to the elements in Figure 5-12 (blue lines indicate elements on the crack tip, orange lines represent the elements on the crack flank).

The configuration with the infinitely small crack-tip suffers from a problem that is not so straightforward at first sight. Consider again Figure 5-12, at z=0. To simulate tunnelling of the crack, the growth straight in the ligament direction, either of the blue elements needs to fail. Since this is a fully symmetric mesh, it might even happen that both blue elements fail at the same time. The crack tip however remains sharp,

because the node where the pre-crack ends is still connected to the two elements in x-direction (orange). This results in no measurable decrease in bearing capacity, which is assumed to be a major characteristic of crack growth. Consequently, for the crack to propagate in the ligament direction and simulate a decrease in bearing capacity, an element in x-direction needs to fail as well as an element in ligament direction. Needing an element in the crack flank to fail, as well as in the ligament direction, forces the crack to grow asymmetrically with respect to the xy-plane of the specimen. Stresses and strains concentrate in the tip of the new crack, which causes a crack path to be forced by the mesh. The configuration with the crack tip that is one element wide does not suffer from that problem. Tunnelling can be achieved by failure in elements in ligament direction, while the growth of shear lips can be achieved by failure of the flanking elements.

For the reasons presented above, the crack tip that is one element wide is chosen over the infinitely sharp crack tip, despite the obviously less accurate simulation before the blunting phase of the real crack tip. It was discovered that despite the introduced bluntness of the crack, very little difference was found in the force-displacement curve before plastic flow occurred.

5.2.3 Analysis

The finite element simulation of the SENB experiment requires an accurate geometry and mesh, with refinements at appropriate locations in the model. The complicated parts of the model are the contact regions where the rollers touch the surface of the beam and the area where the crack is expected to grow. The physical growth of the crack is modelled using the technique of damage mechanics, as is explained globally in paragraph 2.3 and for this approach in the next paragraph. The approach of continuum damage mechanics taken in this thesis requires the use of an explicit integration scheme. This requirement arises because it is not practical to define a consistent tangent stiffness matrix when an element is severely damaged and therefore this will cause convergence problems with an implicit time integration scheme. When using an explicit integration scheme, the problem of a singularity in the stiffness matrix at system level is avoided, since the tangent element stiffness matrix is used. The introduction of an explicit time integration scheme however introduces several problems that need to be considered. First, in an explicit analysis the equilibrium is not strictly enforced, simply because the exact path of the equilibrium is unknown. As long as the time step is very little, this doesn't cause any problems. Secondly, for a non-linear analysis the time step must be even smaller to ensure an accurate solution. For linear problems, this time step is dependent on the highest frequency (smallest eigenvalue) of a specific element, where the smallest element is the most critical. For a nonlinear problem, the step time has to be even smaller than that, resulting in long calculation times. Small errors that arise due to strong nonlinearities are not corrected for and will accumulate into larger errors. The finite element software Abaqus/Explicit introduces a small amount of damping to the calculation of the stable time increment, ensuring that the time step is always smaller than what is derived using the element's smallest eigenvalue.
The rollers are simulated as analytical rigid surfaces and come into frictionless contact with the beam using the Abaqus built-in general contact definition for element based surfaces. This particular contact algorithm uses the penalty approach, which counters the penetration of the roller into the beam by introducing reaction forces. Any contact algorithm in Abaqus/Explicit uses a critical dampening factor of 0.03 by default to reduce solution noise, and this is left untouched. (Dassault Systèmes, 2014).

5.2.4 Damage model

In chapter 2.3 the theory behind the damage mechanics is briefly outlined, while in this paragraph the application theory that is unique to this thesis is explained. In the continuum damage approach taken here, the growth of a crack through an element is modelled by voiding the response of the element normal to the plane in which the crack grows. Consider the eight-node three-dimensional finite element with one integration point presented in Figure 5-14.

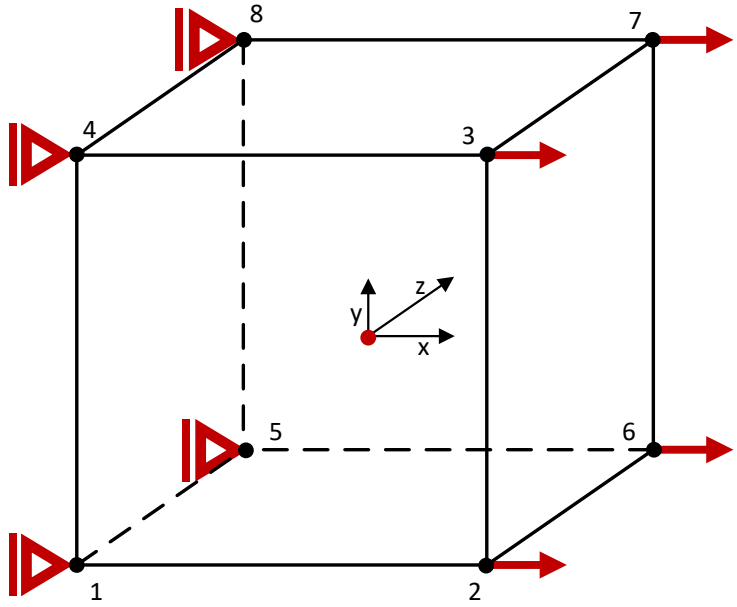

Figure 5-14 Linear brick finite element under tension. Black nodes indicate nodes, the red centre dot is the integration point.

A velocity of 0.006 m/s^2 is applied to the nodes with a positive x-coordinate, while the nodes with a negative x-coordinate constrain translations in x-direction. The origin of the coordinate system is given in the integration point and this represents a co-rotational coordinate system, which rotates with the material. The velocity applied to the nodes with positive x-coordinate causes a state of uniaxial tension in the element. Figure 5-15 shows the development of the first principal stress as a function of the total strain in x-direction. The direction and magnitude of the maximum principal stress in this state are equal to the stress in x-direction.

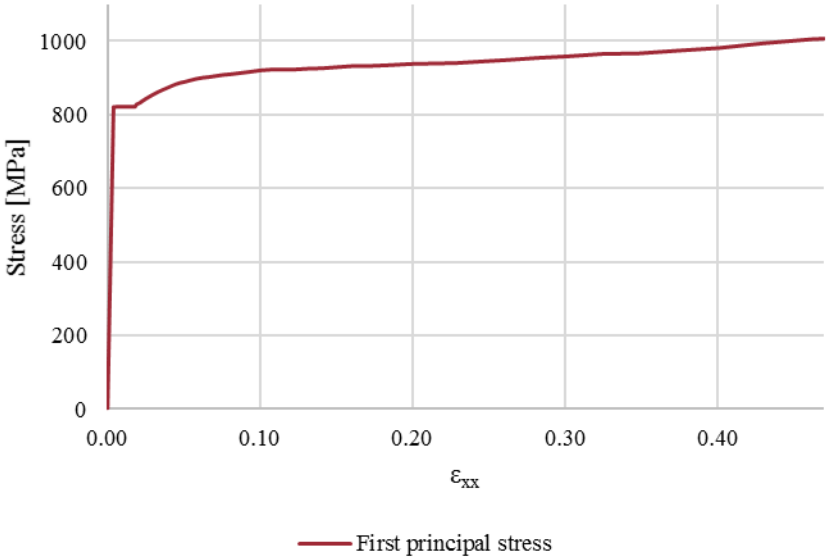

Figure 5-15 Principal stresses in elastic-plastic single finite element in uniaxial tension

This stress state can, alternatively, be described by the Lode angle, stress triaxiality and equivalent plastic strain as was explained in chapter 2.3. The Lode angle in this specific case has a known and constant value

of 1, while the stress triaxiality is also known to be 1/3 (see Figure 2-5). If for this stress state a failure strain is defined, the element will be damaged as soon as this failure strain is reached. This procedure is described in the following paragraph through an example.

The damaging of the element starts when a certain combination of stress triaxiality, Lode angle and equivalent plastic strain is reached. Let ε_d be the equivalent plastic strain at which damage is initiated. The stress state now that ε_d is reached, can be described by the stress triaxiality at damage initiation (η_d) and normalized Lode angle (θ_d). At this moment, it is assumed that a crack grows in the plane that has the greatest tensile principal stress normal to it. In the considered cube of Figure 5-14, this is the first principal stress as can be seen in Figure 5-15. For different states of stress, the principal stresses and their direction vectors with respect to the element (or material) coordinate system can be calculated as respectively the eigenvalues and eigenvectors of the current stress matrix. It is assumed that during the growth of the crack along this plane and in fully cracked condition, the direction of the plane remains constant relative to the material basis. As the fictitious crack progresses along the crack plane, the resistance of the element to further straining normal to that plane decreases. At the moment that the crack has grown to another face of the element, the capacity to resist straining normal to the crack plane has diminished. Shear stresses that resist deformation normal to the crack plane, share this deterioration. The existence of a crack also means that further straining normal to the crack plane does not have any effect on the transversal contraction or contraction due to the Poisson effect or conservation of volume. The Poisson effect of strains in the damaged direction to other stresses decreases to zero as the crack reaches the other face of the element. Please note that this also means that the conservation of volume is not enforced anymore. This approach bears much resemblance to the fixed smeared-crack model introduced by Y.R. Rashid in modelling of concrete (Rashid, 1968) and later smeared crack models, with two major differences.
The first of the major differences has to do with the relationship between strain and stress in modelling. Classic smeared crack models are based on the total strain concept, meaning that at any moment in time the stress can be found by multiplying the strain with a (damaged) stiffness matrix. In this case, it is impossible to combine cracking or damage with plasticity and or other nonlinear effects. In the approach taken in this thesis, stress is calculated using an additive formulation. Here the stress resulting from the strain increment in the current time step is added to the stress from all previous time steps. This process is shown in equation **(** 5.1) for the trial stress calculated in the elastic phase in the material model. Again, μ and λ are the Lamé parameters.

$$\sigma_t^{trial} = \begin{bmatrix} \sigma_{xx}^t \\ \sigma_{yy}^t \\ \sigma_{zz}^t \\ \sigma_{xy}^t \\ \sigma_{yz}^t \\ \sigma_{zx}^t \end{bmatrix} = \begin{bmatrix} \sigma_{xx}^{t-\Delta t} \\ \sigma_{yy}^{t-\Delta t} \\ \sigma_{zz}^{t-\Delta t} \\ \sigma_{xy}^{t-\Delta t} \\ \sigma_{yz}^{t-\Delta t} \\ \sigma_{zx}^{t-\Delta t} \end{bmatrix} + \begin{bmatrix} \lambda+2\mu & \lambda & \lambda & & & \\ \lambda & \lambda+2\mu & \lambda & & & \\ \lambda & \lambda & \lambda+2\mu & & & \\ & & & \mu & & \\ & & & & \mu & \\ & & & & & \mu \end{bmatrix} \begin{bmatrix} \Delta\varepsilon_{xx}^t \\ \Delta\varepsilon_{yy}^t \\ \Delta\varepsilon_{zz}^t \\ \Delta\varepsilon_{xy}^t \\ \Delta\varepsilon_{yz}^t \\ \Delta\varepsilon_{zx}^t \end{bmatrix} \quad (5.1)$$

The formulation of the current stress state as described above, together with a Newton-Raphson based return mapping algorithm for plastic deformation, allows the damage to be applied to only new time steps with their corresponding strain increments. Therefore, it is possible to combine plasticity with damage.
The second major difference with classic smeared crack models has to do with the direction of damage. In classic smeared crack approaches, the direction of the crack plane is fixed with respect to the global coordinate system. Since in this approach the element stiffness is used set within its own coordinate system instead of the global stiffness matrix, the plane of the crack rotates as the element rotates.

Consider again the element from Figure 5-14, but now a damage criterion is present in the form of a stress triaxiality (η_d) and Lode angle (θ_d) dependent equivalent plastic strain (ε_d). In Figure 5-16, the development of maximum principal stress in the simulation without damage and with damage is shown.

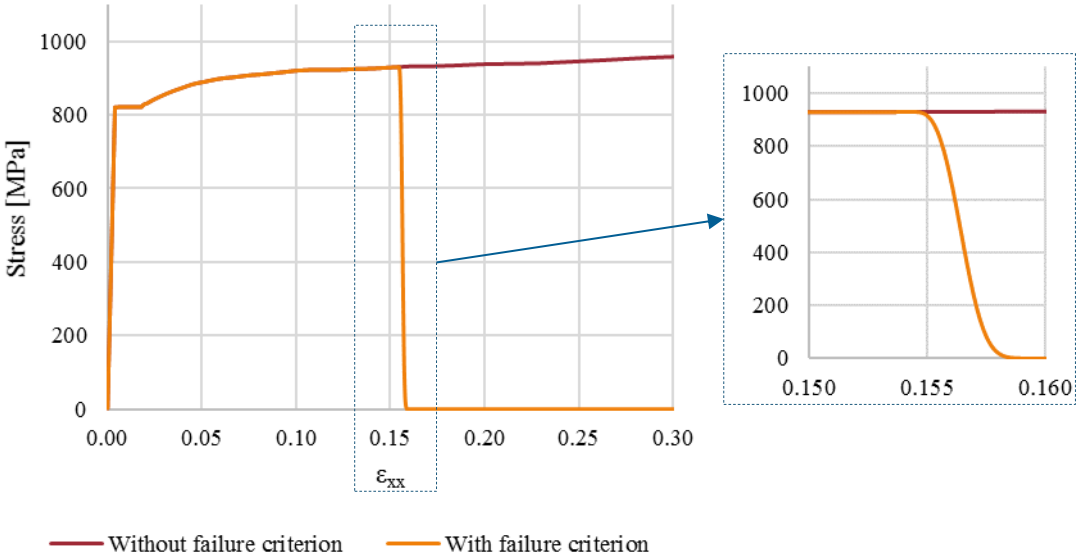

Figure 5-16 First principal stress of simulation without failure criterion and with failure criterion ε_d=0.15 and D_f=0.16/0.15.

The transition from undamaged to fully damaged is emphasised in Figure 5-16. This smooth transition, in which the first principal stress is decreased to zero, is the result of the damage evolution function. In chapter 2.3, the damage evolution function was introduced with the following formula:

$$\tilde{\sigma} = \omega * \sigma \qquad (5.2)$$

In this formula, $\tilde{\sigma}$ is the softened stress tensor, and σ is the stress tensor without damage applied. The damage tensor ω is a function of damage parameter (D) in the range from 1 to D_f. D_f is a value greater than 1 at which point the element can no longer sustain a stress (in a particular direction). The fictitious crack plane and resulting material orthotropic is accomplished using the damage tensor ω, where all values except the value corresponding to the direction normal to the fictitious crack are zero. The non-zero value follows the damage evolution laws presented in equation (5.3) and (5.4). The value of D is determined through the following formula (Johnson & Cook, 1985):

$$D(\bar{\varepsilon}_p) = \int_0^{\varepsilon_p} \frac{d\bar{\varepsilon}_p}{f(\eta, \bar{\theta})} \qquad (5.3)$$

The value of f is a failure strain dependent on the Lode angle and stress triaxiality. In the case of the calibration procedure, f consists of a locus of points, while in the application procedure f represents the Hosford-Coulomb model. Basically, the value of D represents how far along the path to failure (f) an element is. As soon as D is equal to one and therefore the element has reached the end of the path to failure, the softening parameter ω reduces from 1 to 0, thereby reducing the effective stress to 0, using the following formula:

$$\omega = \frac{2(D-1)^3}{3 * D_f} - \frac{3(D-1)^2}{2 * D_f} + 1 \qquad (5.4)$$

To remain within the scope of this research project, of which the development of this damage function is just a side-track, no attention is given the effect of softening parameter D_f. This parameter, controlling the softening rate, is set in such a way that full damage (w=0) is applied over a very short range of D. As was mentioned in the scope in the introduction, damage evolution has been the topic in a great many research projects. To limit the influence of this on the calibration and application method presented here, the range of D is great enough to ensure a stable solution in the return mapping algorithm, but short enough to make the onset of full damage seem instantaneous.

This damage evolution function is specifically designed to facilitate a smooth decrease in effective stress, in order to reduce the dynamic effect of this loss of bearing capacity, but has no further physical meaning. Equation (5.4) is visualised in Figure 5-17.

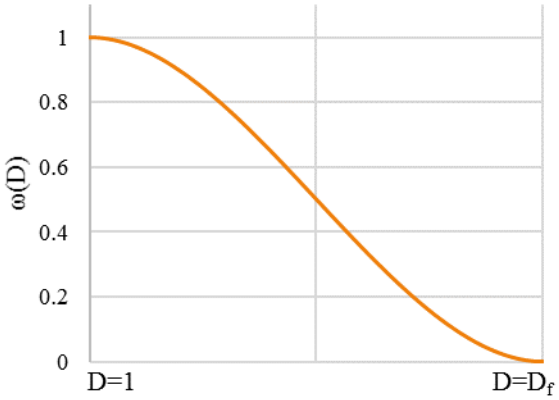

Figure 5-17 Evolution of the softening parameter as a function of D according to equation (5.4) .

This procedure results in the deformed shape of the element presented in Figure 5-14, of which the development of the first principal stress was shown in Figure 5-16, is shown in Figure 5-18.

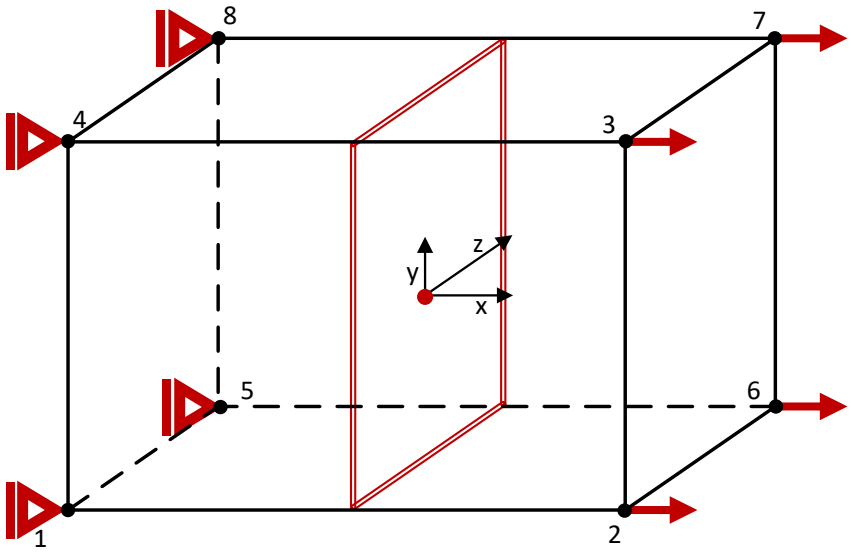

Figure 5-18 Deformed shape of the uniaxially loaded element, with fictitious fracture plane marked with double red lines at D=D_f.

The fictitious crack plane, normal to the maximum principal stress and intersecting with the integration point is shown as a double red line. Any additional strains in the x direction in this state have no effect on stresses in any direction. Due to the visualisation of the damage procedure using a fictitious crack plane normal to the maximum principal stress, this damaged model will be referred to as the fictitious crack damage (FCD) model. This is not the first damage model that is envisioned from the viewpoint of a fictitious crack. Among others, (Hillenborg, 1991) introduced the fictitious crack model based on an energy approach. The FCD model used here is not as sophisticated as Hillenborg's, but finds an application in 3D and allows easy numerical evaluation.

The reason that, besides the damage applied to the stress tensor, the strain increments in the damaged direction are voided, can be found when looking at the calculation of the trial stresses. In equation (5.5), the calculation of the trial stress in y-direction is shown, expanded from **(** 5.1).

$$\sigma_{yy}^{t} = \sigma_{yy}^{t-\Delta t} + (\lambda + 2\mu)\Delta\varepsilon_{yy}^{\Delta t} + \lambda\Delta\varepsilon_{xx}^{\Delta t} + \lambda\Delta\varepsilon_{zz}^{\Delta t} \quad (5.5)$$

The damage applied to the stresses in x-direction, causes the strain in x direction to be allowed to grow with little resistance. This then causes an enormous increase to stresses in the transverse direction, due to the term in the trials stress calculation containing the strain in x-direction. This is deemed unrealistic from the viewpoint of the fictitious crack, and therefore the strains in the damaged direction are voided. Consequently, the conservation of volume is lost, which is shown in Figure 5-19.

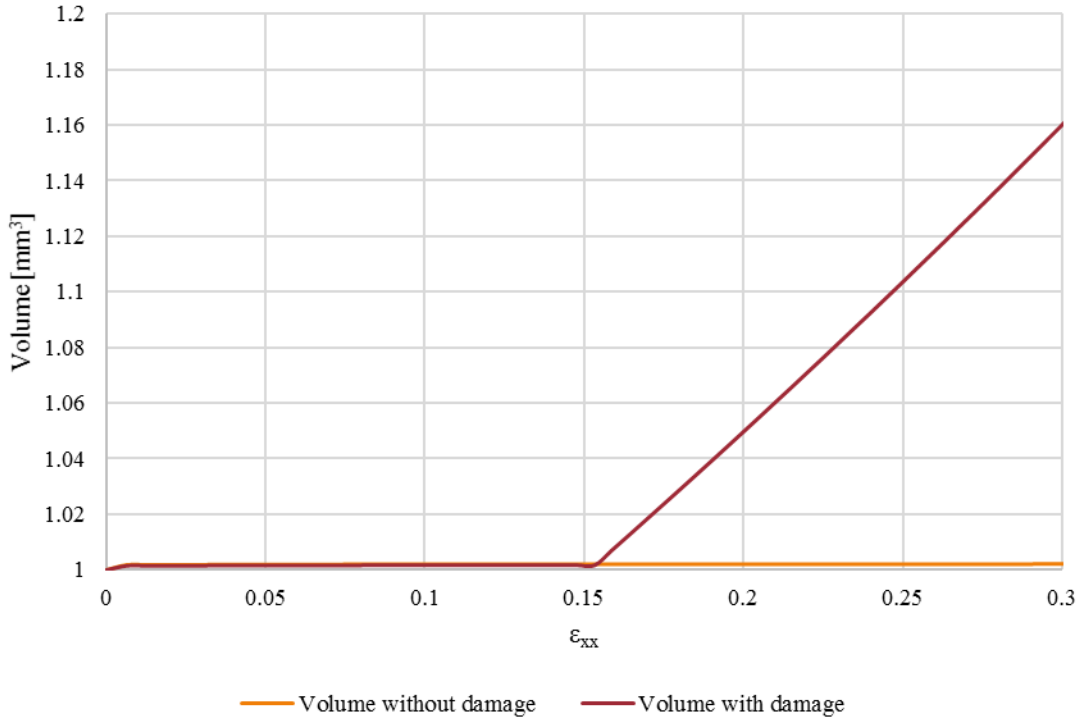

Figure 5-19 Volume of element in uniaxial tension without and with damage criterion.

It must be noted that at this time no elastic relaxation due to the existence of the fictitious crack is included in the model. One could expect that due to a loss of all stiffness in x-direction, the part of the stress in transverse directions that resulted from the elastic strain in x-direction should experience elastic relaxation. A damage model where this is incorporated was also devised, but not used in this thesis, because of a severely decreased step time or sub-stepping algorithm that is needed to avoid convergence problems in the return mapping algorithm.

5.2.5 Damage model motivation

The reason that the choice was made to use this damage model, instead of a more conventional isotropic damage model with or without element deletion, is discussed in this paragraph. The motivation comes from observations made while using the isotropic damage model to calibrate the specimen. Consider the deformed state of the element wide crack-tip Figure 5-12, shown in Figure 5-20. Element number 1 is assumed to fail first, as is explained in chapter 5.3.1.3. Consider the element being damaged by an isotropic damage model, meaning that it loses the ability to resist deformation in any direction.

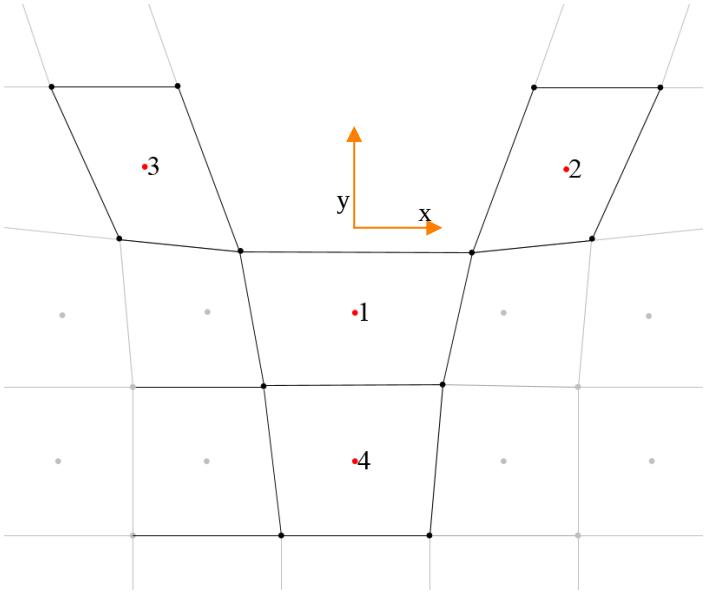

Figure 5-20 Deformed state of the element wide crack-tip at z=0 (xy-symmetry plane).

The effect of the fully damaged element 1 on element number 4 in terms of stress state is shown in Table 5-4. The fully damaged state of element 1 means that element 4 is now the element that is on the crack tip in ligament direction. For this reason, one would expect that the stress state in element 4 after element 1 is fully damaged is similar to the stress state in element 1 before any damage occurred. In Table 5-4, one can see that that is not the case. The loss of stress triaxiality and significant change in Lode angle is caused by loss of constraint in element 4, due to the isotropic damage applied to element 1.

Table 5-4 Stress state in elements 1 and 4 for intact and fully damaged state of element 1 using isotropic damage.

El.	Parameter	No damage (ω=1)	Fully damaged (ω=0)
1	Lode Angle ($\bar{\theta}$)	0	-
	Stress Triaxiality (η)	1.9	-
4	Lode Angle ($\bar{\theta}$)	0.3	-0.6
	Stress Triaxiality (η)	1.5	1.2

Recreating the same table with the FCD model results in the stress states presented in Table 5-5. Instead of a loss of constraint, element 4 shows an increase in constraint and a Lode angle that signifies plane strain. This essentially means that the element that is now on the crack tip in ligament direction, has a similar stress state as the element that was previously at the crack tip in ligament direction, albeit with a smaller stress triaxiality. This is the main reason that the orthotropic FCD model is chosen over isotropic damage. From Table 5-5, the result of the FCD model on the damaged state of the element can be seen. The elimination of the response of the element to its largest principal strain significantly decreases the triaxiality of the damaged element and puts in in a state close to equibiaxial tension.

Table 5-5 Stress state in elements 1 and 4 for intact and fully damaged state of element 1 using the FCD model.

El.	Parameter	No damage ($\omega_{1,xx}$=1)	Fully damaged ($\omega_{1,xx}$=0)
1	Lode angle ($\bar{\theta}$)	0	-0.9
	Stress Triaxiality (η)	1.9	2/3
4	Lode angle ($\bar{\theta}$)	0.3	0
	Stress Triaxiality (η)	1.5	1.7

In the z-direction a similar trend can be seen. Consider the element behind element 1, which is the element closer to the free surface and neighbouring element 1. A huge jump in Lode angle is the result of element 1 being fully damaged. This is no surprise, since in case of the isotropic damage, the element gains a new

free surface and loses constraint. In the case of the fictitious crack damage (FCD) model, the increase in Lode angle is less severe, but still there. It is important to note that the stress state in this element is a direct consequence of using finite elements and is consequently very artificial. This means that, for the crack to propagate in z-direction, a damage criterion different from the first element is needed. While calibrated failure loci often show that there is a significant effect of the Lode angle on low stress triaxialities $0.3 < \eta < 0.6$ (see for example Figure 5-21), the Lode angle dependency for high stress triaxialities is much less significant or even absent. This observation in theory agrees well with the change of Lode angle experienced in this calibration procedure.

Table 5-6 Stress state in the second element on the crack front to fail, before (ω_1=1) and after (ω_1=0) the first one fails, with isotropic and orthotropic (FCD) damage accumulation. The second element to fail is on the crack front, located in the thickness (z) direction from the first element to fail.

	No damage (ω_1=1)	Fully damaged (ω_1=0)
$\bar{\theta}$ isotropic damage	0.08	0.78
η isotropic damage	1.8	2.0
$\bar{\theta}$ FCD	0.08	0.56
η FCD	1.8	2.0

5.2.6 Material parameters

The strain at which damage is initiated is a function of the Lode angle and stress triaxiality, as discussed in chapter 2.3. These failure combinations are both dependent on the material that is used, and the mesh size. In this research project a failure criterion in the modified Haigh-Westergaard stress space is used, but the failure strain corresponding to a triaxiality and Lode combination is not known *a priori*. This is where the damage calibration procedure comes in, which is explained in this chapter. An example of a fully calibrated failure criterion, or failure locus, is shown in Figure 5-21.

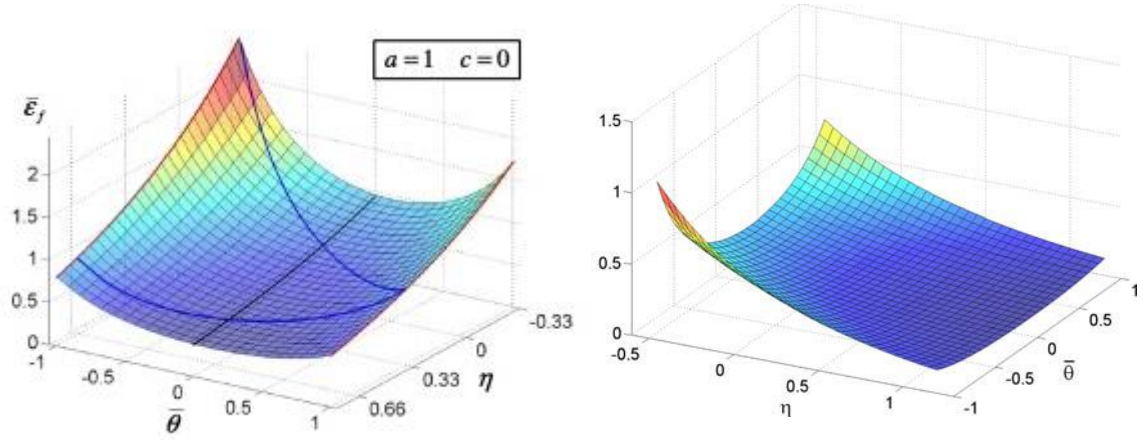

Figure 5-21 Example of failure loci in the modified Haigh Westergaard stress space for steel. The blue line is drawn through triaxiality-Lode combinations that signify plane stress. (Left (Mohr & Marcadet, 2015)), (Right (Bai & Wierzbicki, 2010))

There are various theories on the shape and formulae to describe a failure locus as shown in Figure 5-21. This particular failure locus is taken from the Hosford-Coulomb failure model to describe ductile fracture (Mohr & Marcadet, 2015). Some other models to describe the failure locus are Modified-Mohr-Coulomb (Y. Bai, 2008) and the triaxiality based model by Johnson and Cook. (Johnson & Cook, 1985). The power of the method explained in this thesis is that any of the above-mentioned damage models and more can be calibrated with the data points obtained in the iterative procedure.

The Hosford-Coulomb (HC) model, originally formulated by Coulomb in 1776, has the following form in Haigh-Westergaard coordinates (Mohr & Marcadet, 2015):

$$\bar{\sigma}_f = \frac{b}{\left(\frac{1}{2} * (f_1 - f_2)^a + (f_2 - f_3)^a + (f_1 - f_3)^a\right)^{\frac{1}{a}} + c(2\eta + f_1 + f_3)} \quad (5.6)$$

$$f_1 = \frac{2}{3}cos\left(\frac{\pi}{6}(1 - \bar{\theta})\right); f_2 = \frac{2}{3}cos\left(\frac{\pi}{6}(3 + \bar{\theta})\right); f_3 = -\frac{2}{3}cos\left(\frac{\pi}{6}(1 + \bar{\theta})\right) \quad (5.7)$$

$$\sigma_i = \bar{\sigma}(\eta + f_i) \qquad \text{where } \sigma_1 \geq \sigma_2 \geq \sigma_3 \quad (5.8)$$

In equation (5.6), three calibration parameters can be distinguished. Calibration parameter a is the Hosford exponent, which ranges between 0 and 2. Parameter b is a scaling parameter for the stress or strain (as a function of stress) to failure. Parameter c is known as the friction coefficient. Together, parameter a and c can make combinations that relate the HC to other well-known models:

1. For a=2 and c=0 the Von Mises model is obtained.
2. For a=1, the Mohr-Coulomb model is obtained.

How the principal stresses are related to the von Mises stress ($\bar{\sigma}$), Lode angle and stress triaxiality can be seen in (5.8). The stress to failure is converted to plastic strain to failure, using the piecewise interpolation obtained in chapter 4, but other functions (such as Swift's power law) can also be used.

5.3 Calibration procedure

Now that a clear target has been set, namely finding the calibration parameters (a, b and c) of the Hosford-Coulomb model, it is time to introduce the calibration procedure. This procedure is used to find the locus of failure combinations, introduced in 5.2.5 as the function $f(\eta, \bar{\theta})$. When enough points on the failure locus have been found, the HC model can be fitted using its calibration parameters (a, b and c).

5.3.1 Global procedure

The entire procedure can be described globally by the following flowchart:

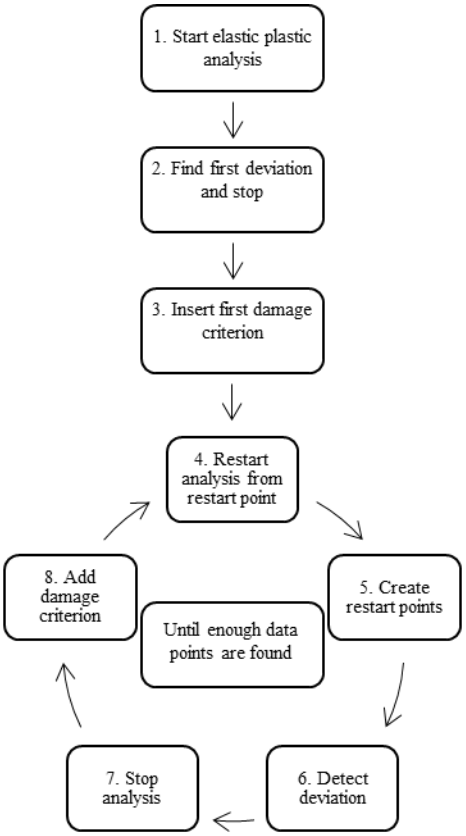

Figure 5-22 Global calibration procedure

In the following paragraphs, every step of this procedure is detailed. Every step is fully automated, except for the end of the cycle of steps 4 through 8. This cycle is stopped at the moment that the user determines that enough data points have been obtained to create a reliable fit. The automation of the various steps is handled using a Matlab framework, that carries out various tasks, from pre-processing to postprocessing and starting Abaqus jobs.

5.3.1.1 Elastic plastic analysis

The finite element model, as described in chapter 5.2, is run with the plasticity model included. At this point in the procedure, this is a regular elastic-plastic analysis. During step 1, the force and CMOD of the simulated specimen is continuously compared to the experimental data using Abaqus user subroutine VUAMP. Restart points are created at every increase of CMOD by 0.1 and, as soon as forces in the simulation have exceeded the experimental values by more than 0.8%, every 5000 time increments.

5.3.1.2 First deviation and stop

As soon as the force for the current CMOD in the simulation exceeds the force measured in the experiment for the same CMOD by a certain percentage, the analysis is stopped by the user subroutine VUAMP. This

is the crucial point at which it is assumed that the deviation between the simulation and experiment is caused by crack growth. The deviation criteria and the influence of the mesh size on it, is discussed in chapter 5.3.2. In the calibration procedure, the critical deviation is set to 1%.

5.3.1.3 Insertion of first damage criterion

The results from the elastic-plastic analysis are postprocessed and the stress state and equivalent plastic strain of the critical element, at 4000 time increments before the deviation occurs, is extracted. This stress state becomes the first damage criterion and is inserted in the material subroutine VUMAT. The reason that the element on the crack front and on the symmetry plane, in ligament direction, is chosen as the critical element, can be found through both theory and experimental observations. Looking at stress states, this element is in a state of stress with the highest stress triaxiality, the smallest Lode angle and one of the highest equivalent plastic strains along the crack front. Many calibrated failure loci show that elements with a high stress triaxiality and/or small Lode angle fail at lower equivalent plastic strain (EPS) than elements with low stress triaxialities (η) and/or high normalized Lode angles ($\bar{\theta}$) (Johnson & Cook, 1985), (Gu & Mohr, 2015), (Xue, 2007) , (Bai & Wierzbicki, 2008).

5.3.1.4 Restarting the analysis from the last restart point

The subroutines are recompiled, so that now the new damage criterion is included, and used to restart the analysis from the last restart point created in 5.3.1.2.

5.3.1.5 Creating restart points

Like in the elastic-plastic simulation, it is important to generate new restart points to accommodate later restarts. Like in the elastic plastic step, restarts points are made with an interval of 5000 load increments after 0.8% deviation.

5.3.1.6 Deviation detection

Like in 5.3.1.2, the simulated force and CMOD are continuously compared against the experimental values. As soon as the experimental values are exceeded by more than 1%, the analysis is stopped.

5.3.1.7 Stopping the analysis

The analysis is stopped and values are post-processed in the Matlab framework.

5.3.1.8 Adding the new damage criterion

Now, the neighbours of elements that are damaged are evaluated. The stress state of the neighbour that has the highest plastic strain, is selected as the new damage criterion and is saved to be included in the subroutine which will be recompiled in step 4.

This cycle continues until it is halted by the user.

5.3.2 Experiment-model deviation criteria

The deviation criterion is chosen to be 1% during the calibration. In Figure 5-23, the force-CMOD graphs for the experiment and various simulations is shown. First it had to be established that the deviation is not mesh size dependent. Figure 5-23 Shows that the CMOD for which the deviation occurs, is very similar for the meshes with 0.1,0.2 and 0.3mm characteristic element length. From this point onwards (CMOD>0.75), the difference in gradient between the simulations and the experiment only becomes larger. Other than that, the choice for a deviation of 1% is arbitrary to some point. It was found that decreasing the deviation criteria only resulted in slightly smaller equivalent plastic strains, for almost identical stress states. The effect of the deviation criteria will be most noticeable during the application of the calibrated model and is discussed in chapter 6.

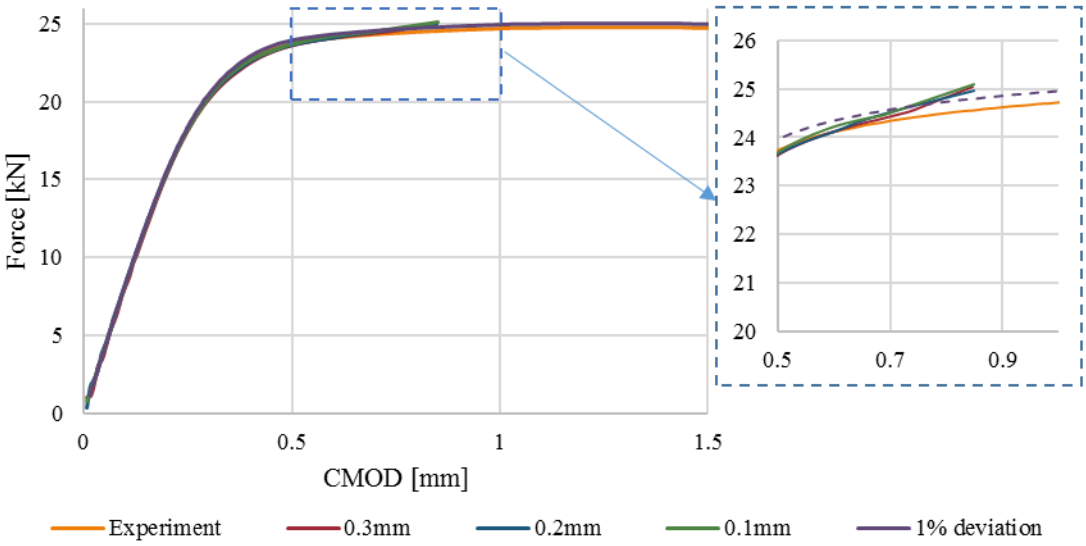

Figure 5-23 Force-CMOD curves for simulations with various mesh sizes, experiment and 1% deviation criterion (dotted line) for the 12x24mmortional specimen.

The values of the stress states for the different meshes are summarised in Table 5-7. From this table, the influence of the mesh size on the stress state of the centre element is shown. While the stress states are very similar, the equivalent plastic strain shows a very strong dependency on the mesh size. This is to be expected, and another reason to emphasize that any calibrated model is valid only for one element size, in the region where damage is expected. On the other hand, it shows that it might be possible to calibrate the damage model on one mesh size, and use damage parameter b from equation (5.6) to scale the damage model by multiplying it with the ratio between plastic strain shown in Table 5-7.

Table 5-7 Mesh details in calibration procedure

Element size	0.3mm	0.2mm	0.1mm
CMOD at deviation	0.764 mm	0.745 mm	0.746 mm
$\bar{\varepsilon}_p$ in element 1	0.186	0.247	0.491
η in element 1	1.91	1.89	1.90
$\bar{\theta}$ in element 1	0.05	0.03	-0.02
Elements	91161	200942	548018

5.4 Calibration of the damage model

The calibration of the damage model is done as soon as it is determined that doing more calibration steps, continuing the cycle of steps 4-8 in Figure 5-22, will yield no more new data points. From the stress states along the z-axis, as shown in Figure 5-13, it can be concluded that a great number of stress states is found along the crack front. The domain in which stress states are expected to be found if the calibration cycle is

continued until the simulated crack has reached the free surface, is shown in Table 5-8. These values are the upper and lower values that were presented in Table 5-2.

Table 5-8 Boundaries of stress states from static situation before any damage occurred.

	Element crack tip	
	Lower	Upper
Stress triaxiality	0.81	1.91
Lode angle	0.00	0.32

Crack growth, simulated by damaged elements, can create stress states that are outside of the domain presented in Table 5-8, as was explained in chapter 5.2.5. This means that in the domain in which Lode angles are expected to be found is between 0 and 0.8. After 80 calibration cycles and therefore 80 damage criteria, failure strains were found for the stress states presented in Figure 5-24. A distinction has been made between elements in ligament direction and elements in x-direction. The crack can be considered initially to grow in 2 directions from the first element. Elements that simulate crack growth in the thickness (z-direction), meet failure criteria along the black path in Figure 5-24. The black path starts at high triaxiality plane strain and progresses in z-direction through failure criteria with similar stress triaxiality but higher Lode angles. This is caused by the effect explained in chapter 5.2.5, where neighbouring elements experience jumps in Lode angle due to their damaged neighbour. Similar failure criteria are found until about halfway along the z-axis, from where descending triaxialities and Lode angles are found. At a certain point (~80% along the z-axis), the elements in the flank experience higher plastic strains than the elements in the ligament direction and as such the crack orientation changes from the ligament direction to the x-direction. This becomes more and more clear as the crack progresses towards the free surface, where the elements are almost in a state of plane stress. Meanwhile, the growth in y-direction (ligament) continues and more failure combinations are found near the plane strain line and for higher Lode angles for high stress triaxialities. From this point onwards, with a crack that has fully developed to the free surface and deeper into the ligament and flanks, very little failure combinations are found that provide new information.

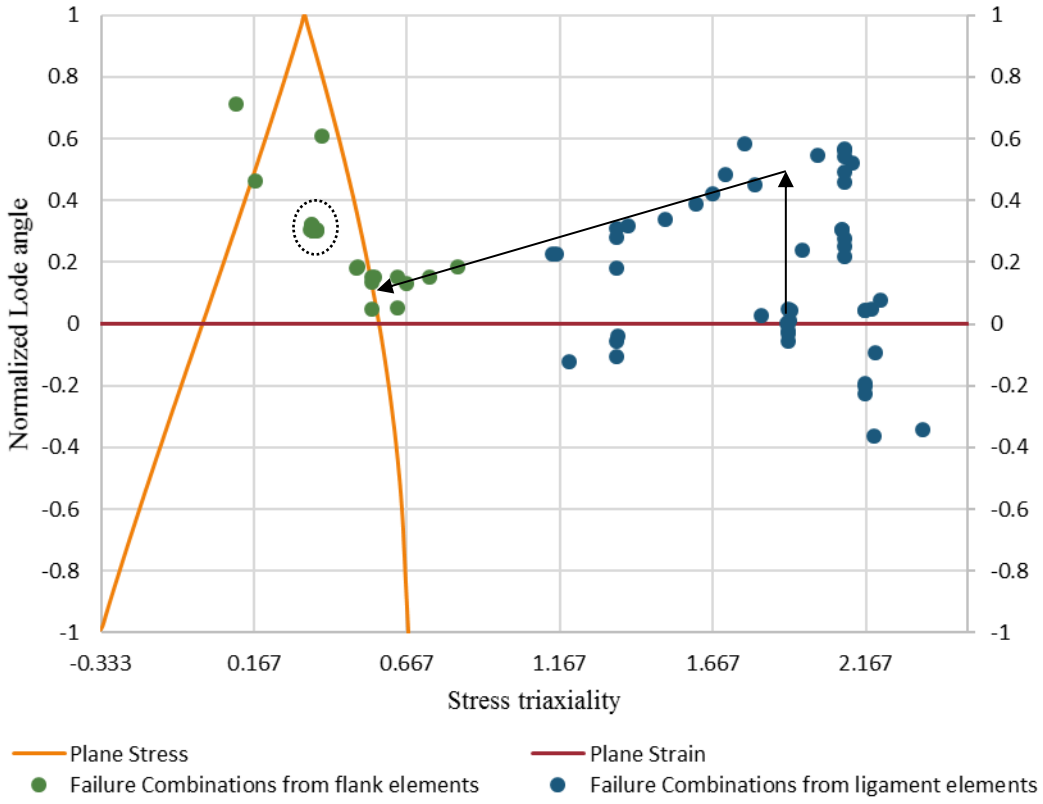

Figure 5-24 Failure criteria resulting from 80 cycles of the calibration procedure.

There is one important other aspect to notice from Figure 5-24, namely the failure criteria from flank elements that are indicated by a black circle. These failure criteria result from elements that have a great amount of plastic strain, but are not in a position where failure was expected. This can best be explained by looking at a part of the model around the crack tip, shown in Figure 5-25.

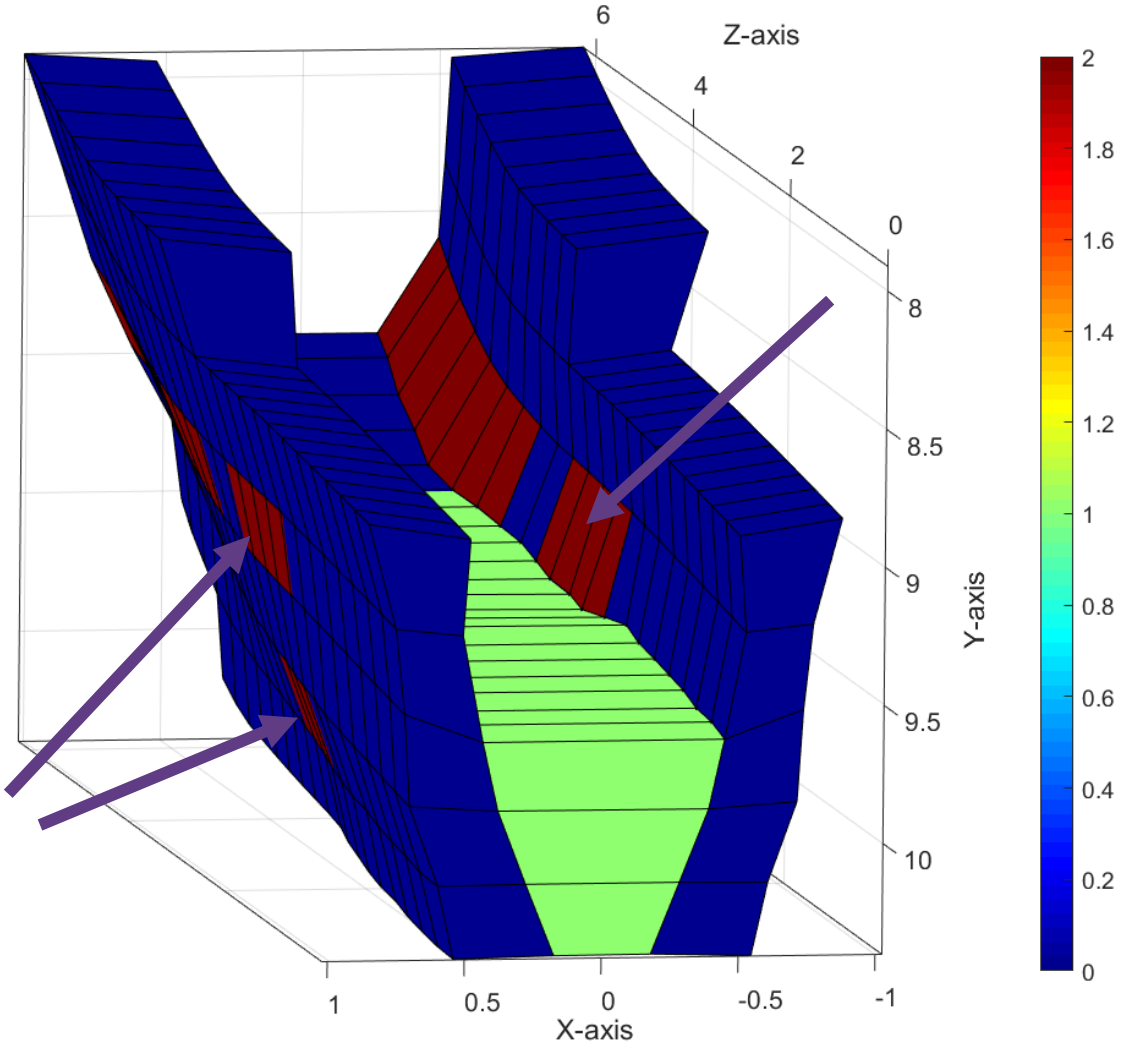

Figure 5-25 Part of the model around the crack tip, looking from the symmetry plane (z=0) along the z-axis to the free surface (z=6.25). Only elements that directly border the crack are displayed. The colours give an indication of the damaged direction, where blue indicates undamaged elements, greenish indicates elements damaged approximately in x-direction and red elements are damaged in approximately the y-direction.

At this time, there is fully symmetric damage, and therefore crack growth, for the positive and negative x-domain. A crack has developed at the locations indicated by the purple arrows and soon after that, this crack starts growing towards z=0. A crack in x-direction near the symmetry plane is not observed in any examined specimen, so this presents a discrepancy between reality and the calibration. For further use, they will be referred to as conflicting elements. An explanation for the high plastic strains, that caused these elements to generate a failure criterion, can be found looking at their stress states. These elements on the crack flank are in a state of shear. Since the von Mises yield criterion is used, yielding occurs for lower stresses in shear than in tension. The failure criterion that were taken from these elements are shown in Figure 5-24 by the points in the black circle. The importance of these points will become clear when looking at the effect they have on the fit of the failure surface, presented in Figure 5-26. These failure combinations are then used to fit the Hosford-Coulomb failure model, using a least squares fit.

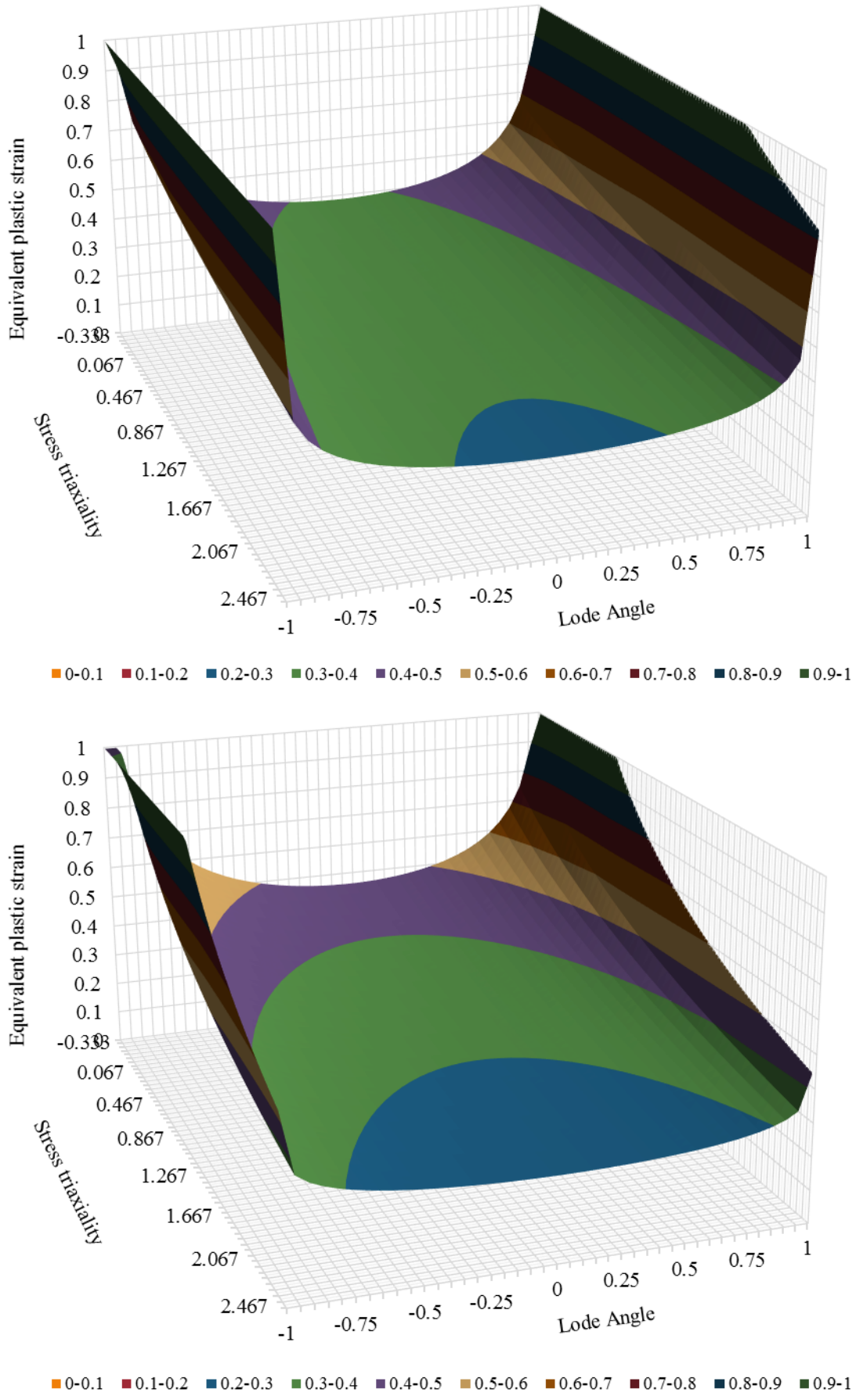

Figure 5-26 Fitted surface with the flanking elements (top), Fitted surface without flanking elements (bottom).

The difference between the two failure surfaces can be summarised by two characteristics. Ignoring the failure criteria from the conflicting elements, results in the bottom surface of Figure 5-26. Including those elements leads to the failure surface presented in the top of Figure 5-26. Including those failure criteria leads to a smaller dependence on stress triaxiality, but a greater dependency on the Lode angle. This is characterised by respectively a less steep decline in failure strain from low triaxialities to high triaxialities and a steeper incline for increasing Lode angles. The models were applied to the mesh to find the differences between them. It was found that there was a negligible difference between the produced force-CMOD curves. The reason for that lies in the effect of those damaged elements on the bearing capacity of the model. During calibration, it was found that when the failure criteria were inserted that caused the damage of the seemingly conflicting elements, no significant loss of bearing capacity was measured. Thus, the same trend was found in the calibration and simulation using the fitted model that includes the failure criteria from the conflicting elements.

The effect of the two different failure surfaces does become clear when looking at the crack path in an advanced stage.

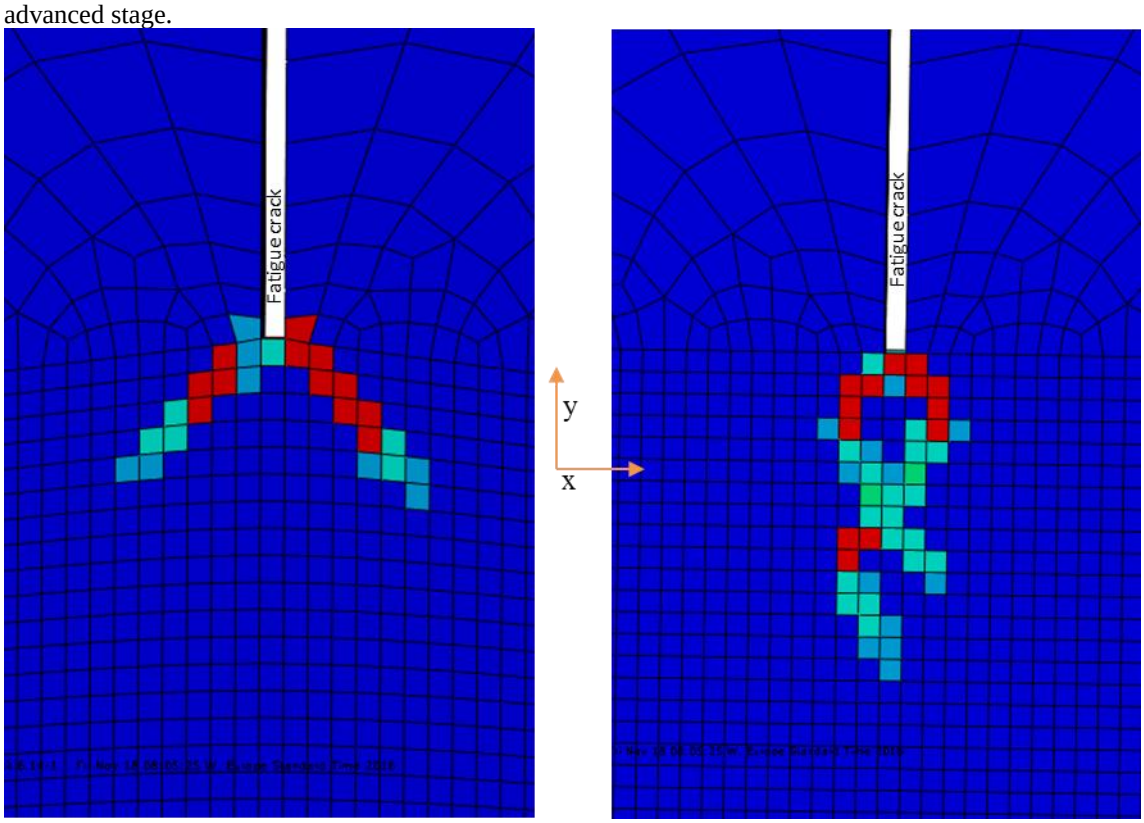

Figure 5-27 Fracture path from HC model with conflicting elements, plotted on an undeformed mesh. All elements with colours different than dark blue are fully damaged. Free surface (left) and thickness symmetry plane z=0 (right).

In Figure 5-27, the fracture paths of the model with the failure combinations from the conflicting elements, are plotted on an undeformed mesh. The crack has grown globally in a downwards fashion on the z=0 plane, which is where indeed growth in the ligament direction is expected. On the free surface, left, an immediate growth to the x-direction can be seen. This agrees well with the expected growth of the shear lips, shown Chapter 5.2.2. The crack growth at z=0 shows a zigzag-like pattern. While in the real specimen the tunnelling crack in ligament direction also shows a zigzag like pattern, the amplitude of the zigzag in the simulation is much bigger. Zigzag patterns have a micromechanical basis and were discussed in chapter 3.2.2. In short, the cause for the zigzag pattern is a combination of the maximum plastic strain and the constraint. The maximum plastic strain can be found at an angle of 45° to the crack plane and this is where the crack grows due to void coalescence. The high constraint however forces the crack back towards the ligament direction, resulting in a zigzag pattern on a microscopic scale. In the FCD model used here the same happens, but the scale is much larger due to the discretisation. All in all, the agreement between experimental results and the simulation is consistent.

Now the same simulation is run, but with the damage model where the criteria resulting from the conflicting elements were ignored.

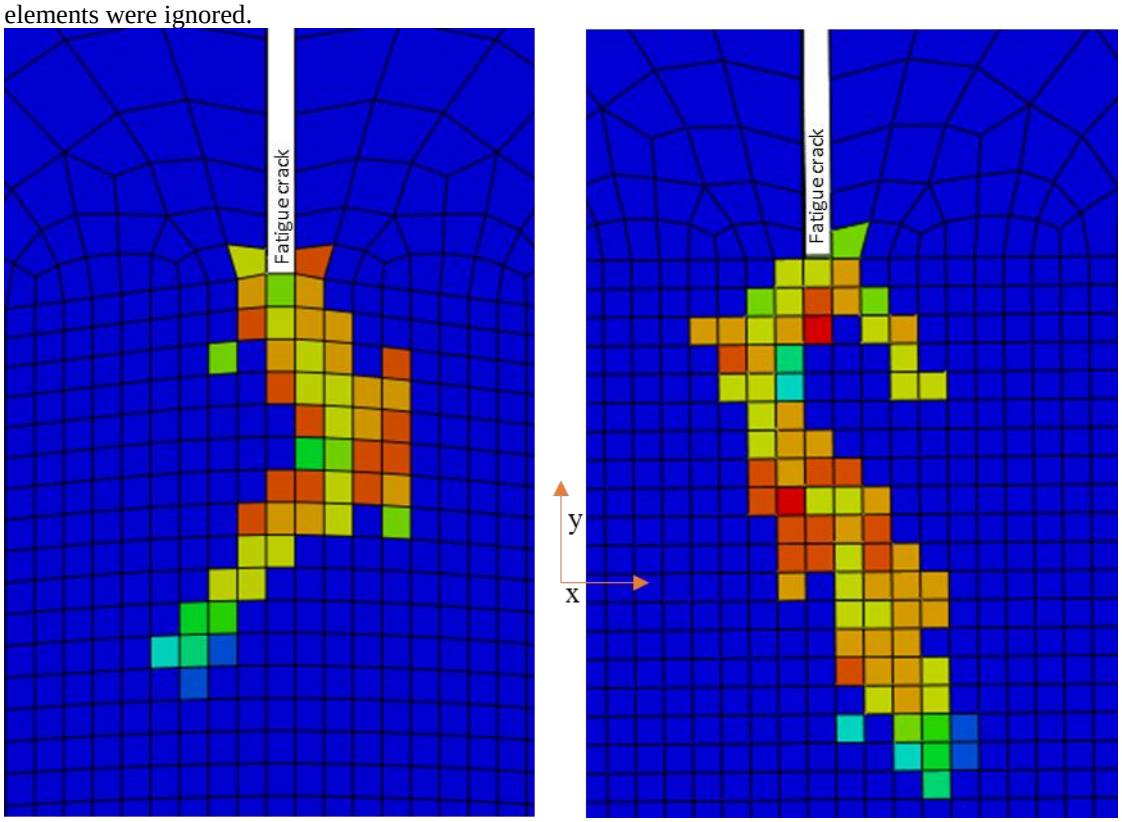

Figure 5-28 Fracture path from HC model without conflicting elements, plotted on an undeformed mesh. All elements with colours different than dark blue are fully damaged. Free surface (left) and thickness symmetry plane z=0 (right).

On the z=0 plane, a crack growing in a downward fashion can be found, while the zigzag pattern is not as visible as in Figure 5-27. The free surface on the other hand, left in Figure 5-28, shows no sign of shear lip formation immediately from the end of the fatigue crack. This immediate shear lip growth from the fatigue pre-crack, characterised by crack growth in x-direction, is seen in all experiments. For this reason, the omission of the conflicting elements in calibrating the Hosford-Coulomb model is not correct. The fitted surface as presented in the top of Figure 5-26 will thus be used in all further simulations.

This calibration procedure has been carried out for the meshes that were also used to investigate the effect of mesh size on the stress states and failure strains, as was presented in Table 5-7. Very similar failure loci were found, with the main difference being the strain at failure, but also tiny differences in the gradients of the surface. The effect of these differences is shown in the next paragraph, were the calibrated failure surfaces are applied to the their respective meshes. For stress triaxialities higher than 0.3, this fitted surface has the characteristics of a maximum shear criterion, but with a strong stress triaxiality dependency. For any stress triaxiality, the failure strains belonging to a zero Lode angle, which signifies pure shear, is the lowest.

5.5 Verification of the damage model

In this chapter, the calibrated failure models are applied to the mesh on which they were calibrated. This is done to investigate the quality of the fit, as well as a possible difference between crack initiation and propagation. A typical force-CMOD graph of the application of the damage model, together with the calibration and the experimental values can be seen in Figure 5-29. From this figure, it is clear that there are some differences between the failure combinations as they are inputted as a locus of points, or as a fitted surface. The most notable point where this can be seen is at the occurrence of the very first damage. In the calibration, the deviation from the experimental values can by design never exceed 1%. The fitted model on the

other hand shows for all examined meshes a value of up to 2.5% higher than the experimental values for the first elements. This can be seen directly from the first drop in force, at a CMOD of around 0.8.

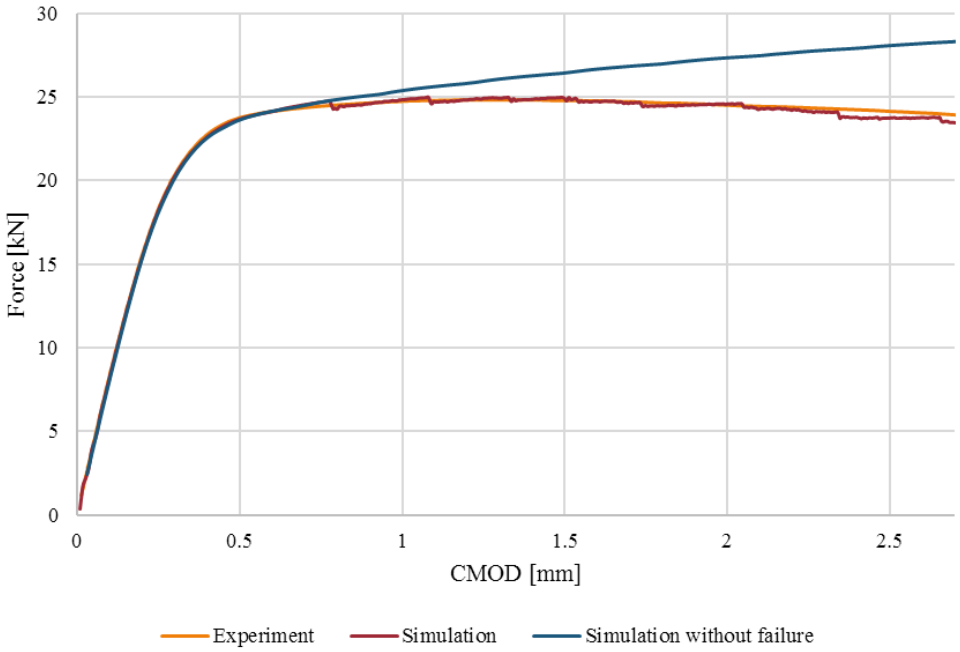

Figure 5-29 Force-CMOD for the application of the damage model on the 0.2mm mesh.

The difference between the three meshes and their calibrated failure models can best be described by the box and whiskers plot shown in Figure 5-30. The data represented in the graph was generated by dividing the strain to failure during calibration by the strain at failure in the fitted Hosford-Coulomb model. From this graph, it can be concluded that the fit using the finest mesh, 0.1mm elements, is of much higher quality than the mesh with 0.3mm elements. For practical reasons, computation time in particular, the model obtained from the calibration with 0.2mm elements is used. While the spread is bigger compared to the 0.1mm model, the extremities are much smaller than for the 0.3 model.

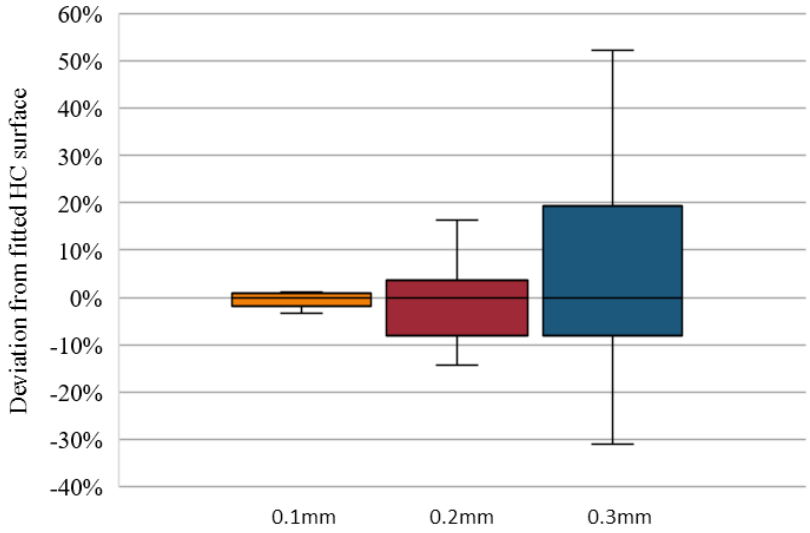

Figure 5-30 Spread in failure strain for points used for calibration and their failing during application with the fitted HC model. The line in the boxes represents the median of the whole set, the upper and lower bound of the box represent the median of the top and bottom half of the set separated by that median. Finally, the whiskers show the maximum deviation that was found.

To comment on the correctness of the damage model, two important requirements must be met, which were introduced in the beginning of the chapter. These requirements are:

1. No or small differences between the force-CMOD measured in the experiment and the simulation.
2. Agreement between the crack path in the experiment and simulation.

The first requirement deals with the correct prediction of the loss of bearing capacity. In Figure 5-29, both the calibration and application of the damage model show a saw tooth-like effect on the force-CMOD curve. These drops in force are caused by multiple elements being damaged shortly after each other, and is a direct effect of the discretisation by finite elements. The overall trend in simulated forces agrees well within ±2.5% of the experimental values and the force maximum is even accurately predicted within 0.5%. This is deemed sufficient and the first requirement is met.

The agreement between the crack path in the experiment and simulation is more difficult to assess. While there is a good agreement between the real crack growth and simulated crack growth on a larger scale, some obvious effects of the discretisation of the specimen by finite elements are seen. This is most apparent in the growth of the shear lip on the free surface, which in reality occurs in a diagonal fashion, at roughly 45° from the fatigue crack. The discretisation with finite elements causes a stair step pattern, but also in 45° angle fashion. The same goes for the zigzag pattern of the crack growing in the ligament direction. This zigzag pattern causes a 45°-degree crack growth of at most 4 elements in both x and y-direction. When a finer mesh is used, this number of elements does not change, but the actual dimension of the simulated crack does become smaller.

All things considered, the fitted damage model predicts the force-CMOD curve far past the point where the calibration was run, and produces deviations no larger than 2.5%. Additionally, the crack path is simulated roughly in the same way the crack grows especially when taking the limitations of the discretisation in mind.

6 APPLICATION OF THE DAMAGE MODEL

In this chapter, the damage model that was found in chapter 5 is applied to a SENB specimen with different cross-sections. The transferability of the failure surface to other geometries is directly related to the second part of the main research question:

Is a stress triaxiality, Lode angle and plastic strain based failure model, calibrated from a single SENB specimen, able to correctly predict failure in differently sized SENB specimen?

This can be split into two parts:

1. Is it possible to calibrate a failure model, where the strain at failure is a function of stress triaxiality and Lode angle, using only a single SENB specimen?
2. Is this failure model able to correctly predict crack growth in SENB specimen with different geometries?

Correct crack growth prediction is defined in the following ways:

1. No or small differences between the force-CMOD measured in the experiment and the simulation.
2. Agreement between the crack path in the experiment and simulation.

This chapter deals with the second part of the research question; Checking whether the damage model calibrated from the smallest specimen can correctly predict crack growth in SENB specimen with different dimensions. In chapter 3, reasons were given why a size effect exists in terms of fracture toughness parameters. These reasons are correlated with the effect of the specimen's dimensions on the stress states in the specimen. Using finite element modelling can shed light on which stress states exist, how they are distributed through the model, and the effect of crack growth on them. Stress states can be accurately described through the stress triaxiality and Lode angle and as such, the effect of geometry that complicates fracture mechanics can be accurately simulated. Consequently, using a continuum damage mechanics approach with a stress triaxiality, Lode angle and equivalent plastic strain based failure model, calibrated on one geometry, should be able to work predictively for other geometries. This is the hypothesis that is tested in this chapter.

The geometries of SENB specimen that were tested are shown in Figure 6-1. The force-CMOD curves for these experiments were shown in Figure 5-4, Figure 5-6 and Figure 5-7.

Figure 6-1 Different geometries with their cross-sectional dimensions. 24x48mm (left), 24x24mm (middle), 12x24mm (right). Calibration of the failure surface is based on the smallest specimen.

6.1 Force-displacement curves

All FEM models are made with the same characteristic element length (0.2mm) in the areas where crack growth is expected. The results of applying the calibrated HC model from chapter 5, are plotted in Figure 6-2 for the 24x24mm specimen and in Figure 6-3 for the 24x48mm specimen.

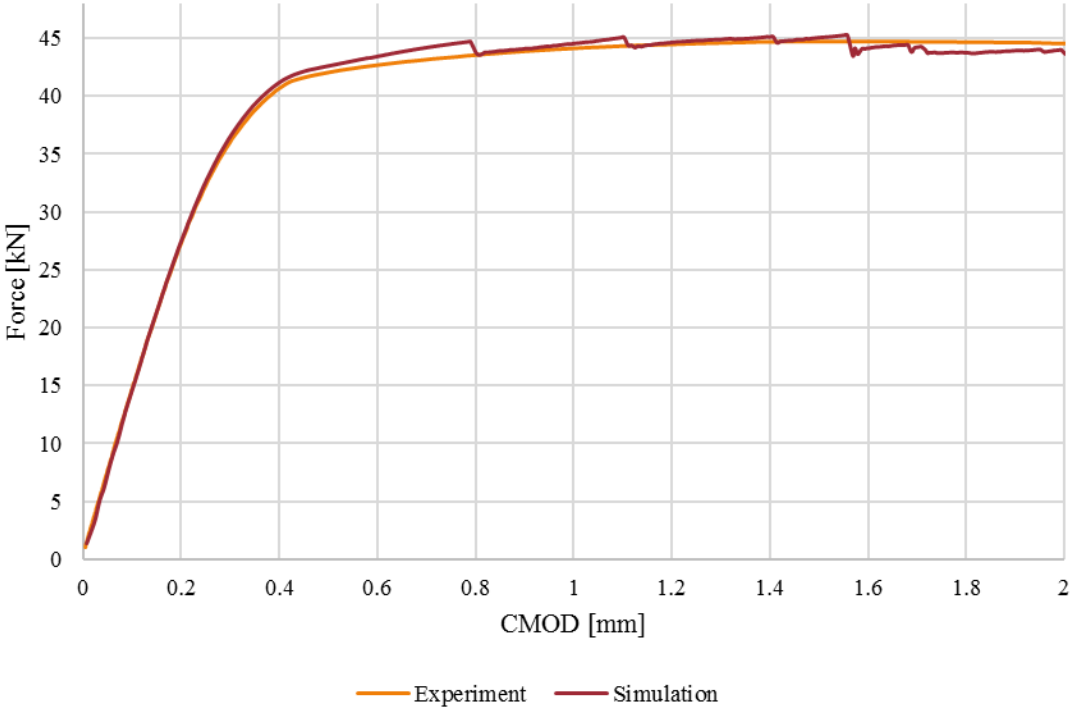

Figure 6-2 Force-CMOD curve for 24x24mm specimen

It is interesting to see that in the Force-CMOD curve for the 24x24mm specimen, is that it has a sharper change in gradient than the 24x48mm and 12x24mm specimen. This sharp turn, for the 24x24mm specimen at a CMOD of 0.4, is attributed to the development of a plastic hinge (Nevalainen & Dodds, 1995). Assuming this is true, which is confirmed by the simulated plastic zone just before failure in Figure 7-2, it is clear that in all specimens failure occurs after the formation of the plastic hinge. The implications of this are discussed in chapter 7.2. That point aside, the calibrated failure model does an acceptable job of predicting failure in the 24x24mm specimen. The maximum deviation from the experiment is found to be 2.5%, while the average deviation is less than 1%. Additionally, the force maximum is found with a deviation of less than 1%.

In the case of the 24x48mm specimen, the simulation is allowed to run longer in order to verify the size of the crack growth on the free surface. Results are therefore presented for a much greater domain of CMOD than the other specimen. These results are presented in Figure 6-3.

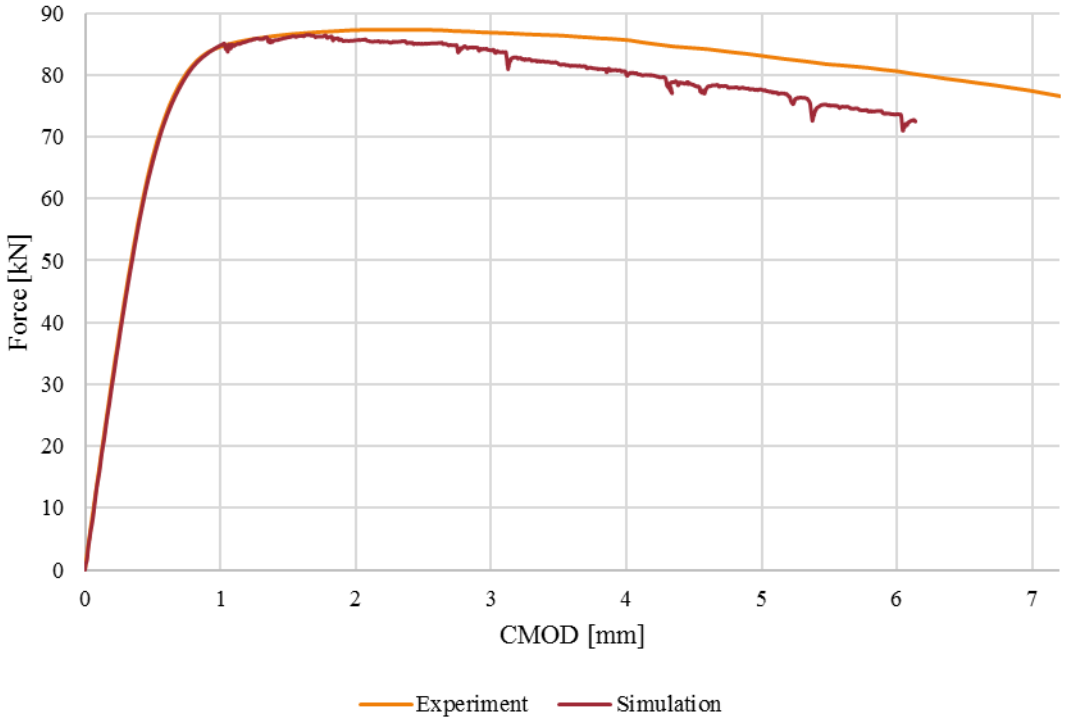

Figure 6-3 Force-CMOD curve for the 24x48mm simulation

Clearly, the calibrated failure model performs less well than for the 12x24mm and 24x24mm specimen. The deviation between first failure, at a CMOD of 1, and a CMOD of 1.7 is acceptable, with an average deviation of 0.5%. Beyond that CMOD, the simulation clearly deviates from the experiment. This also goes for the CMOD where the maximum force is found, which results in an underestimation by 2.5% of the maximum force at a CMOD of 2.1.

To conclude this part of the verification of the damage model, part one of the check of correct crack growth prediction, the following things are to be said.

1. For a limited amount of CMOD increase, the crack growth is simulated with an accuracy of on average 0.5%.
2. Crack initiation is predicted in the 24x48mm before 0.5% deviation can be reached between experiment and simulation. For the 24x24mm specimen, this is 2.5%, and for the 12x24mm specimen, it is 1.1%.
3. For higher CMOD values, the crack growth prediction becomes less accurate in terms of the force-displacement prediction. The deviation increases to almost 10%.

Reasons for the observations listed above are presented in chapter 7, as well as the conclusion (chapter 8) and the discussions in chapter 9.

6.2 Crack path

The last check of correct crack growth prediction is the extent to which the damage model is able to simulate the crack path. A correct prediction of the shape and size of the crack path helps to defend the application of the calibrated HC-model. For this purpose, the simulation of the 24x48mm specimen was extended to the end of the experimental procedure, at a CMOD of about 7mm. Then, the roller motion was reversed, resulting in elastic relaxation. The reason that this particular specimen was chosen, is simply because this is the only specimen for which a photo of the specimen was made, directly after it was taken out of the setup as presented in Figure 5-1. The resulting deformed mesh, with all damaged (D>1 as defined in section 5.2.4) elements removed from view, is overlaid on the experiment in Figure 6-4. In this figure, one can see various differences between the simulated crack path and the experiment. First, the width of the crack path is greater in the simulation than in the experiment. One of the reasons for this is that the in the simulation the crack is visualised by removed elements.

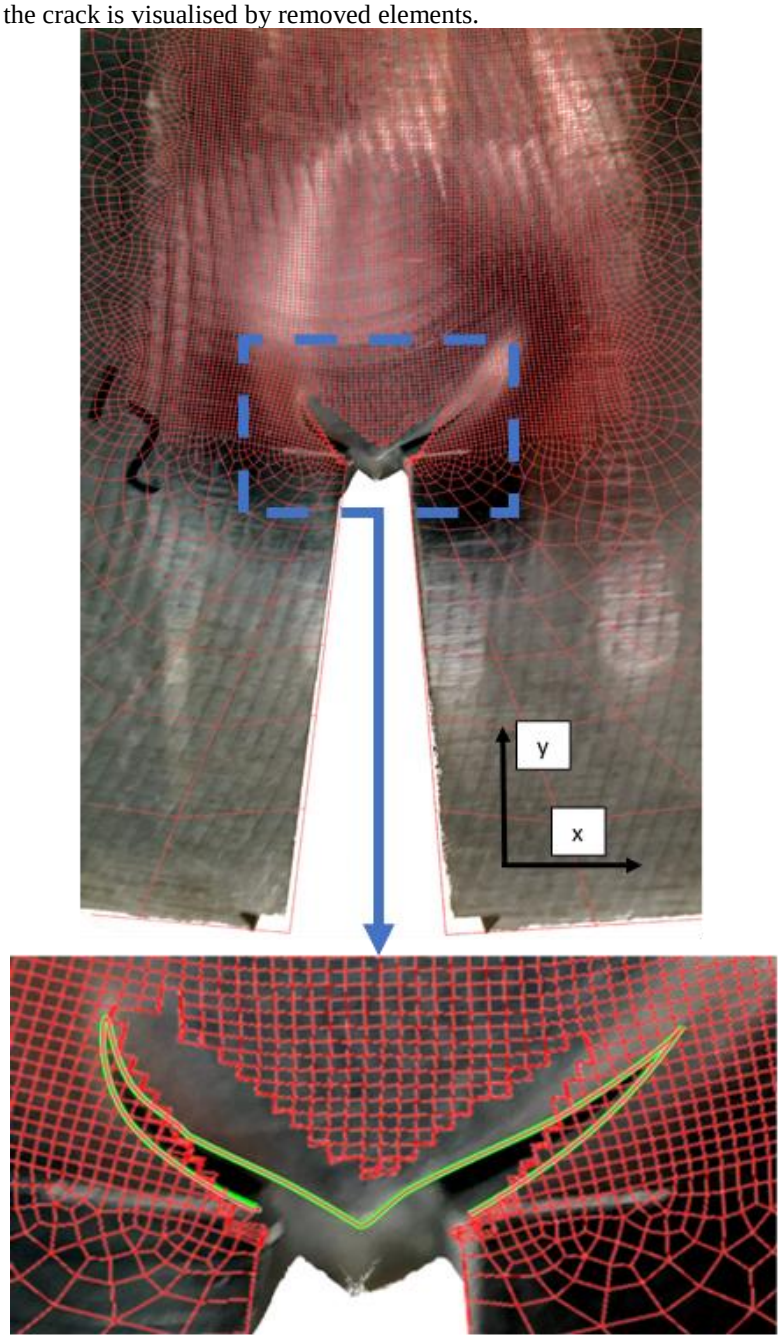

Figure 6-4 Crack path in deformed mesh overlaid on experiment at the free surface. Crack in experiment is highlighted in green.

The simulated crack path consists of multiple fully damaged elements through its width, so when they are removed, the crack is at least the combined width of the number of removed elements and the plastic deformation. This explains the difference in crack path width. The slope of the crack path in the experiment has a greater x-component than in the simulation. In the simulation, the slope of the crack path is approximately 45° and becomes greater towards the end. The crack path in the experiment starts with a slope smaller than 45° but ends, especially on the left, with a steeper slope. The extent of the crack is fairly accurately modelled in the y-direction, but less so in the x-direction. It is interesting to note that the crack seems to stop growing symmetrically on the free surface, which is a feature that was found in the experiment as well. Minor differences have started to appear due to the order in which elements are damaged, and these differences propagate in the form of unsymmetrical crack growth.

In the calibration chapter, it was observed that the crack in the symmetry plane grows along the ligament in a zigzag shaped pattern. This same observation is made in both the 24x24mm model and the 24x48mm model. Since the 24x48mm model was simulated to a greater CMOD, this model is best to view the development of this crack growth.

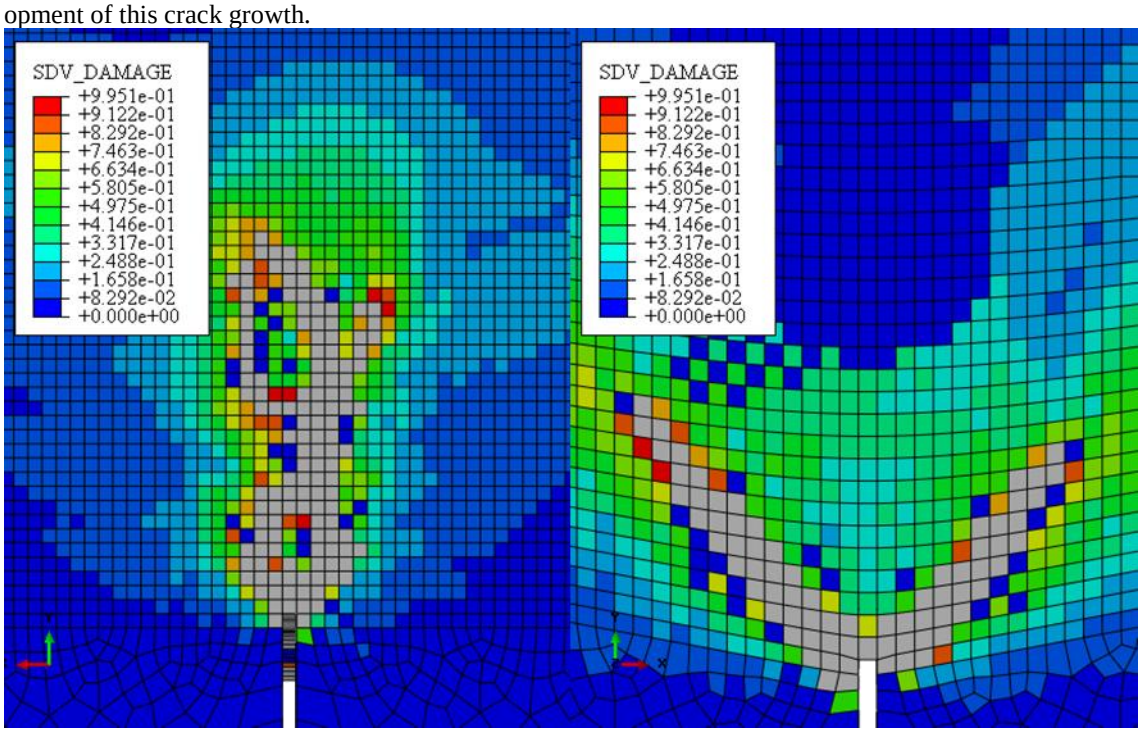

Figure 6-5 Damaged elements on an undeformed mesh, presented on the symmetry plane (left) and the free surface (right).

The differences between the simulated crack path and the crack path observed in experiments can also be used to explain the difference in the force-CMOD curves. Due to the great number of damaged elements, especially in the section where tunnelling is expected, more stiffness is lost by this crack discretisation than in reality.

7 OBSERVATIONS ON THE SIZE EFFECT

In this chapter, the effects of the specimen size on the stress states are presented. The stress states are compared just before failure and observations are noted and where possible related to theory. It is important to note that the CTODs of the states presented are smaller than the critical CTOD of each specimen. Consequently, the observed differences in stress states and geometry effects may be true for small CTOD values, but false for CTOD values larger than the critical CTOD. Since failure occurs a little before the critical CTOD is reached in this thesis, cases for large CTODs are not researched.

7.1 Stress states before failure

In chapter 3, it was explained that the size of the specimen effects the constraint in the specimen. The stress states are first examined in the xy-plane, and later in the yz-plane. Accordingly, one would expect to find differences in the distribution of the Lode angle and stress triaxiality between the specimen. This is most visible at the symmetry plane in thickness direction, because this is where the biggest differences in constraint are expected. In Figure 7-1, the Lode angle contour plots of the 12x24mm specimen and the 24x24mm specimen are shown. For the 24x24mm specimen, one can distinguish a ring with a diameter equal to the ligament of Lode angles close to zero. A Lode angle of zero indicates plane strain dominance. While the 24x48mm and 12x24mm specimens also show a concentration of plane strain condition near the crack-tip on the symmetry plane, there is no ring shape pattern of values close to zero to discern.

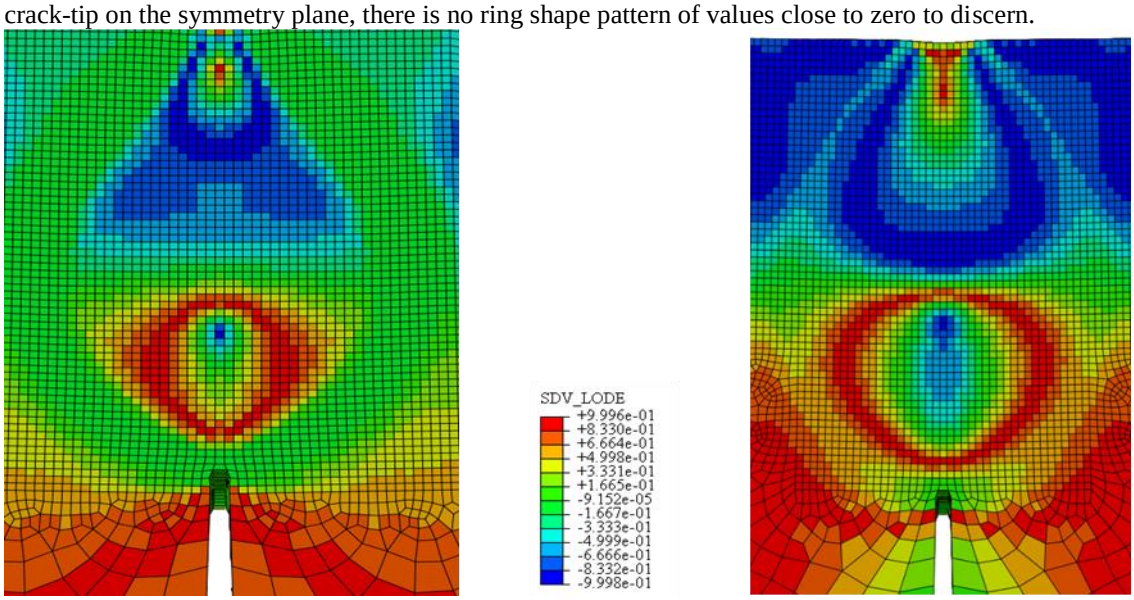

Figure 7-1 Lode angles on the thickness symmetry plane (xy-plane). 24x24mm specimen (left), 12x24mm (right). See appendix C for the interactive 3D plots.

The actively yielding elements just before first failure are shown in Figure 7-2. How the actively yielding elements are different from the plastic deformed elements, as well as the stages of plastic hinge development, are explained in chapter 7.3.

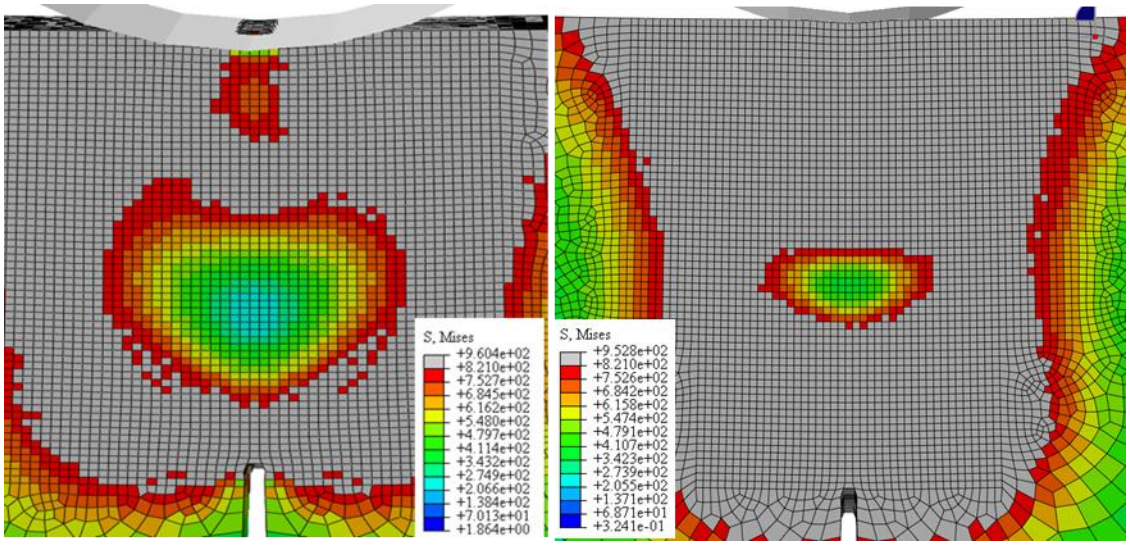

Figure 7-2 Currently yielding elements (grey) just before first failure on the symmetry plane. Stresses in MPa. 24x24mm specimen (left), 12x24mm (right). See appendix C for the interactive 3D plots. There are no significant differences between the 12x24mm and 24x48mm plastic zone shape.

The 24x24mm specimen shows a significantly smaller low stress region in the centre than the 12x24mm specimen. In both specimen, the magnitudes of the stresses that are displayed in this centre discs show a very strong gradient. Since the disc contains more elements in the 12x24mm specimen than in the 24x24mm specimen, the magnitudes of those stresses are likely influenced by the mesh size relative to the gradient and cannot be compared. In terms of stress triaxiality, the 24x48mm and 12x24mm specimen behave very much alike, with no significant differences in the shapes of stress triaxiality. The differences in magnitude between of stress triaxiality, Lode angle and equivalent plastic strain is discussed later on.

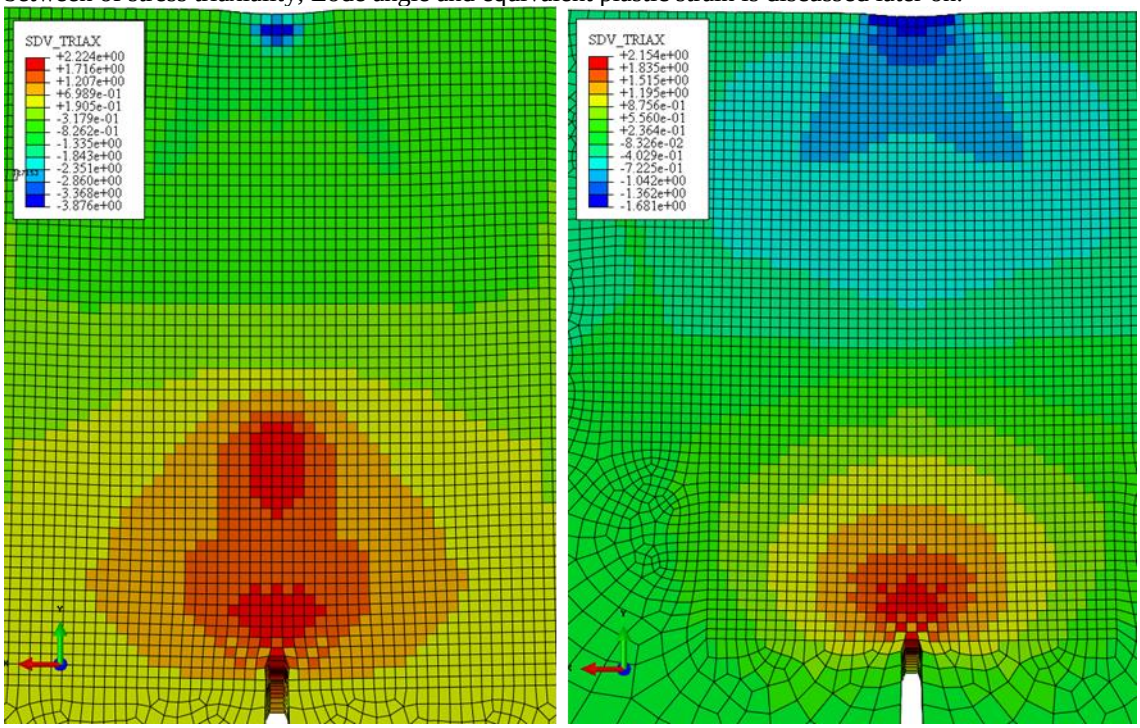

Figure 7-3 Stress triaxiality just before first failure. 24x24mm specimen (left) and 12x24mm specimen (right). See Appendix C for the interactive 3D plots.

From the two contour plots in Figure 7-3, one major difference stands out. This is the existence of a second concentration of high stress triaxialities at some distance from the crack tip. To study this occurrence better, the attention is switched to the yz-plane. According to Figure 7-4, earlier shown in chapter 3, the expected maximum of the stress triaxiality can be found at a distance of 2 times the CTOD.

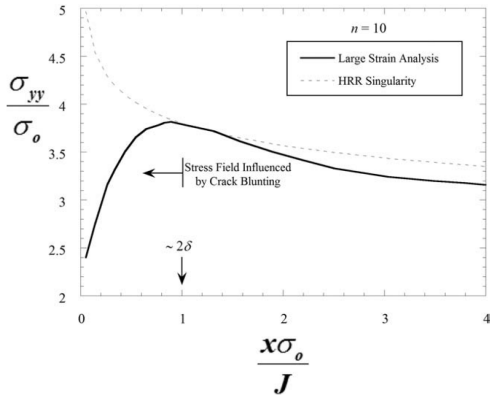

Figure 7-4 Large strain analysis of the stress field near the crack tip using FEM compared with the HRR field. (McMeeking & Parks, 1979)

In the 12x24mm specimen, the critical CTOD was found to be about 0.4mm (Element materials technology, 2016), making the expected maximum of stress triaxiality to occur at about 0.8mm from the crack-tip. Indeed, in Figure 7-5, the peek stress triaxiality is found at a distance of about 0.8mm.

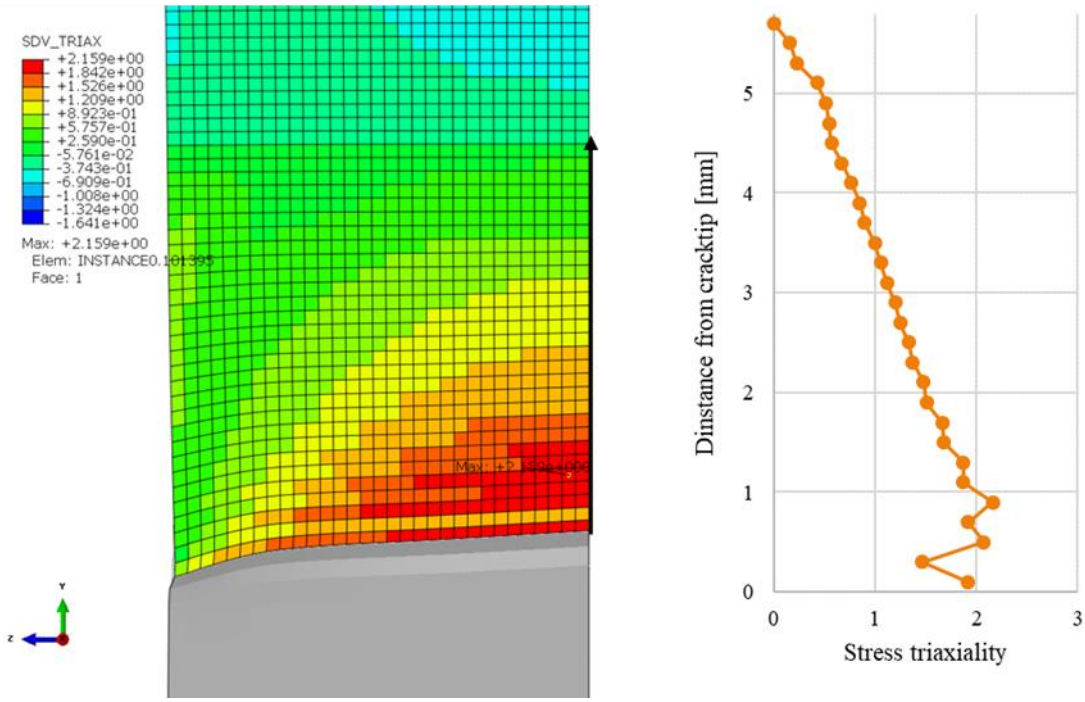

Figure 7-5 Contour plot of stress triaxiality in the 12x24mm specimen just before first failure. Stress triaxiality as function of coordinate along y-axis along black arrow in contour plot (right).

In the 24x24mm specimen, a critical CTOD of 0.41mm was reported. While there is a peak in stress triaxiality around a distance of 0.8mm from the crack tip, a greater peak is found at a distance of approximately 10 times the CTOD. Interestingly, a strong decrease in triaxiality follows to reduce the triaxiality to zero at approximately the same distance from the crack tip as was seen in the 12x24mm specimen. In both cases, the triaxiality became smaller than zero for both specimen, indicating that the boundary between the compression zone and the tension zone in the specimens is at approximately the same location.

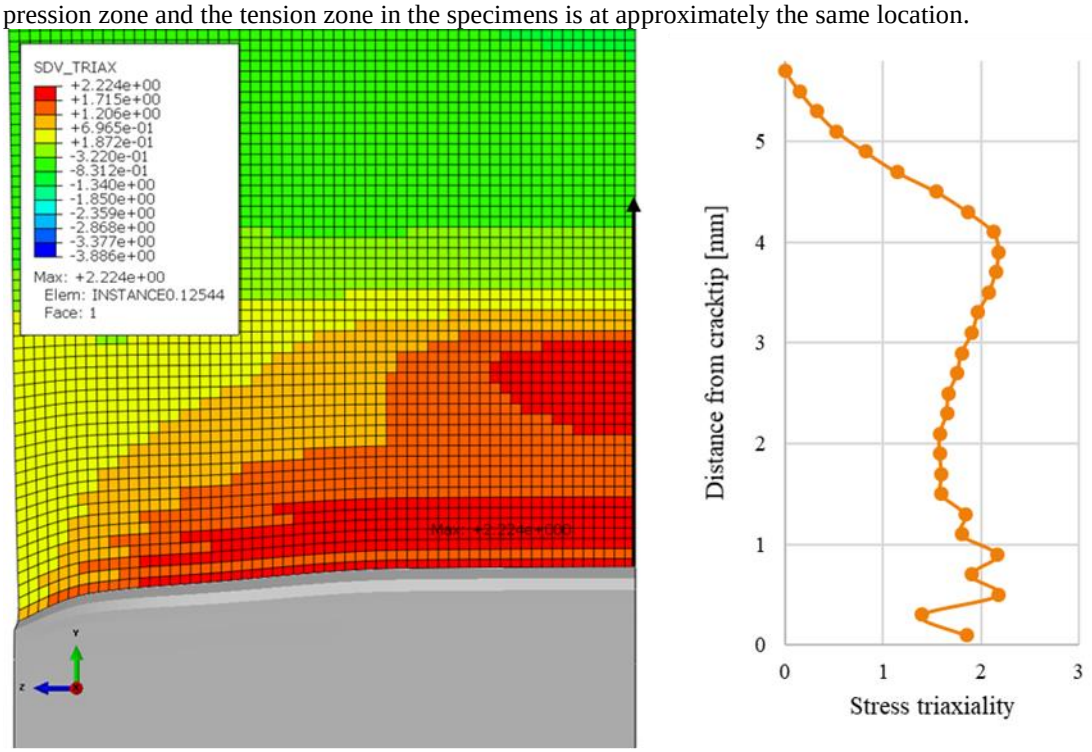

Figure 7-6 Contour plot of stress triaxiality in the 24x24mm (24x24mm) specimen just before first failure (left). Stress triaxiality as function of coordinate along y-axis along black arrow in contour plot (right).

The effect of the specimen size, specifically the width, has an influence on the location where the crack starts growing. The stress states along the z-axis, on the yz-planes that were shown in the previous section, are first shown to indicate the effect of the specimen width on the stress states. Since the crack growth is both in ligament direction, at the thickness symmetry plane, and in the flank direction, where the shear lips emerge, the convention shown in Figure 7-7 is reused from chapter 5.

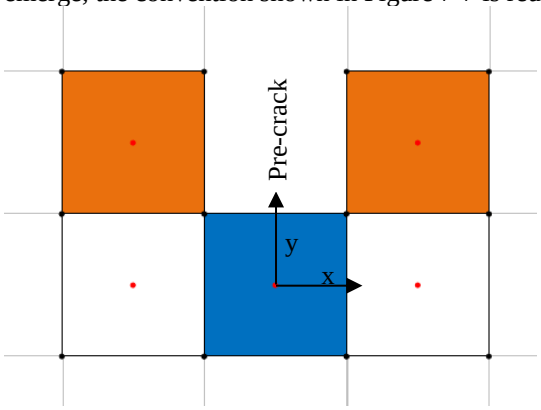

Figure 7-7 Definition of elements in y-direction/ligament (blue) and elements in x-direction/flank (orange).

In the following figures, the stress states of the crack tip elements along the z-axis are presented left and the stress states of the crack flank elements are presented right for the various specimen.
For the case of the stress triaxiality, presented in Figure 7-8, few major differences are found.

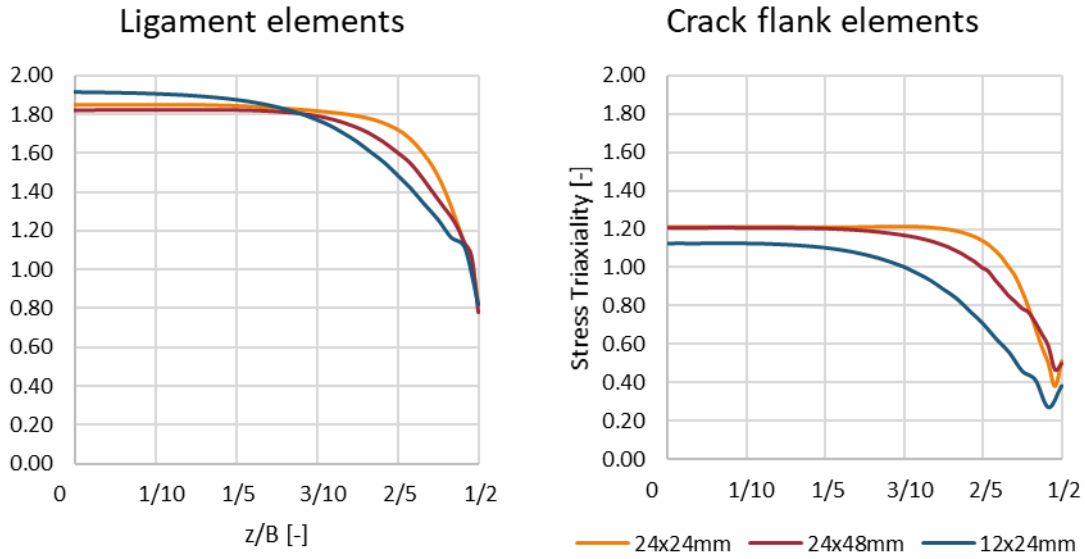

Figure 7-8 Stress triaxiality along the z-axis of the crack-tip for the various specimen, just before first failure. The symmetry plane in thickness direction is at z=0, the free surface at z/B=1/2.

These differences can be summarised as follows for both the elements on the crack flank and the elements on the crack front:

1. Greater thickness equals higher stress triaxiality for the plane strain location.
2. Greater thickness keeps the stress triaxiality higher for relatively further along the z-axis.
3. The ratio of thickness versus ligament also contributes to effect number 2.

In Figure 7-8, it can be seen that the stress triaxiality is constant over a fairly large portion of the thickness. The development of the stress triaxialities versus the absolute distances from the free surfaces, presented in Figure 7-9, is used to investigate this further. Looking at the elements in ligament direction along the z-axis, the curves of the 12x24mm and 24x48mm specimen are remarkably similar for the first 2mm from the free surface.

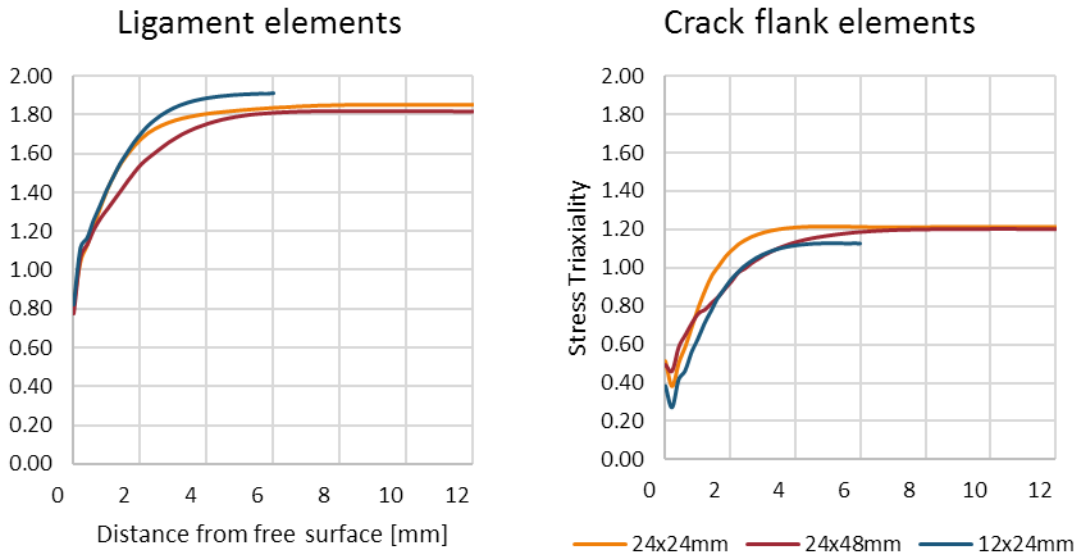

Figure 7-9 Stress triaxiality versus the absolute distance from the free surface to the symmetry plane in thickness direction.

Furthermore, the stress triaxialities seem to be constant for all specimens from about 5mm onwards. This suggests that a certain amount of material, independent of specimen size, is required to bring the stress triaxiality to a constant value from the disturbance created by the free surface. The rate with which the stress triaxiality converges seems to be related to the ratio of the ligament size and thickness, since the 12x24mm and 24x48mm specimens converges faster than the 24x24mm specimen. Whether this amount of material depends on the type of material, falls outside the scope of this thesis.

Secondly, the development of the Lode angle along the z-axis are presented in Figure 7-10.

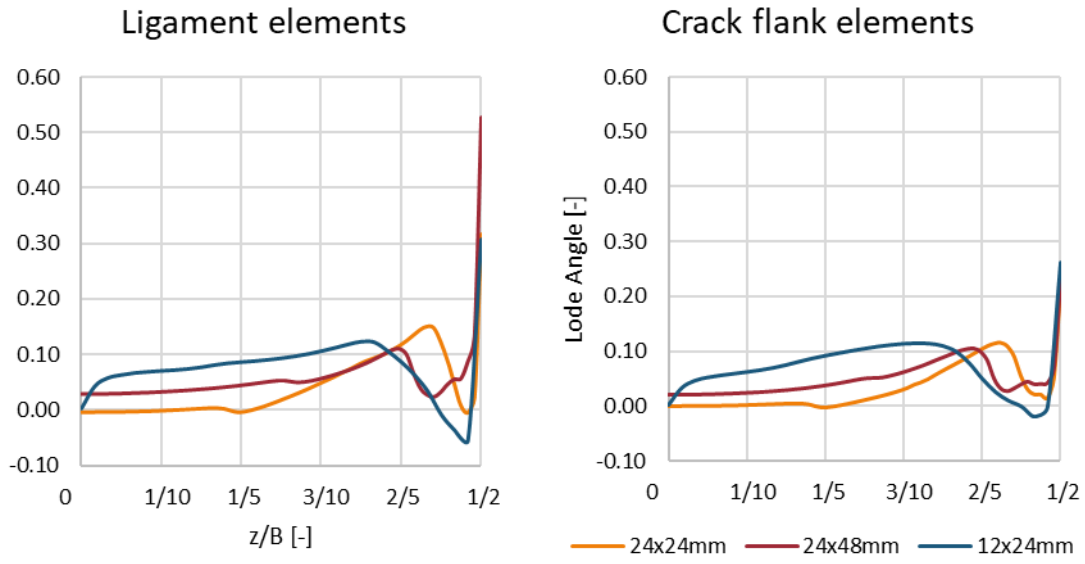

Figure 7-10 Lode angles along the z-axis of the crack-tip for the various specimen, just before first failure. The symmetry plane in thickness direction is at z=0, the free surface at z/B=1/2.

The Lode angle along the z-axis is very similar for all specimen, with the only major difference being the relative location of the first peak along the z-axis.

In Figure 7-11, the equivalent plastic strain is shown. There are two distinct effects of specimen size here starting with the thickness, using the plot on the crack front. The highest equivalent plastic strain can be found at approximately the same relative distance a small distance (<1/20) from the thickness symmetry plane for the 24x48mm and 12x24mm specimen. In the 24x24mm specimen on the other hand, there is a clear peak of plastic strain at about 3/10 along the way from the symmetry plane to the free surface. Secondly, turning our attention to the elements in x-direction, one can immediately see that the specimen with the largest ligament, has the largest strain in the crack flanks. The ligament size seems to make a greater difference than the width for small z/B, but soon after that, the plastic strain in the 24x24mm specimen catches up with the stress state of the 24x48mm specimen.

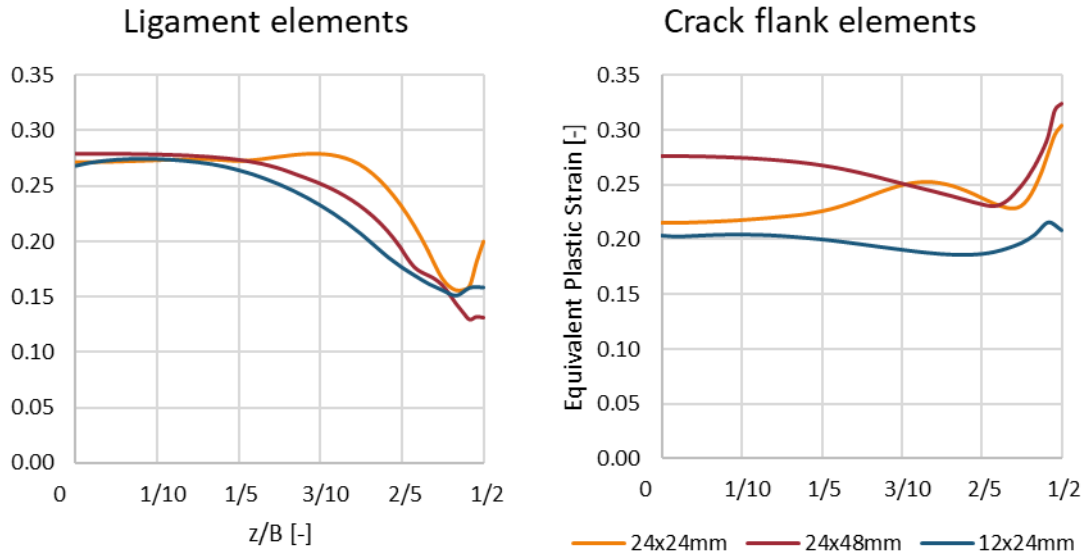

Figure 7-11 Equivalent plastic strain along the z-axis of the crack-tip for the various specimen, just before first failure. The symmetry plane in thickness direction is at z=0, the free surface at z=1/2.

From Figure 7-11 the main effects of the specimen size can be summarised as follows for elements on the crack front:

1. Both the thickness and ligament size have very little effect on the plastic strain experienced at the symmetry boundary condition.
2. Similarly to what was seen for the elements on the crack flank, the strain for the 24x24mm specimen only goes up from z/B=0 till z/B=3/10.
3. The ratio of thickness to ligament has the greatest effect on the plastic strain on the free surface, where plane stress prevails.

Similarly, the main effects of the specimen size can be summarised as follows for elements on the crack flank:

1. The thickness of the specimen seems to drive the equivalent plastic strain at the specimen's free surface, where plane stress prevails.
2. The ligament has the largest effect near the symmetry surface, where plane strain prevails.
3. Where the 24x48mm and 12x24mm specimen experience a decrease in strain from z=0 onwards, the 24x24mm specimen increases until z/B=3/10.

7.2 Stress states after first failure

When elements start failing, this influences the stress states near the crack tip quite a lot. An example of this influence is shown in Figure 7-12.

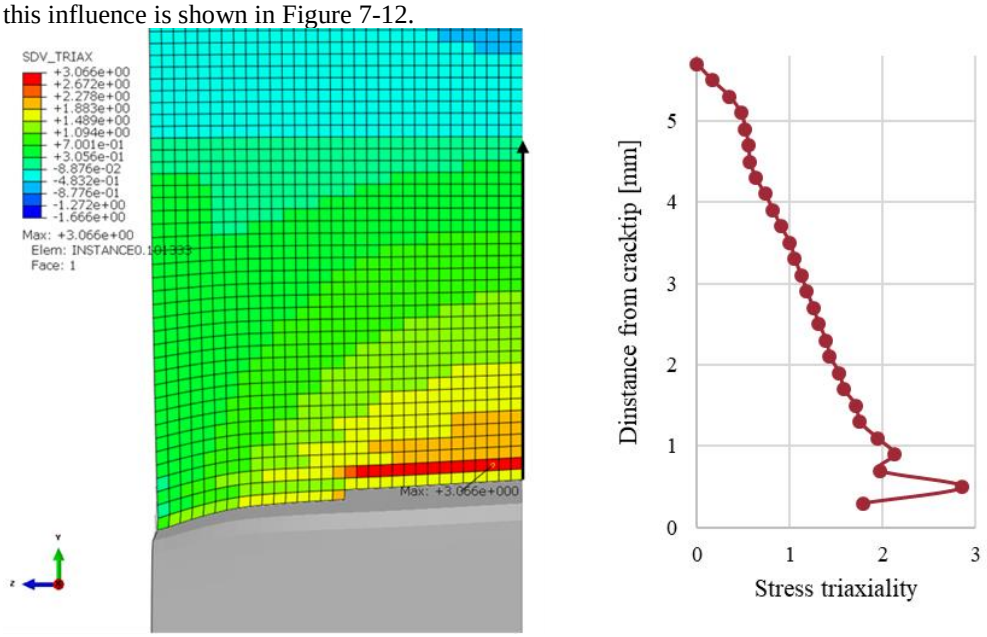

Figure 7-12 (Left) Contour plot of stress triaxiality in the 12x24mm specimen immediately after the first set of elements has failed (removed from view). (Right) Stress triaxiality as function of coordinate along y-axis along black arrow in contour plot.

In the graph presented in Figure 7-12, the classic shape of stress triaxiality over distance from (McMeeking & Parks, 1979) is found. However, the distance of the peek from the new crack-tip is only 0.3mm, which is equal to the distance from the edge of the first undamaged element to the integration point of the second undamaged element in y-direction. Similar behaviour is spotted in the 24x24mm specimen, immediately after a first set of elements are damaged. Interesting to note is that the stress triaxiality is much higher than in the 12x24mm simulation. However, this may just as well be an effect of the mesh size, considering the steep gradients in the triaxiality are captured by just 2 elements.

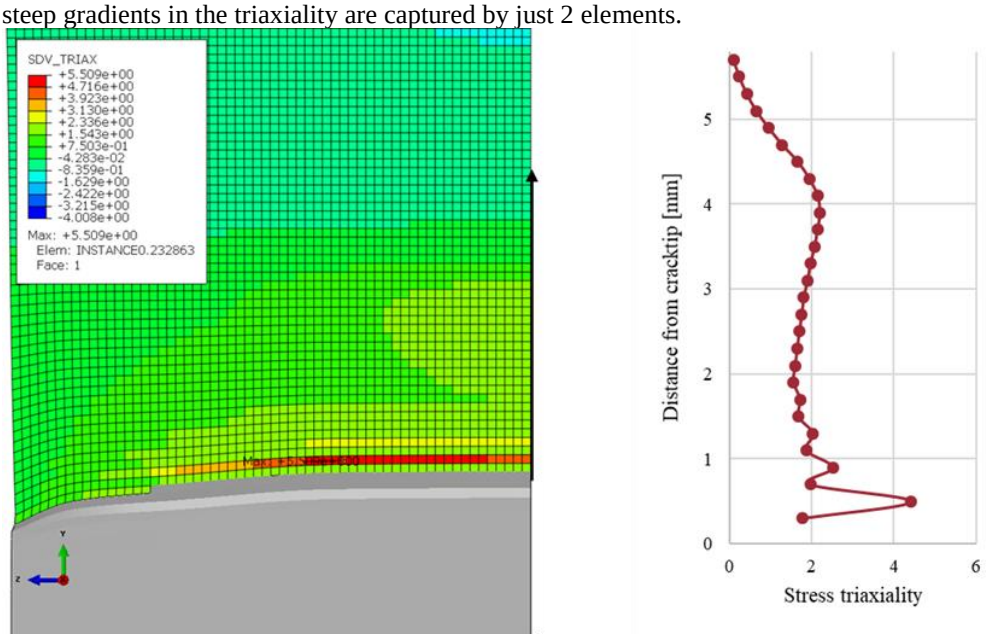

Figure 7-13 (Left) Contour plot of stress triaxiality in the 24x24mm specimen after the first set of elements has failed (removed from view). (Right) Stress triaxiality as function of coordinate along y-axis along black arrow in contour plot.

In reality, the crack does not progress stepwise with steps of 0.2mm, or the characteristic element length, but rather in a more continuous way. In the damage model, the elements response to strains in the damaged direction gradually decreases as the plastic strain grows, to approximately simulates that. Due to more plastic straining, the fictitious crack widens over time. Assuming that this is a realistic way of modelling and that the widening of the artificial crack can be seen as a growing crack tip, no further crack growth in the ligament direction can be expected until the critical CTOD is reached again. Thus, one would expect the peak to shift to a distance of twice the critical CTOD before more elements in y-direction are damaged. This process can best be described by looking at a sequence of stress triaxiality states, presented in Figure 7-14. In this figure, the stress triaxiality of the 24x48mm specimen is plotted as the crack grows. For this specimen, the critical CTOD was reported to be 0.53mm, leaving one to expect the highest stress triaxiality to be at 1mm at the critical point, which is the distance of approximately 5 elements from the crack-tip.

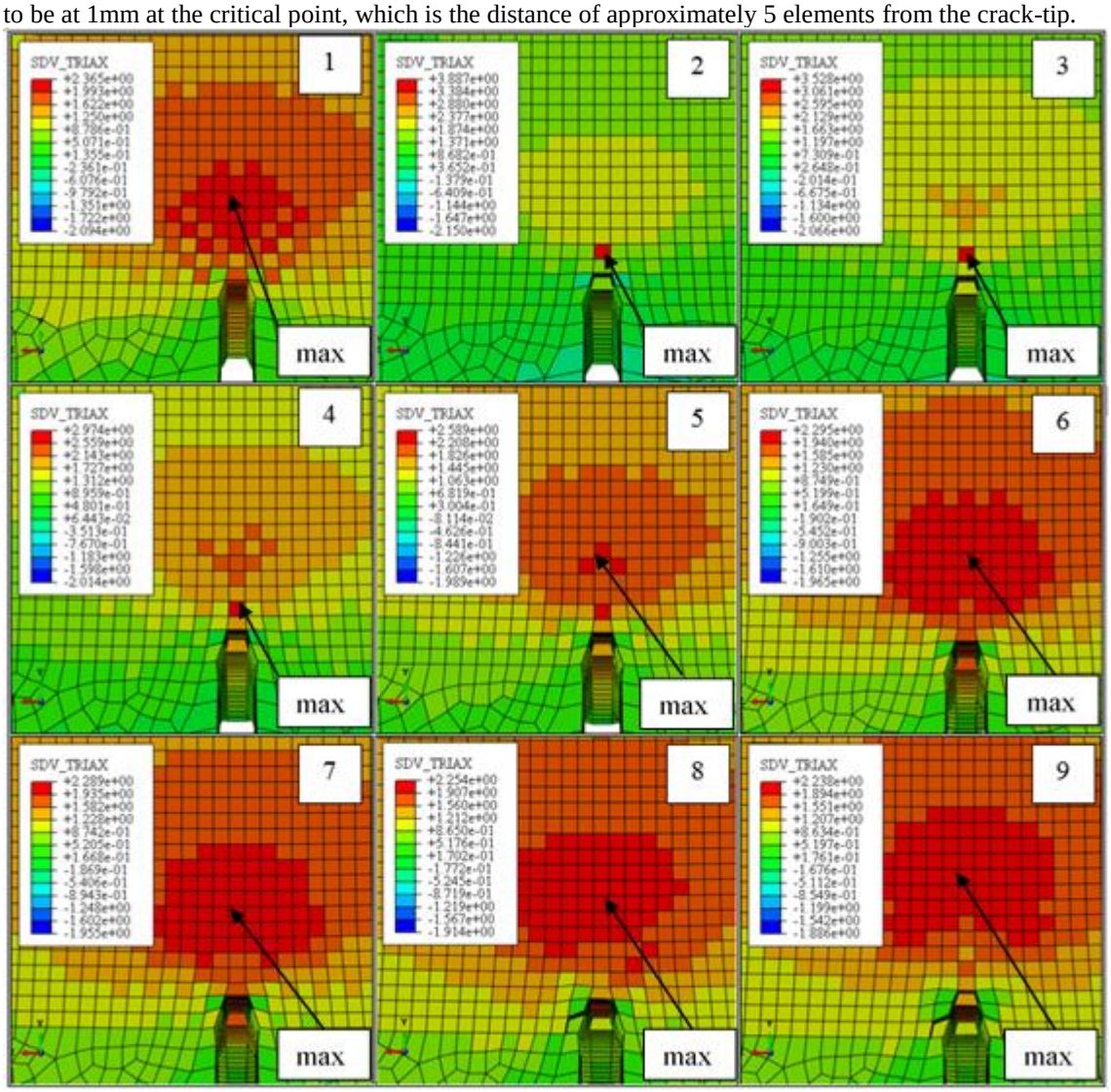

Figure 7-14 Sequence of stress triaxiality growth as the crack progresses by damaging elements (damaged elements are hidden from view for clarity). This is taken from the 24x48mm simulation.

In the first frame, the moment just before damage is captured. The maximum stress triaxiality lies in the 5th element from the crack-tip, which translates to 1mm from the crack tip. This situation is shown in Figure 7-15. Then, in frame 2, a damage criterion is reached and a few elements in z-direction are damaged. This situation is shown in Figure 7-16. The maximum stress triaxiality is now captured by the second element from the new crack-tip. Since this peak is only captured by a single integration point, its magnitude is not very valuable. In stages 3 through 7, the stress triaxiality decreases in magnitude and its location moves upwards in ligament direction. In stage 8, a damage criterion is reached by one of the flanking elements, somewhat distorting the shape of the high triaxiality zone. In frame 9, a new element in ligament (y) direction is damaged.

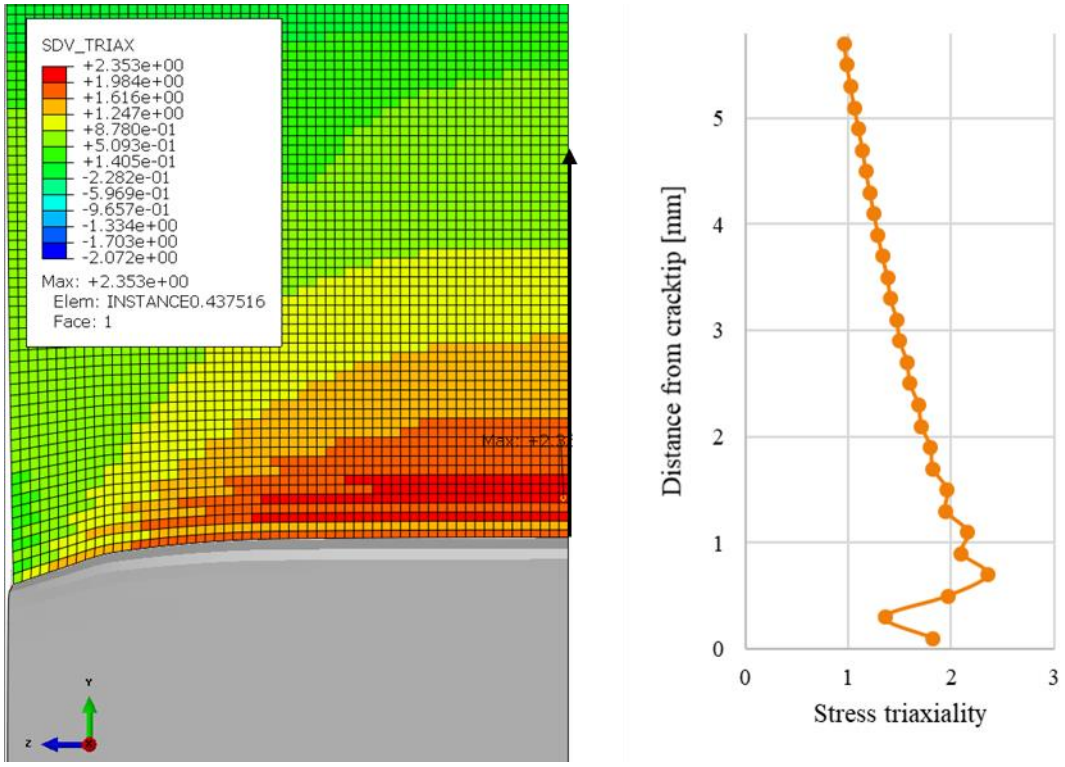

Figure 7-15 (Left) Contour plot of stress triaxiality in the 24x48mm (24x48mm) specimen just before first failure. (Right) Stress triaxiality as function of coordinate along y-axis along black arrow in contour plot.

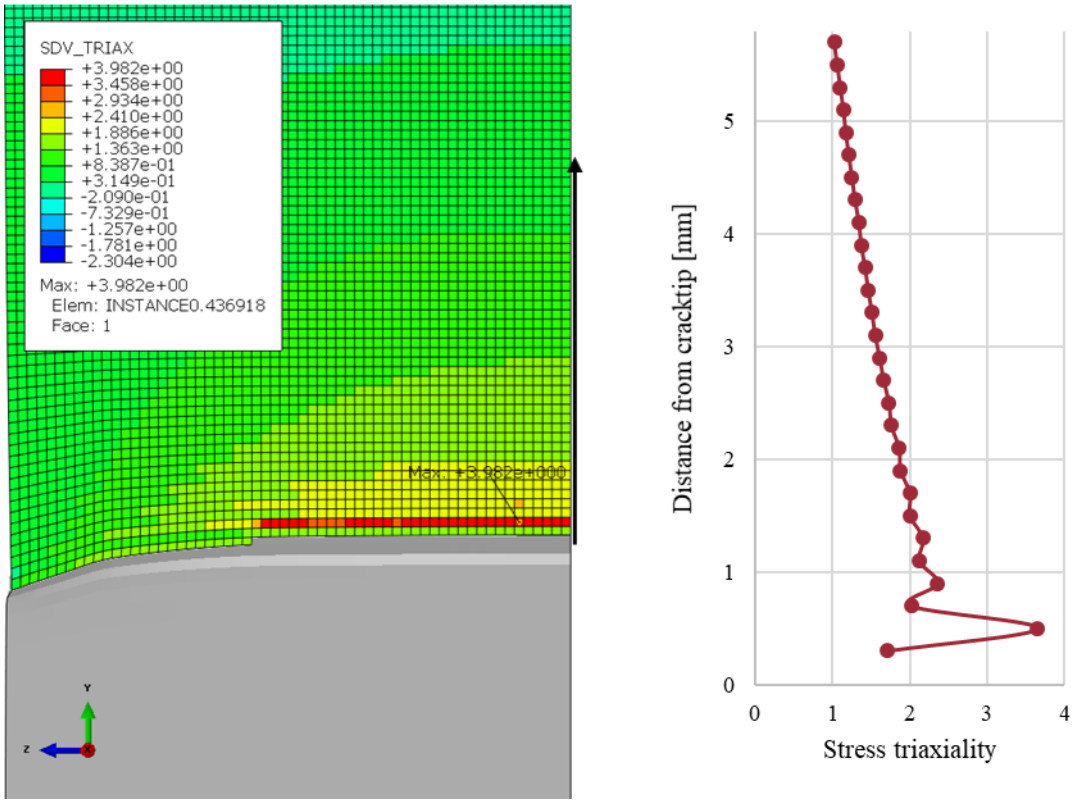

Figure 7-16 (Left) Contour plot of stress triaxiality in the 24x48mm (24x48mm) specimen after the first set of elements has failed (removed from view). (Right) Stress triaxiality as function of coordinate along y-axis along black arrow in contour plot.

These differences in stress state and equivalent plastic strain along the z-axis influence the start of the crack growth. The very first (couple of) elements that are damaged are presented in Figure 7-17 and Figure 7-18. The very first observation is that the first elements that fail are where the peak in equivalent plastic strain occurs.

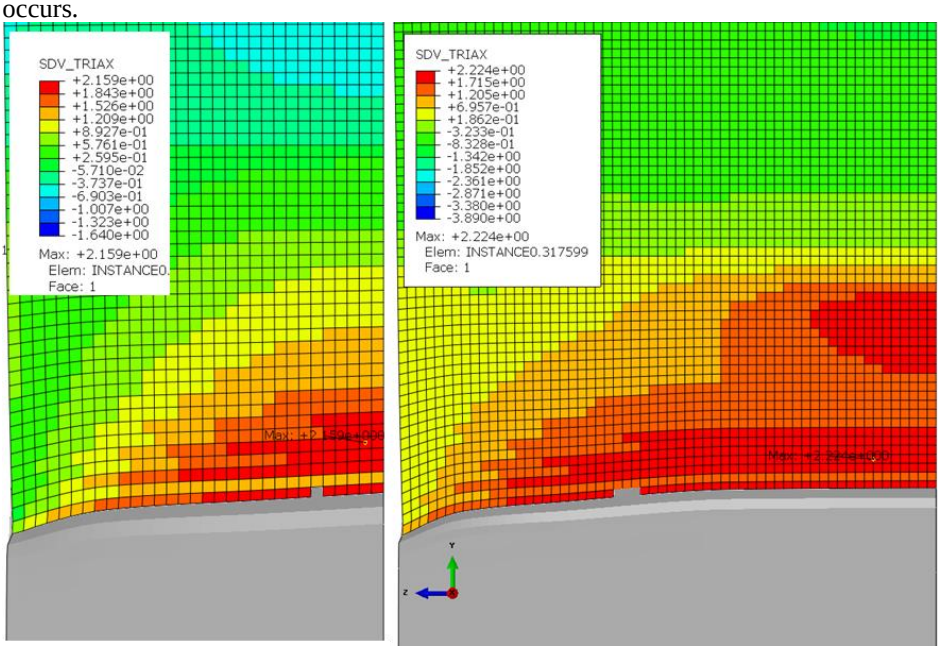

Figure 7-17 First elements to fail, with contour plot of the stress triaxiality. The left boundary is the free surface in the models, the right boundary the symmetry plane. 12x24mm (left), 24x24mm (right).

Even in the 12x24mm specimen, where during the calibration the crack was forced to grow from element at the symmetry plane in thickness, the crack does not start in at the symmetry plane, due to slightly higher strains at a small distance from that plane. The elements to the right of the failed element fail very quickly, within a 0.001mm in CMOD increase (or a few time increments), after that first one. In the 24x48mm specimen, it is impossible to tell which element fails first, as a set of 8 elements ranging from the symmetry surface are damaged all at once. This does seem to justify the assumption, used in the calibration, that failure starts from the centre of the specimen in the 24x48mm and 12x24mm specimen. If, on the other hand, one were to calibrate a damage model using a 24x24mm sized specimen, this assumption can clearly not be used.

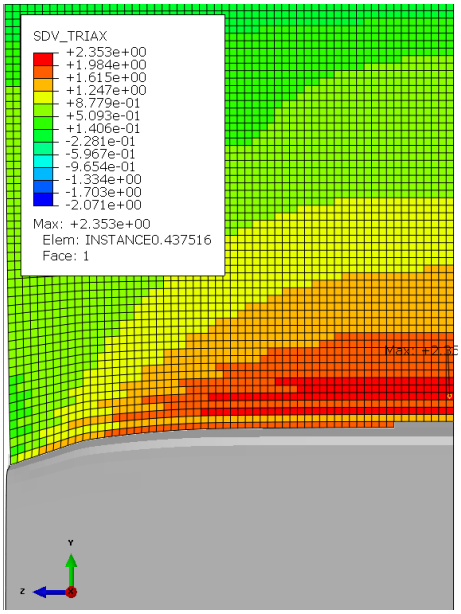

Figure 7-18 First elements to fail of the 24x48mm specimen, with a contour plot of the stress triaxiality. The left boundary is the free surface in the models, the right boundary the symmetry plane.

7.3 Plastic hinge effects

The growth of cracks causes some relaxation in the elements in the plastic hinge zone. For this development, a distinction is made between plastically deformed elements and elements that are actively yielding. This is necessary to describe what happens in the specimen due to crack growth in the plastic hinge. Consider the plastic zone state of the 24x24mm and the 12x24mm specimen displayed in Figure 7-19. The elements that are actively yielding are at this time exactly the same elements that experience plastic deformation. In other words, there are no elements that have yielded in the past load history that are not actively yielding at this step.

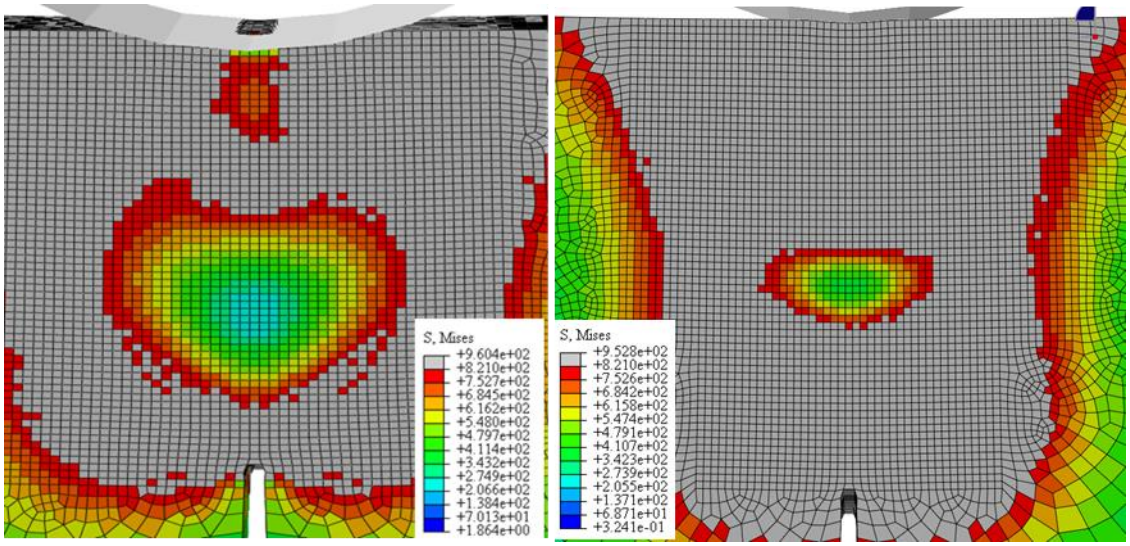

Figure 7-19 Actively yielding elements (grey) before crack formation. 24x24mm specimen (Left), 12x24mm specimen (right).

As soon as the crack starts growing, i.e. elements start to get damaged, some elastic relaxation occurs. This is most prominent in the 24x48mm and 12x24mm specimen, which show identical behaviour in terms of the shape. In the case of the 24x24mm specimen, different behaviour is observed.

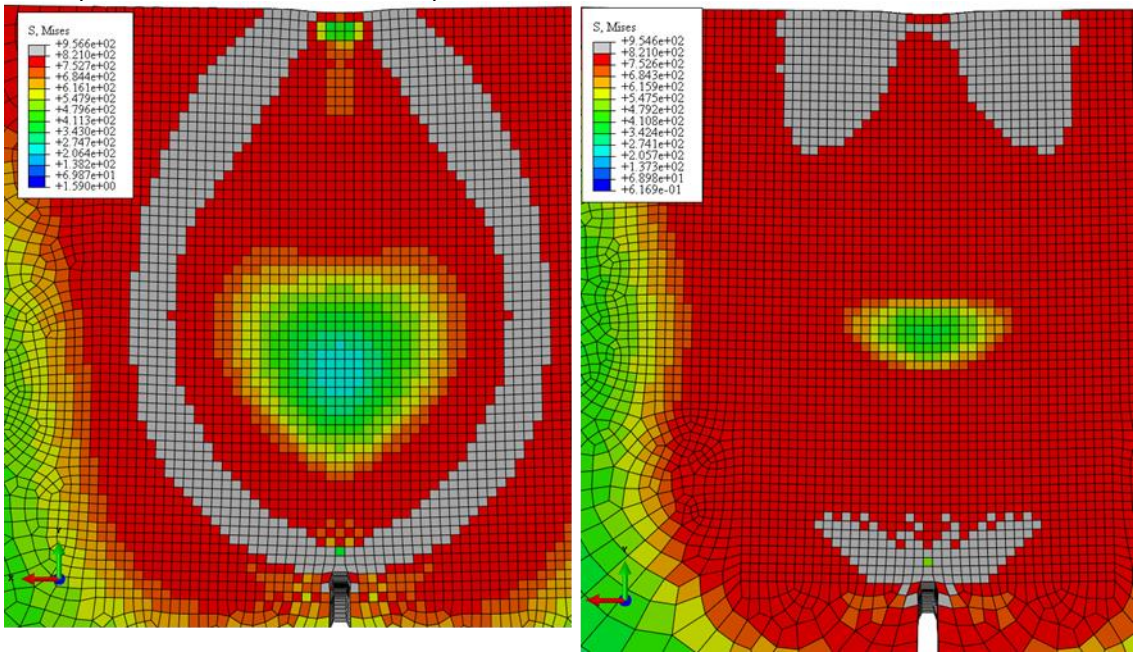

Figure 7-20 Actively yielding elements (grey) directly after the first elements in y-direction have been damaged (hidden from view). 24x24mm specimen (left) and 12x24mm specimen (right).

In Figure 7-20, many elements experience elastic relaxation due to crack growth in both the 24x24mm specimen and the 12x24mm specimen. This can be seen from the difference in elements actively yielding between Figure 7-19 and Figure 7-20. While the plastic hinge in the 24x24mm specimen is clearly visible from the currently yielding elements, this is not the case for the 12x24mm specimen. Interestingly, the ring shaped by the actively yielding elements in the 24x24mm specimen exactly overlays the ring of elements that are in a state of plane strain that was presented in Figure 7-1. The simulations feature continuous loading by a velocity-driven indenter, which causes the 24x48mm and the 12x24mm specimen to strain until the plastic hinge shape re-emerges as in actively yielding elements. Sometime after the first elements have been damaged, the zones of currently yielding elements presented in Figure 7-21 can be found.

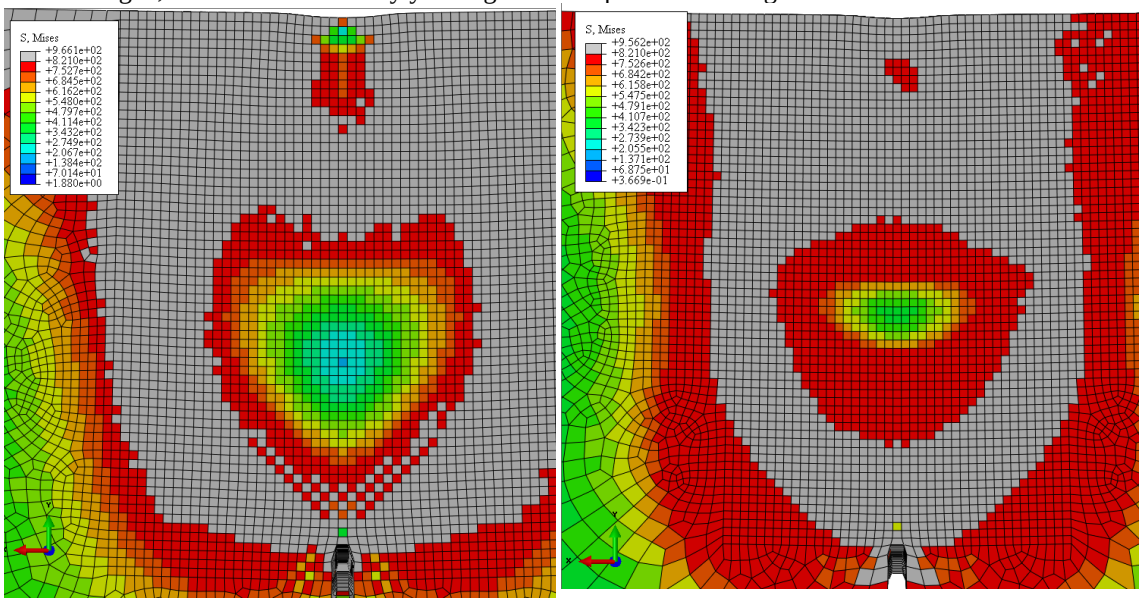

Figure 7-21 Actively yielding elements long after the first row of elements in ligament direction are damaged. 24x24mm specimen (left), 12x24mm (right)

The diamond shaped low stress concentrations that were also present before any damage had occurred are now back, until more elements fail. The situation shown in Figure 7-21 is taken from the situation just before the next big dip in the Force-CMOD curves. After this big dip, the plastic zone shape builds up again from the shape in Figure 7-20 to Figure 7-21. The big difference between the two aspect ratios that are observed in this thesis comes from the continuity of the ring shape of actively yielding elements in plane strain.

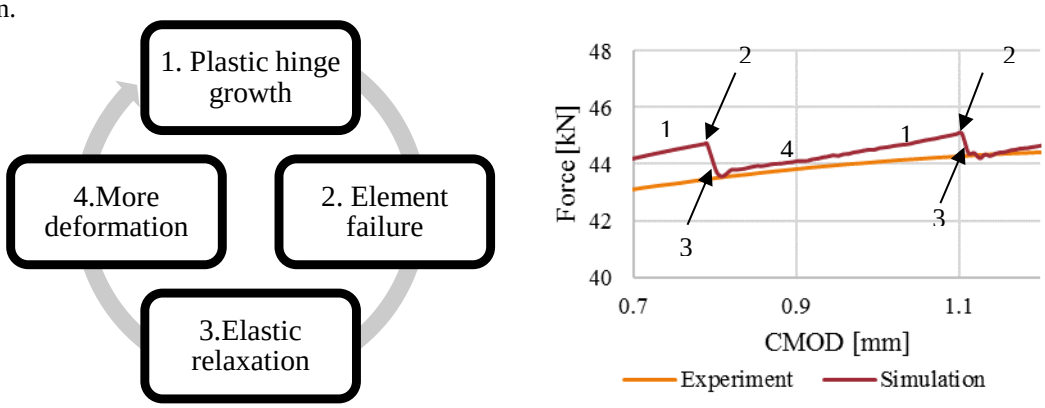

Figure 7-22 Pattern in plastic hinge development (left) and crack growth as it appears in the 24x24mm specimen (right).

From these observations, one can conclude that there is an effect of specimen width (B), in addition to the ligament size on the development of the plastic hinge. This is however a purely numerical effect, since in reality crack growth is a continuous process.

8 CONCLUSIONS

In this chapter, the answers to the questions raised in the introduction are presented. First the sub and main questions are repeated and then answered in order.

8.1 Sub questions

The first sub question is the following:

How does the size of the specimen effect the stress triaxiality and Lode parameter at the crack tip?

Answering the main question relies on an accurate description of the stress states around the crack tip, and therefore, it is necessary to review the effect of the specimen size on the stress states around the crack tip. This was done both theoretically, in chapter 3, and experimentally using the finite element method (chapter 6). To compare the stress states per specimen geometry, a point during loading was needed where they are comparable. This point was chosen as the time right before crack growth occurs. At this time, the CTOD is below the critical CTOD and as such, the conclusions below may only be applicable to small CTOD. The main takeaways from these simulations are the following:

1. The thickness of the specimen influences the stress triaxiality in such a way that a greater thickness results in a higher stress triaxiality on the crack flanks up to a certain plateau, after which, it is invariant in the centre. Conversely, a greater thickness results in a slightly lower stress triaxiality on the crack front (in ligament direction) at the centre of the thickness.
2. The stress triaxiality becomes constant at approximately equal distance from the free surface for all specimens. The ratio between the ligament size and thickness influences the rate with which the stress triaxiality converges to a constant value, demonstrated by the steepest slope being present in the 24x24mm specimen.
3. The influence of the specimen size on the Lode angle is less significant. The Lode angle is on the other hand very important to differentiate between plane stress and plane strain for small stress triaxialities ($\eta \leq \frac{2}{3}$) in all specimens. This becomes important near the free surface, where the stress triaxiality in the crack flank and crack tip are similar, but the flank has a significantly higher Lode angle. This, in combination with the higher plastic strain in the ligament, allows the shear lips to grow. Furthermore, the trend that a higher Lode angle requires a higher strain to fail, controls the extent to which the crack grows into the flank at the mid-surface during tunnelling.
4. The size of the ligament and thickness have little effect on the plastic strain in the elements in the ligament direction, but have major consequences for the plastic strain in the crack flanks. The influence of the ligament is most apparent at the symmetry plane for the flank elements, while the thickness has the greatest effect at the free surface for the elements in the crack flank.

These results clearly show that there is a significant effect of the specimen geometry on the stress and strain states on the crack front and flanks.

Strong stress gradients are present near the crack tip, due to a high stress intensity and crack blunting. To accurately capture these gradients, a large number of finite elements might be required. Whether this is feasible, is the motivation behind the second sub question:

Is it feasible to use a mesh so fine that the high stress gradients near the crack tip are accurately captured?

Meshes with three differently sized elements, ranging from 0.1mm to 0.3mm in the crack path were evaluated to select one for the calibration and application of the damage model. There was no discernible effect of the mesh size on the force-displacement curve. Before failure, the force-displacement curve is dominated by the global bending behaviour and plastic hinge formation of the beam. For the coarsest mesh, 40 elements were used over the critical bending section, which is more than enough to accurately simulate bending behaviour in a simple three-point bending experiment. The existence of the fatigue pre-crack and element wide crack front results in mesh size dependent strains near the crack tip. The stress magnitudes resulting from this are consequently also mesh size dependent and are calculated using a mesh size dependent plasticity model. Fortunately, the stress triaxiality and Lode angle depend more on the ratios between the three principal stress than on the magnitudes of those. During the mesh refinement study, major differences were found in the magnitudes of the stresses and strains, but only minor differences in the stress triaxiality and Lode angle. So, while the magnitudes of the stresses and strains are very different, the ratios between them are very similar. In short, with a finer mesh, the peaks in stress triaxiality are more accurately captured, and therefore, a slightly higher maximum stress triaxiality was found in the finest mesh than in the coarse mesh. Unfortunately, the analysis time is not only affected by the greater number of elements in the thickness, width and span of the beam, but also by the critical time step. Where the calibration of the specimen using the 0.2mm mesh takes about a week of full time computations on a dedicated server using 8 CPUs, the 0.1mm mesh will take more than a month. In the end, a constant element size of 0.2mm for all simulations was used in this thesis.
There was very little difference between the 0.2mm and 0.1mm mesh in the stress triaxiality and Lode angle on the first row of elements on the crack front and the crack flank. Those are the elements that are used during calibration and facilitate crack growth, and for this reason, the 0.2mm mesh is considered to be adequate. The peak in stress triaxiality that was shown earlier by Nakamura & Parks (1990) at a distance of about twice the CTOD from the crack tip is therefore only captured accurately when multiple elements fall within the distance of twice the CTOD. Consequently, a larger deformation of the beam results in a greater CTOD, which in turn means that the peak in stress triaxiality is captured by more elements.
In conclusion, it is possible to use a mesh so fine that the stress states in terms of Lode angle and stress triaxiality on the crack front and crack flanks are converged, provided that the deformation is large enough to allow multiple elements to characterise the peak in stress triaxiality. While there are vast differences between the equivalent plastic strain found in the three different meshes at deviation between simulation and experiment, the point of deviation in terms of CMOD was found to be approximately equal. The simple reason for this is that the Force-CMOD characteristic is dominated by the global bending behaviour of the beam and plastic hinge, and unaffected by the local stress state at the crack tip. Using the 0.2mm mesh, it is feasible to do a full calibration within a week.

The third and fourth sub-question have a strong relation and can be answered together:

Is the continuum damage approach variant that is used here appropriate for the simulation of fracture in SENB specimen?
Is it possible to accurately simulate tunnelling and shear lips with this damage mechanics model?

The FCD model introduced in this thesis is able to simulate the path of the crack through orthotropic damage. Furthermore, the force-displacement curves of the simulations match the force-displacement curves of the experiments until a certain CMOD. Beyond this CMOD, the simulated reaction force is conservative. Multiple reasons for this can be proposed, some of which are presented in the future work/recommendations, following the conclusions. One of the main reasons is related to the way the crack growth is modelled. The crack path discretisation, especially at the symmetry plane where the crack zigzags on a scale of multiple elements, tends to weaken the bearing capacity more than the straight crack observed in reality. Since this zigzag pattern appears to consist of a constant number of elements, unrelated to the size of these elements, it stands to reason that the impact on the bearing capacity will decrease as the element size decreases.

8.2 Main question

The main question is the following:

Is a stress triaxiality, Lode angle and plastic strain based failure model, calibrated from a single SENB specimen, able to correctly predict failure in differently sized SENB specimens?

This can be split into two parts:

1. Is it possible to calibrate a failure model, where the strain at failure is a function of stress triaxiality and Lode angle, using only a single SENB specimen?
2. Is this failure model able to correctly predict crack growth in SENB specimens with different geometries?

The first part of the main question is answered in chapter 5. The iterative procedure presented in this thesis is able to find a large number of combinations of stress triaxiality, Lode angle and equivalent plastic strain for which an element should fail. The procedure is driven by measuring the deviation between the measured force-CMOD curve and the simulated one. A new data point is obtained with every deviation that is found. The main assumption in selecting new data points from critical elements is that the critical element borders an already damaged element and it has the highest equivalent plastic strain of all elements bordering any damaged element. In the end, 80 points were used to fit the three parameters of the Hosford-Coulomb failure criterion. It is noteworthy that the vast majority of points from 60 to 80 were found in ranges of stress triaxiality and Lode angle that were already densely populated by previously found points. This resulted in a failure surface which bears much resemblance to a stress triaxiality dependent maximum shear criterion. The points that define the surface range in stress triaxiality between 0.1 and 2.2, and in Lode angle between -0.4 and 0.7. In other research, e.g. (Bai & Wierzbicki, 2010) and (Kofiani, Nonn, & Wierzbicki, 2013), multiple calibration tests were used. However, the calibration tests in those approaches not only deliver just a single calibration point each, they also span a smaller range of stress triaxialities than the calibration procedure presented in this thesis. While the range of stress triaxialities is higher in this calibration procedure, few calibration points are found in the domain of stress triaxiality where the strongest gradient of failure strain is expected. It must be noted that in the domain with high gradients of failure strain, mainly consisting of negative and very small stress triaxialities, very high failure strains are typically found. This range is represented in the paper by Bai and Wierzbicki (2010) by upsetting tests. Since the 3-point bending test used in this thesis does not fail in compression, it is impossible to obtain those values from this test. Consequently, the calibration produces an accurate failure surface for stress triaxialities in the range of 0.1 to 2.2, but probably has little value for use of failure prediction of this material in compression. Additionally, both the procedures used by Kofiani et al. (2013) and Bai and Wierzbicki (2010) feature a greater range of Lode angles. In those procedures, the failure data from smooth round bars and notched round bars is assumed to deliver the failure strain for a Lode angle of 1 (in tension) and -1 (in compression). While there is no doubt that the dominant Lode angle in these specimen is indeed 1 and -1, other stress states are present in these specimens. This is most easily visible from the cup and cone shape that is seen in the round bars. Whether the assumption that from these experiments failure strains can be found for Lode angles of 1 and -1 is correct, is far beyond the scope of this research project.
In conclusion, this procedure provides calibration points in a large range of stress triaxialities and Lode angles in the tensile domain of stress states. Any failure surface relating failure strain to stress triaxiality and Lode angle can therefore be fitted to these data points. The resulting failure surface is mesh size dependent and during calibration (and application) it is crucial that the mesh size is small enough that the strong gradients in stress near the crack tip are accurately captured.

The second part of the main question is:

Is this failure model able to correctly predict crack growth in SENB specimens with different geometries?

Correct crack growth prediction is defined in the following ways:

1. No or small differences between the force-CMOD measured in the experiment and the simulation.
2. Agreement between the crack path in the experiment and simulation.

The failure model obtained from the 12x24mm specimen was applied to the specimens with dimensions 24x24mm and 24x48mm. These simulations were carried out with identical element size as used in the calibration in the region where crack growth is expected. In both these other geometries, good agreement was found for crack initiation. The maximum deviation in force before crack initiation was 2.5%. As the crack mouth widens, the simulation and experiment are in good agreement until a certain point. For the 12x24mm and 24x24mm specimen, the model with failure yields results in 1% deviation in simulated force for at least three times the plastic crack mouth opening. This is sufficient to accurately capture the force maximum seen in these experiments. In the case of the 24x48mm specimen, there is good agreement until twice the plastic crack mouth opening. At the CMOD related to the force maximum, the simulated force is 2.5% lower than in the experiment. Afterwards, all models consistently yield smaller simulated forces than the experiment. Reasons for this growing deviation include the crack growth discretisation corresponding to the FCD model, not using a tuned damage evolution rule and element size.
The crack paths were compared for the specimen, and in all cases, there is a clear indication of shear lip growth and tunnelling in the simulation. The tunnelling portion however is plagued by a zigzag pattern that, while it occurs in microscopic scale in the real world, weakens the specimen more than in the experiments. It was possible to compare the extent of the crack growth on the free surface for the 24x48mm specimen to the simulation and similar crack lengths were observed. The crack width, if one assumes that all damaged elements as part of the crack, is much wider than observed in experiments. This assumption is not completely correct, but the fact that 4 elements through the crack width are damaged indicates that the extent of the damage is greater in the simulation than in reality. Again, this difference is completely due to the crack discretisation using the FCD model.

In conclusion:
It is possible to calibrate a stress triaxiality, Lode angle and equivalent plastic strain based failure model from a single SENB specimen. The resulting model is able to correctly predict the onset and the advance, to some extent, of material separation in SENB experiments with other dimensions, provided that the same characteristic element size is used as in the calibration.

9 RECOMMENDATIONS AND FUTURE WORK

One could ask the question: When the crack path on the free surface does not deviate much from the crack path seen in the experiment, then why is there a growing deviation between simulation and experiment? There are multiple answers to this question. First of all, while it is possible to check the crack path on the free surface, it was impossible to do the same for the symmetry plane using the tests carried out here. It is therefore unknown if the amount of tunnelling (crack growth on the plane of the fatigue pre-crack in the ligament direction) is correct for these values of CMOD. The ratio between tunnelling and shear lip growth in the calibration as well as the application is greatly influenced by the stress triaxiality dependence of the failure model. Elements that are in the ligament direction tend to have a much higher stress triaxiality than elements on the flanks of the crack tip. If there is a strong dependence on the stress triaxiality, then tunnelling is more prominent, while for a less strong dependence, shear lip growth is more prominent. The effect of the Lode angle is similar; a strongly Lode angle dependent failure locus promotes tunnelling, while a less Lode angle dependent model promotes shear lip growth. This is because elements on the crack flank have a higher Lode angle than elements in ligament direction. That being said, it was also observed in Chapter 5.2.4 that the Lode angle can change drastically by the damaging of a neighbour in the area where tunnelling is expected. This provides a combination of high stress triaxiality and high Lode angle, whereas the crack flanks experience small stress triaxiality and medium Lode angles. With the above recollection from chapter 5, it can be stated that there is a fine balance between Lode angle dependence and stress triaxiality dependence. Tilting this balance can cause excessive tunnelling or excessive shear lip growth or both. Fitting formula's such as the Hosford-Coulomb model or the Modified Mohr-Coulomb model to the acquired data points help in creating this balance.

A second reason why there is a growing deviation between the experimental force-CMOD curve and the simulation for increasing CMOD values is related to the softening function. As was stated in the scope (Chapter 1.2) and Chapter 5.2.4, no attention is given to the softening effect, and to diminish its effect on the simulation, almost instant element degradation was enforced. Increasing the damage range over which the element goes from undamaged to fully damaged will spread the drop in force over a greater range of CMOD.

In the simulation in this thesis, reduced brick (C3D8R) elements are used. While using these avoid problems such as shear locking, there is evidence of hour glassing near the crack tip. The energy that was needed to correct for hour glassing was more than the elastic deformation energy, but less than the plastic deformation energy. This can to some extent be solved by using a less structured mesh, but one must take care that the characteristic element length remains consistent were element failure is expected. Alternatively, one could turn to using enhanced brick elements that use incompatible modes in combination with full integration to overcome both hour glassing and shear locking. In Abaqus/Explicit, these elements are of the type C3D8I, but they are not commonly used even though they are claimed to be more accurate than C3D8R and C3D8. Future work may focus on using these elements, but if the same fictitious crack damage model is used that is introduced in this thesis, one may consider using a crack orientation model within an element to assure a continuous fictitious crack.

Knowing that the stress state in terms of stress triaxiality and Lode angle are independent of the mesh size near the crack tip, one could form the hypothesis that it is possible to calibrate for a certain mesh size, and then scale this to be applied on a problem with another mesh size. This may be possible, provided that the mesh is still fine enough to capture the strong gradients near the crack tip.

10 REFERENCES

Anderson, T. (2005). *Fracture Mechanics, Fundamentals and Applications 3rd edition.* Boca Raton: Taylor and Francis Group.

ASTM. (1989). *E1290-89: Standard test method for crack-tip opening displacement (CTOD) fracture toughness measurement.* West Conshohocken: American Society for Testing and Materials.

Bai, Y., & Wierzbicki, T. (2008). A new model of metal plasticity and fracture with pressure and Lode dependence. *International Journal of Plasticity*, 1071-1096.

Bai, Y., & Wierzbicki, T. (2010). Application of extended Mohr–Coulomb criterion to ductile fracture. *International journal of fracture*, 1-20.

Bakker, A. (1990). Influence of material flow curve modelling on fracture mechanics evaluations. *Numerical methods in Fracture Mechanics: Proceedings of the Fifth Int. Conf. held in Freiburg*, (pp. 443-449). Freiburg.

Barsom, J., & Rolfe, S. (1987). *Fracture and Fatigue Control in Structures 2nd edition.* Englewood Cliffs, NJ: Prentice Hall.

Betegón, C., & Hancock, J. (1991). Two-Parameter Characterization of Elastic-Plastic Crack-Tip Fields. *Journal of applied mechanics vol 58*, 104-110.

Bilby, B., Goldthorpe, G., & Howard, I. (1986). A Finite Element Investigation of the Effect of Specimen Geometry on the Fields of Stress and Strain at the Tip of Stationary Crack. *Size Effects in Fracture*, 37-46.

Bridgman. (1952). *Studies in large plastic flow and fracture.* New York: McGraw-Hill Book Company.

British Standards. (1991). *BS7448 part 1:method for determining of KIc, critical crack tip opening displacement (CTOD) and critical J values of fracture toughness for metallic materials under displacement controlled monotonic loading at quasistatic rates.* London: British Standards Institution.

Chaboche, J. (1980). Sur l'utilisation des variables d'etat interne pour la description du comportement viscoplastique et de la rupture par endommagement. *Nowacki WK (ed) Problèmes Non-Linéaires de Mécanique (Proceedings of French-Polish symposium, Cracow 1977)* (pp. 137-159). Warsaw: PWN.

Coppejans, O., & Walters, C. (2017). DETERMINATION OF PARAMETERS FOR THE DAMAGE MECHANICS APPROACH TO DUCTILE FRACTURE BASED ON A SINGLE FRACTURE MECHANICS TEST. *36th International Conference on Ocean, Offshore and Arctic Engineering* (pp. -). Trondheim: ASME.

Cotterell, B., & Rice, J. (1980). Slightly Curved or Kinked Cracks. *International Journal of Fracture, vol. 16*, 155-169.

Dagadu, N. (2015). *Calibration of a Stress Triaxiality and Lode Parameter Dependent Damage Model Based on Correlation with Failure in an SENB Fracture Mechanics Test.* Delft: -.

Dassault Systèmes. (2014). 37.1.3 Contact damping. In *Abaqus Analysis User's Guide* (p. 2).

Dodds, R., Anderson, T., & Kirk, M. (1991). A framework to correlate a/W ratio effects on elastic-plastic fracture toughness (Jc). *International journal of Fracture*, 1-22.

Du, Z., & Hancock, J. (1991). The Effect of Non-Singular Stresses on Crack-Tip Constraint. *Journal of the Mechanics and Physics of Solids vol 39*, 555-567.

Element materials technology. (2016). *Trekproef met rekopnemener TNO SW3A1+2.* Breda: Element.

Griffith, A. (1920). The phenomena of rupture and flow in solids. *Philosophical Transactions*, 163-198.

Gu, G., & Mohr, D. (2015). Anisotropic Hosford–Coulomb fracture initiation model: Theory and application. *Engineering Fracture Mechanics*, 480-497.

Hillenborg, A. (1991). Application of the fictitious crack model to different types of materials. *International Journal of Fracture*, 95-102.

Hutchinson, J. (1968). Singular behaviour at the end of a tensile crack in a hardening material. *Journal of the Mechanics and Physics of Solids*, (16):13-31.

Impact and Crashworthiness Lab (ICL), MIT. (2009, January). ABAQUS/EXPLICIT USER MATERIAL FOR RATE-INDEPENDENT, 3D Hill 48 ANISOTROPIC PLASTICITY WITH Morh-Coulomb Fracture Criterion.

Irwin, G. (1956). Onset of fast crack propagation in high strength steel and aluminum. *Sagamore research conference proceedings Vol.2*, (pp. 289-305). Sagamore.

Irwin, G. (1957). Analysis of stresses and strains near the end of a crack traversing a plate. *Journal of applied mechanics*, 109-114.

Johnson, G., & Cook, W. (1985). Fracture characteristics of three metals subjected to various strains, strain rates, temperatures and pressures. *Engineering Fracture Mechanics*, 31-48.

Johnson, G., & Cook, W. (1985). Fracture characteristics of three metals subjected to various strains, strain rates, temperatures and pressures. *Engineering Fracture Mechanics*, 31-48.

Kaufman, J., & Nelson, F. (1973). More on Specimen Size Effects in Fracture Toughness Testing. In ASTM, *ASTM STP559* (pp. 74-98). Philadelphia, PA: ASTM.

Kejiang Han, J. S. (2014). The effect of constraint on CTOD fracture toughness of API X65 steel. *Engineering Fracture Mechanics*, 167-181.

Kofiani, K., Nonn, A., & Wierzbicki, T. (2013). New calibration method for high and low triaxiality and validation on SENT specimens of API X70. *International Journal of Pressure Vessles and Piping, Vol. 111-112*, 187-201.

Larsson, S., & Carlsson, A. (1973). Influence of Non-Singular Stress Terms and Specimen Geometry on Small-Scale Yielding at Crack Tips in Elastic-Plastic Material. *Journal of the Mechanics and Physics of Solids, vol 21*, 263-278.

Lemaitre, J., & Chaboche, J. (1978). Aspect phénoménologique de la rupture par endommagement. *Journal de Mécanique Appliquée 2*, 317-365.

McClintock, F. (1968). A Criterion for ductile fracture by growth of holes. *Journal of applied Mechanics*, 363-371.

McMeeking, R., & Parks, D. (1979). On criteria for J-dominance of crack tip fields in large scale yielding. In ASTM, *ASTM STP 668* (pp. 175-194). Philadelphia, PA: ASTM.

Mohr, D., & Marcadet, J. S. (2015). Micromechanically-motivated phenomenological Hosford–Coulomb model for predicting ductile fracture initiation at low stress triaxialities. *International Journal of Solids and Structures 67-68*, 40-55.

Murakami, S. (2012). *Continuum Damage Mechanics.* Tokyo: Springer.

Nakamura, T., & Parks, D. (1990). Three-dimensional crack front fields in a thin ductile plate. *Journal of the Mechanics and Physics of Solids vol 38*, 787-812.

Nevalainen, M., & Dodds, R. (1995). Numerical investigation of 3-D constraint effects on brittle fracture in SE(B) and C(T) specimens. *International journal of fracture*, 131-161.

O'Dowd, N., & Shih, C. (1991,1992). Family of Crack-Tip Fields Characterization by a Triaxiality Parameter part I and II. *Journal of the Mechanics and Physics of Solids vol 39 and 40*, 898-1015,939,963.

O'Dowd, N., & Shih, C. (2002). Two-parameter fracture mechanics: theory and applications. In ASTM, *Fracture mechanics. ASTM STP 1207* (pp. 21-47). American Society for Testing and Materials.

Parks, D. (1991). Three-Dimensional Aspects of HRR-Dominance. *Defect Assessment in Components - Fundamentals and Applications*, 205-231.

Rashid, Y. (1968). Analysis of prestressed concrete pressure vessels. *Nuclear Eg. Des, 7*, 334-344.

Rice, J. (1968). A path dependent integral and the approximate analysis of strain concentrations by notches and cracks. *Jorunal of Applied Mechanics*, 35(2):379-86.

Rice, J. (1974). Limitations to the small-scale yielding approximation for the crack tip plasticity. *Journal of the mechanics and physics of solids, vol 22*, 17-26.

Rice, J., & Johnson, M. (1970). The role of large crack tip geometry changes in plane strain fracture. In M. Kanninen, & et al., *Inelastic behaviour of solids* (pp. 641-72). New York: McGraw-Hill.

Rice, J., & Rosengren, G. (1968). Plane strain deformation near a crack tip in a power law hardening material. *Journal of the Mechanics and Physics of Solids*, 16(1):1-12.

Rice, J., & Tracey, D. (1969). On the ductile enlargement of voids in triaxial stress fields. *Journal of the Mechanics and Physics of Solids*, 201-217.

Shih, C., & German, M. (1981). Requirements for a one parameter characterization of crack-tip fiels by the HRR singularity. *International journal of fracture vol 17*, 27-43.

Tvergaard, V., & Hutchinson, J. (1994). Effect of the T-Stress on Mode I Crack Growth Resistance in a Ductile Solid. *International journal of solids and structures vol 31*, 823-833.

Walters, C., Voormeeren, L., Janssen, M., & Wallin, K. (2013). VALIDATION OF THE ACCEPTABILITY OF 10X20 MM SPECIMENS FOR FRACTURE TOUGHNESS DETERMINATION OF HIGH-STRENGTH STEELS. *ASME 2013 32nd International Conference on Ocean, Offshore and Arctic Engineering* (pp. 1-9). Nantes: ASME.

Wells, A. (1961). Unstable crack propagation in metals: cleavage and fast fracture. *Proceedings of the crack propagation symposium, 1*, paper 84.

Westergaard, H. (1939). Bearing pressures and cracks. *Journal of Applied Mechanics*, 49-53.

Wierzbicki, T., & Xue, L. (2005). *On the effect of the third invariant of the stress deviator on ductile fracture.* Cambridge, MA: Impact and Crashworthiness Laboratory, Massachusetts Institute of Technology.

Williams, J. (1957). On the stress distribution at the base of a stationary crack. *Journal of Applied Mechanics*, 109-114.

Xue, L. (2007). Damage accumulation and fracture initiation in uncracked ductile solids subject to triaxial loading. *International Journal of Solids and Structures*, 5163-5181.

Y. Bai, T. W. (2008). A new model of metal plasticity and fracture with pressure and Lode dependence. *International Journal of Plasticity*, 1071-1096.

Yuan, H., & Brocks, W. (1998). QUANTIFICATION OF CONSTRAINT EFFECTS IN ELASTIC-PLASTIC CRACK FRONT FIELDS. *Journal of the mechanics and physics of solids vol 46*, 219-241.

11 APPENDICES

APPENDIX A PLASTICITY MODEL FORMULAS AND MESHES

The formulas to calculate the true strains from the engineering strains is presented below:

$$\boldsymbol{\varepsilon_{true} = LN(\varepsilon_{engineering} + 1)} \quad (11.1)$$

$$\sigma_{true} = \sigma_{engineering} * (1 + \varepsilon_{engineering}) \quad (11.2)$$

The meshes used in the calibration of the plasticity model and the refinement study for these meshes is presented in this appendix.

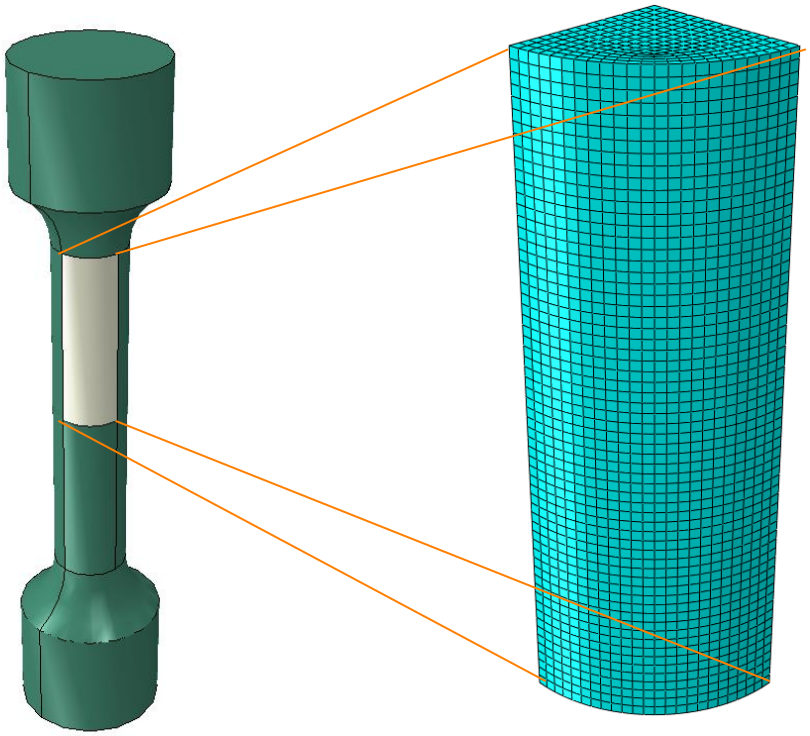

The height of the meshed part in the figure above is 25mm, which is the maximum distance between the measuring point of the strain gage and the middle of the specimen. All meshes presented here share that same dimension and share the radius of the specimen, which is 6.25 mm. All meshes have an artificial reduction of radius at the part of the model that is displaced, to enforce the stress concentration and necking there. This radius of nodes om the outer layer of the mesh is 6.24mm. In all plasticity models an explicit analysis is used with a velocity loading applied to the bottom of the model and symmetry conditions with respect to the outward normal of the faces that are cut from the full-scale model presented above.

The meshes that are used are the following:

Table 11-1 Mesh information tensile simulations

Mesh name	Average element size [mm]	Number of elements
25x04mm (coarse)	0.4	16268
25x03mm (medium	0.3	36437
25x02mm (fine)	0.2	118000
25x01mm (ultrafine)	0.1	1876982

Also, to investigate the geometrical size effect, the following mesh is used:

Table 11-2 Mesh information full geometry mesh tensile test

Mesh name	Average element size [mm]	Number of elements
12.5x01mm (prop)	0.1	118000

The proportional model is (geometry wise) an exact scaled version of the other models, so one would expect the results to be an exact scaled version of the results in the normal sized simulations. The geometry is scaled by a factor 2 and consequently the cross-sectional area by a factor 4. This is tested by comparing the force-displacement values of both experiments, while scaling the results of the proportional model by a factor 4.

Table 11-3 Boundary condition tensile test simulation

Name	Time step [s]	Velocity [mm/s]	Total displacement [mm]
25x01mm	6	1	6
12.5x01mm	3	1	3

The relative difference between the recorded forces ($F_{simuatlion\ 1}/F_{simulation\ 2}$) is presented in the graph below:

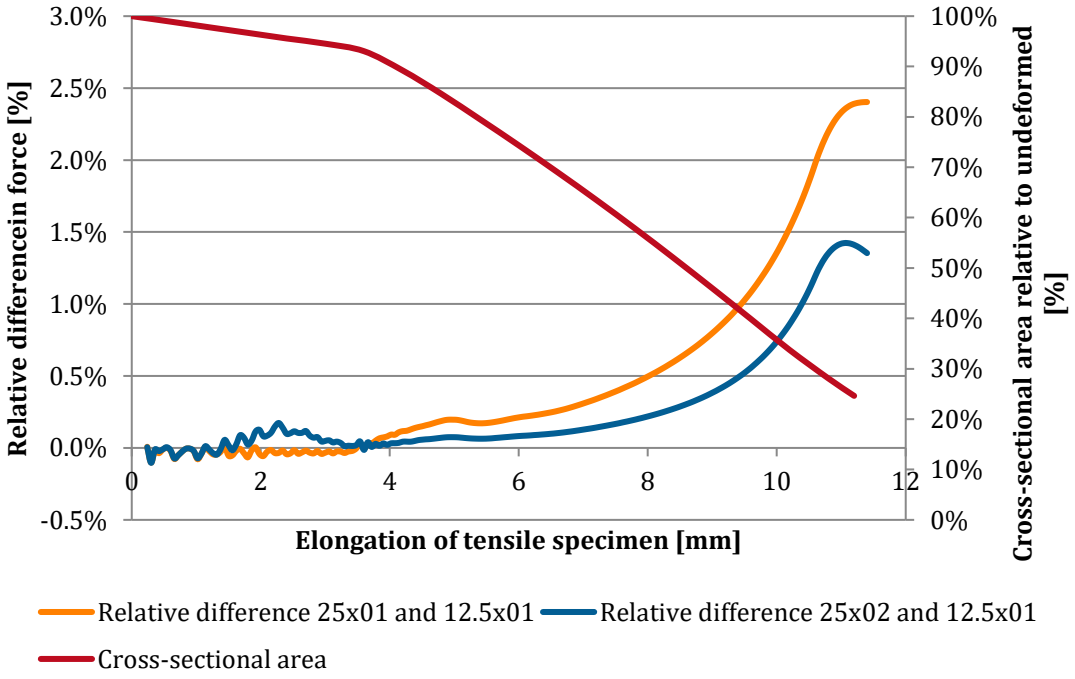

Figure 11-1 Relative differences in force measurements for different mesh sizes.

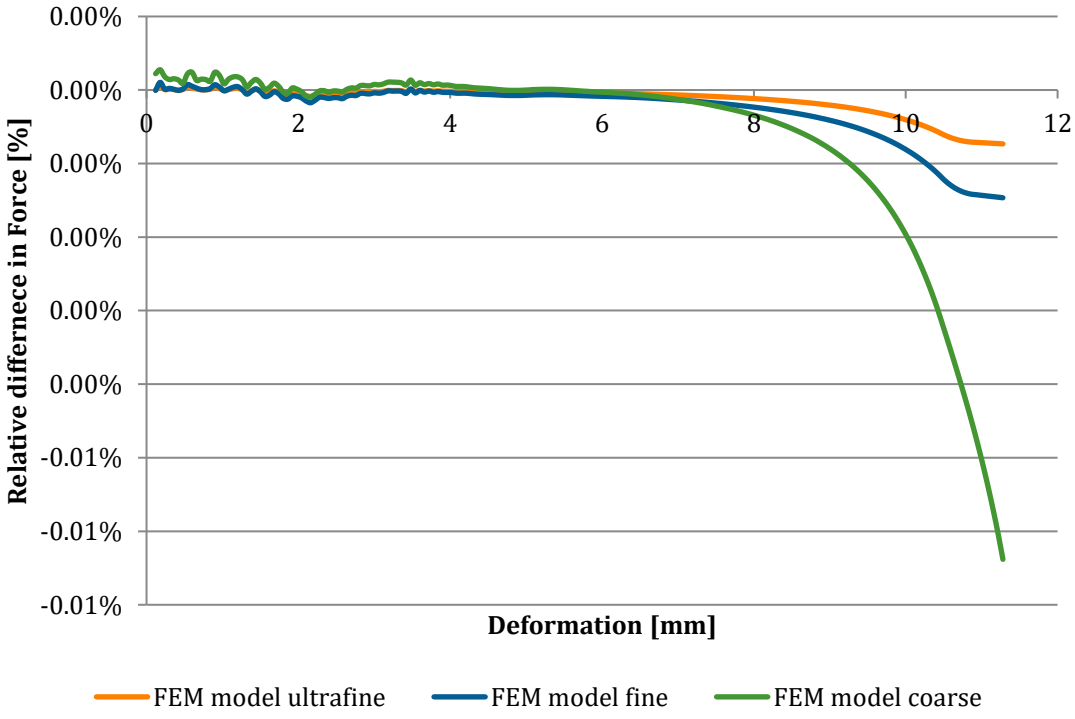

Figure 11-2 Mesh refinement study; relative deviation from experiment

APPENDIX B DAMAGE MODEL AND MESHES

In this section, the orthotropic (FCD) damage model is coarsely explained. The most important difference between this damage model and regular isotropic damage is that damage is only applied to forces with a certain direction. For this purpose, at the time the failure criterion is met, the largest principal stress is found its eigenvector is set as the vector to which damage is applied. In subsequent steps, the current stress tensor is rotated to the coordinate system in which the damaged direction is known (using the eigenvectors of the principal stresses found in the timestep where the element was damaged). Then, the newly obtained stress tensor is multiplied with a damage tensor, reducing all components sharing the same index as the damaged direction.
In somewhat more detail, this is explained in the section below.

The application of the damage model is further explained below in various timesteps:

$t=t_f$

Following the ordinary material routine containing a plastic step, the Lode angle and stress triaxiality are calculated. The element can be tagged for damage in the following ways, depending on the procedure:

1. During the calibration procedure:

   The stress state of the element, expressed in Lode angle and stress triaxiality is checked against a list of failure combinations. This list of failure combinations contains a set of tiles with a particular failure strain, Lode angle and stress triaxiality. If the current strain in the element exceeds the strain in the failure combination, the element is tagged for damage by setting the damage parameter $D_{t+\Delta t}$ to 1.

   Example:

   The current Lode angle in the element being evaluated is 0.8, the stress triaxiality is 1.9 and the strain is 0.22. This state is compared to the list of failure combinations, presented below:

Lower bound triax-iality	***Upper bound triax-iality***	***Lower bound Lode angle***	***Upper bound Lode angle***	***Failure strain***
1.880	*1.890*	*0.780*	*0.790*	*0.23*
1.895	*1.905*	*0.795*	*0.805*	*0.19*

   The current element fits within the bound set by the second failure combination in the list above and exceeds the failure strain of 0.19 belonging to that stress state. This state variable controlling the damage state ($D_{t+\Delta t}$) is set to 1.

2. During the application of the failure locus obtained through a full calibration:

   A surface function or polynomial containing failure combinations was fitted to the results of the calibration run done in a different simulation. This function uses the Lode angle and stress triaxiality as input parameters, and the output is the failure strain. Elements accumulate damage through the damage evolution integral, until a value of 1 is exceeded. If this value is reached, the next time step will be the first time step where the element's response to strains is weakened.

$$\boldsymbol{D(\bar{\varepsilon}_p) = \int_0^{\varepsilon_p} \frac{d\bar{\varepsilon}_p}{f(\eta, \bar{\theta})}} \qquad (11.3)$$

For both:
At this time, the direction cosines used to rotate the stress tensor to the principal stress tensor are recorded, as well as the index of that tensor corresponding to the direction cosine of the maximum principal stress in the current time-step. In subsequent time-steps, the response in terms of stress in this direction will be gradually reduced to 0, effectively reducing this element to a plane stress element indifferent to straining in one direction.

The stress tensor in matrix notation has the following form:

$$\Sigma_{xyz}^{t} = \begin{pmatrix} \sigma_{xx}^{t} & \sigma_{xy}^{t} & \sigma_{xz}^{t} \\ \sigma_{yx}^{t} & \sigma_{yy}^{t} & \sigma_{yz}^{t} \\ \sigma_{zx}^{t} & \sigma_{yz}^{t} & \sigma_{zz}^{t} \end{pmatrix} \tag{11.4}$$

The principal stresses and eigenvectors can now be calculated

$$S_{123}^{t} = \begin{bmatrix} s_1^t & 0 & 0 \\ 0 & s_2^t & 0 \\ 0 & 0 & s_3^t \end{bmatrix} \quad \text{and} \quad V = \begin{bmatrix} V_{11} & V_{12} & V_{13} \\ V_{21} & V_{22} & V_{23} \\ V_{31} & V_{32} & V_{33} \end{bmatrix} \tag{11.5}$$

Tensor V contains the eigenvectors corresponding to the eigenvalues in tensor Σ_{123}^{t}. The subscript 123 denotes the coordinate system in which these stresses are given. By definition the tensor V is an orthogonal rotation matrix and therefore the following properties hold:

$$S_{123}^{t} = V^{-1} S_{xyz}^{t} V = V^{T} S_{xyz}^{t} V$$

$$S_{xyz}^{t} = V S_{123}^{t} V^{-1} = V S_{123}^{t} V^{T} \tag{11.6}$$

Matrix V can thus be used to rotate the stress tensor from the original xyz coordinate system to the coordinate system of the principal stresses and vice versa.

Example: Let σ_1 be the greatest principal stress. Then index 1 is saved for the next time steps.

$t=t_f+\Delta t*n$ for n from 1 to inf.

This time step starts with calculation the value of the softening function:

$$\omega = \frac{2}{\left(D_{crit}\right)^3} \cdot (D_t - 1)^3 - \frac{3}{\left(D_{crit}\right)^2} \cdot (D_t - 1)^2 + 1 \tag{11.7}$$

The shape of the softening function can be found in the figure below. Here the critical damage value D_{crit} is set to 0.4 and a smooth decline in the damage function can be seen. This smooth decline is introduced to minimise potential dynamic behaviour.

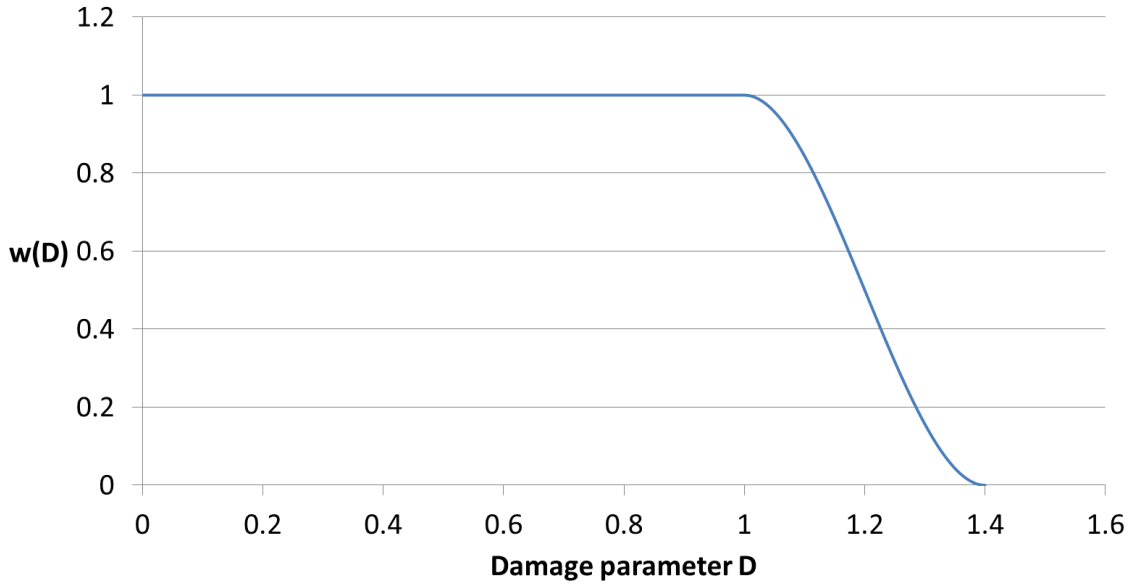

Calculate trial stress state (Voigt's notation):

$$\sigma_t^{trial} = \begin{bmatrix} \sigma_{xx}^t \\ \sigma_{yy}^t \\ \sigma_{zz}^t \\ \sigma_{xy}^t \\ \sigma_{yz}^t \\ \sigma_{zx}^t \end{bmatrix} = \begin{bmatrix} \sigma_{xx}^{t-\Delta t} \\ \sigma_{yy}^{t-\Delta t} \\ \sigma_{zz}^{t-\Delta t} \\ \sigma_{xy}^{t-\Delta t} \\ \sigma_{yz}^{t-\Delta t} \\ \sigma_{zx}^{t-\Delta t} \end{bmatrix} + \begin{bmatrix} \lambda+2\mu & \lambda & \lambda & & & \\ \lambda & \lambda+2\mu & \lambda & & & \\ \lambda & \lambda & \lambda+2\mu & & & \\ & & & \mu & & \\ & & & & \mu & \\ & & & & & \mu \end{bmatrix} \begin{bmatrix} \Delta\varepsilon_{xx}^t \\ \Delta\varepsilon_{yy}^t \\ \Delta\varepsilon_{zz}^t \\ \Delta\varepsilon_{xy}^t \\ \Delta\varepsilon_{yz}^t \\ \Delta\varepsilon_{zx}^t \end{bmatrix} \quad \textbf{(11.8)}$$

The trial stress tensor in matrix notation has the following form:

$$\Sigma_{xyz}^t = \begin{bmatrix} \sigma_{xx}^t & \sigma_{xy}^t & \sigma_{xz}^t \\ \sigma_{yx}^t & \sigma_{yy}^t & \sigma_{yz}^t \\ \sigma_{zx}^t & \sigma_{zy}^t & \sigma_{zz}^t \end{bmatrix} \quad (11.8)$$

Rotate to 123 coordinate system:

$$\Sigma_{123}^t = V^{-1}\Sigma_{xyz}^t V = V^T\Sigma_{xyz}^t V \quad (11.9)$$

The following stress tensor in 123 coordinate system results:

$$\Sigma_{123}^t = \begin{bmatrix} \sigma_{11}^t & \sigma_{12}^t & \sigma_{13}^t \\ \sigma_{21}^t & \sigma_{22}^t & \sigma_{23}^t \\ \sigma_{31}^t & \sigma_{32}^t & \sigma_{33}^t \end{bmatrix} \quad (11.10)$$

In order to apply damage to stresses in the direction of the maximum principle stress, the index from timestep t= $t_{f+\Delta t}$ is recalled. All components with that index are then multiplied by softening function ω.

$$\Sigma_{ij}^t = \begin{cases} \Sigma_{ij}^t, \ for\ i \neq index\ and\ for\ j \neq index \\ \omega * \Sigma_{ij}^t, \ for\ i = index\ and/or\ for\ j = index \end{cases} \quad (11.11)$$

Example: Taking index 1 from time step t=$t_{f+\Delta t}$ the following effective stress tensor in 123 coordinate system is found:

$$\Sigma_{123}^t = \begin{bmatrix} \omega\sigma_{11}^t & \omega\sigma_{12}^t & \omega\sigma_{13}^t \\ \omega\sigma_{21}^t & \sigma_{22}^t & \sigma_{23}^t \\ \omega\sigma_{31}^t & \sigma_{32}^t & \sigma_{33}^t \end{bmatrix} \quad (11.12)$$

Rotate the effective stress tensor in 123 coordinate system back to the xyz coordinate system:

$$\Sigma_{xyz}^t = V\Sigma_{123}^t V^{-1} = V\Sigma_{123}^t V^T \quad (11.13)$$

Continue with ordinary elastic or plastic step. In case of the plastic step, the same procedure in rotating and applying damage is used during the return mapping algorithm as presented in formulae 5 through 10.

Meshes

The meshes that are used in the mesh sensitivity study were already presented in Table 5-7 in chapter 5. The meshes used in the application phase have the same characteristic element size (0.2mm) but different shapes and therefor a different number of elements.

Specimen	**Number of elements**
12x24mm	200942
24x24mm	464760
24x48mm	876840

APPENDIX C 3D PLOTS (DIGITAL VERSION ONLY)

1. Stress triaxiality in 12x24mm specimen
2. Stress triaxiality in 24x24mm specimen
3. Stress triaxiality in 24x48mm specimen
4. Lode angle in 12x24mm specimen
5. Lode angle in 24x24mm specimen
6. Lode angle in 24x48mm specimen
7. Crack growth in 24x48mm specimen , with damage.
8. Crack growth in 24x48mm specimen , with equivalent plastic strain.
9. Crack growth in 24x48mm specimen , with Lode angle.
10. Crack growth in 24x48mm specimen , with von Mises stress.
11. Crack growth in 24x48mm specimen , with stress triaxiality.

(not available on hardcopy)

LODE ANGLE

Model: Bx2B
Just before first failure.

Legend:

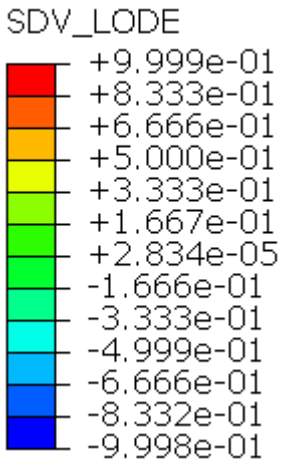

White elements have no value and are outside the subroutine domain.

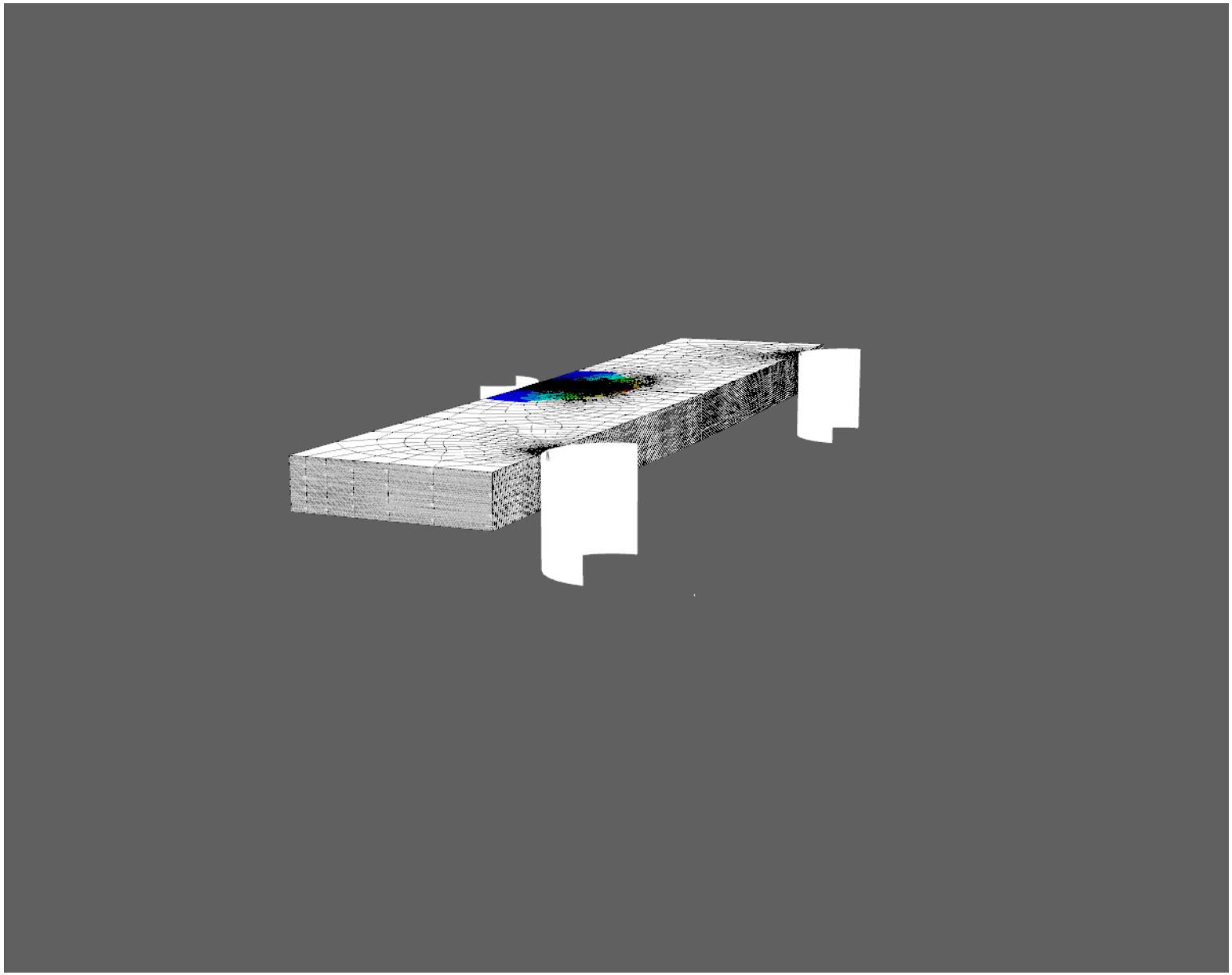

STRESS TRIAXIALITY

Model: Bx2B
Just before first failure.

Legend:

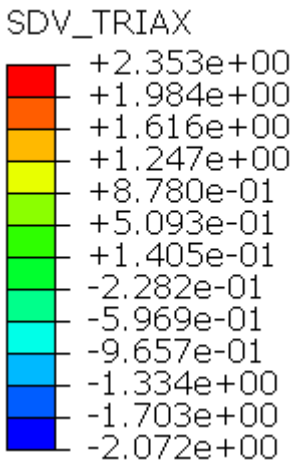

White elements have no value and are outside the subroutine domain.

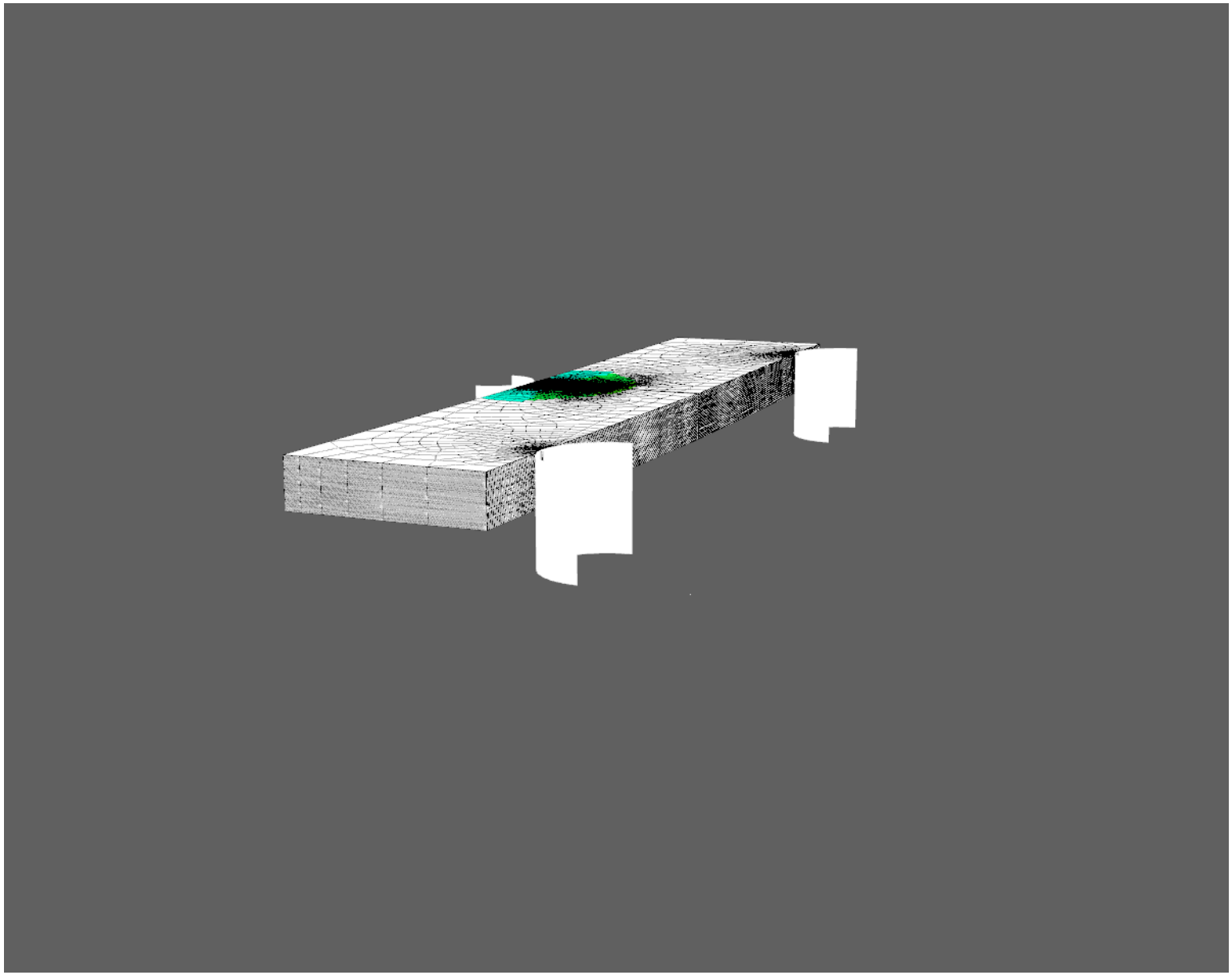

LODE ANGLE

Model: BxB
Just before first failure.

Legend:

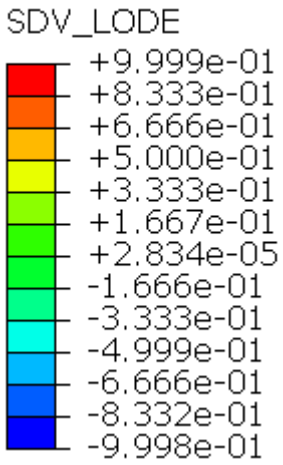

White elements have no value and are outside the subroutine domain.

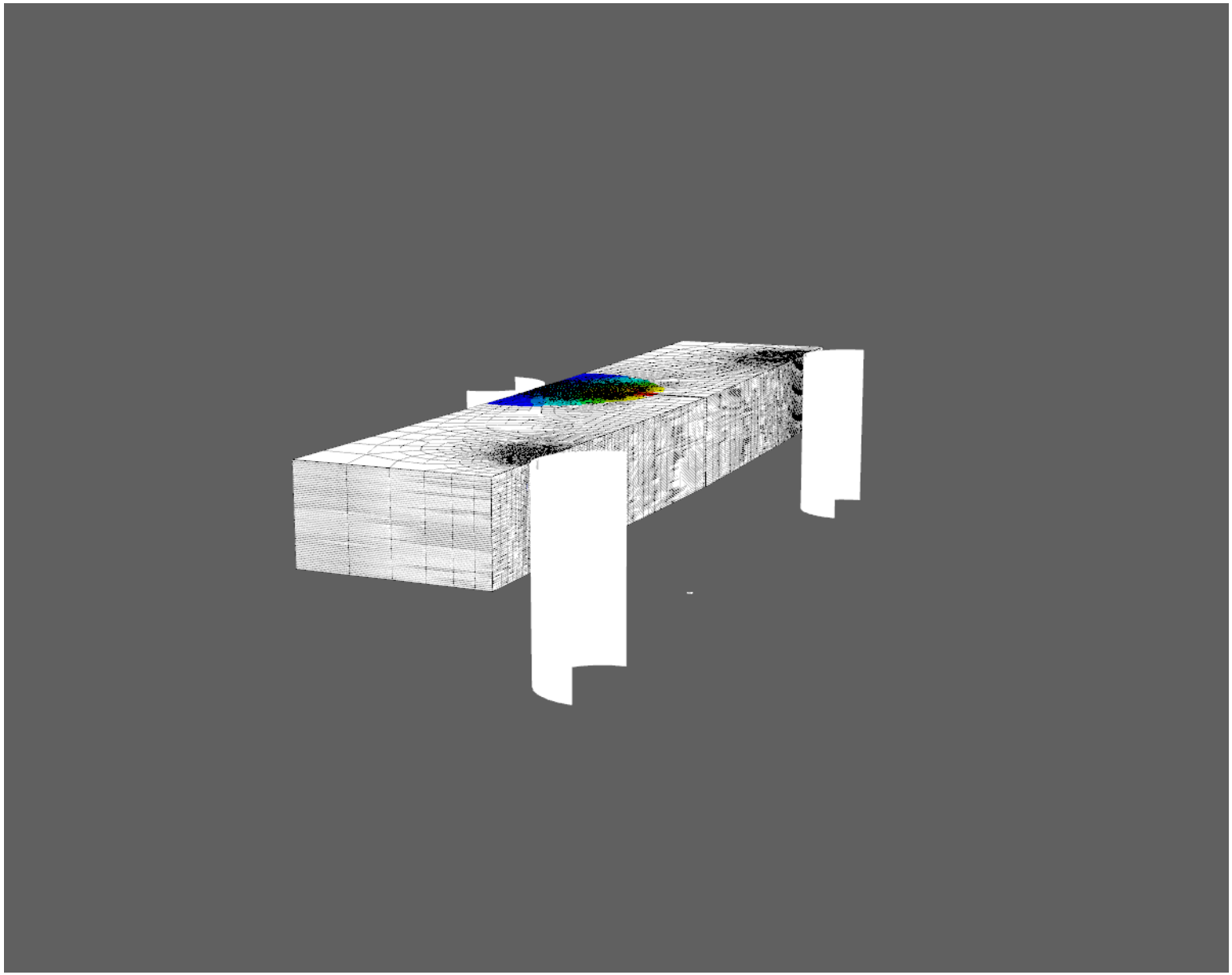

STRESS TRIAXIALITY

Model: BxB
Just before first failure.

Legend:

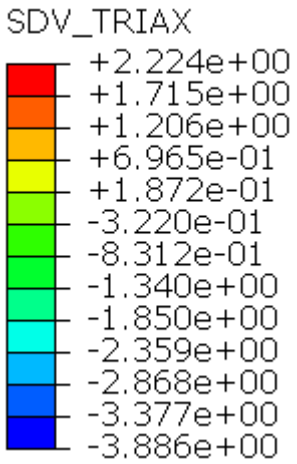

White elements have no value and are outside the subroutine domain.

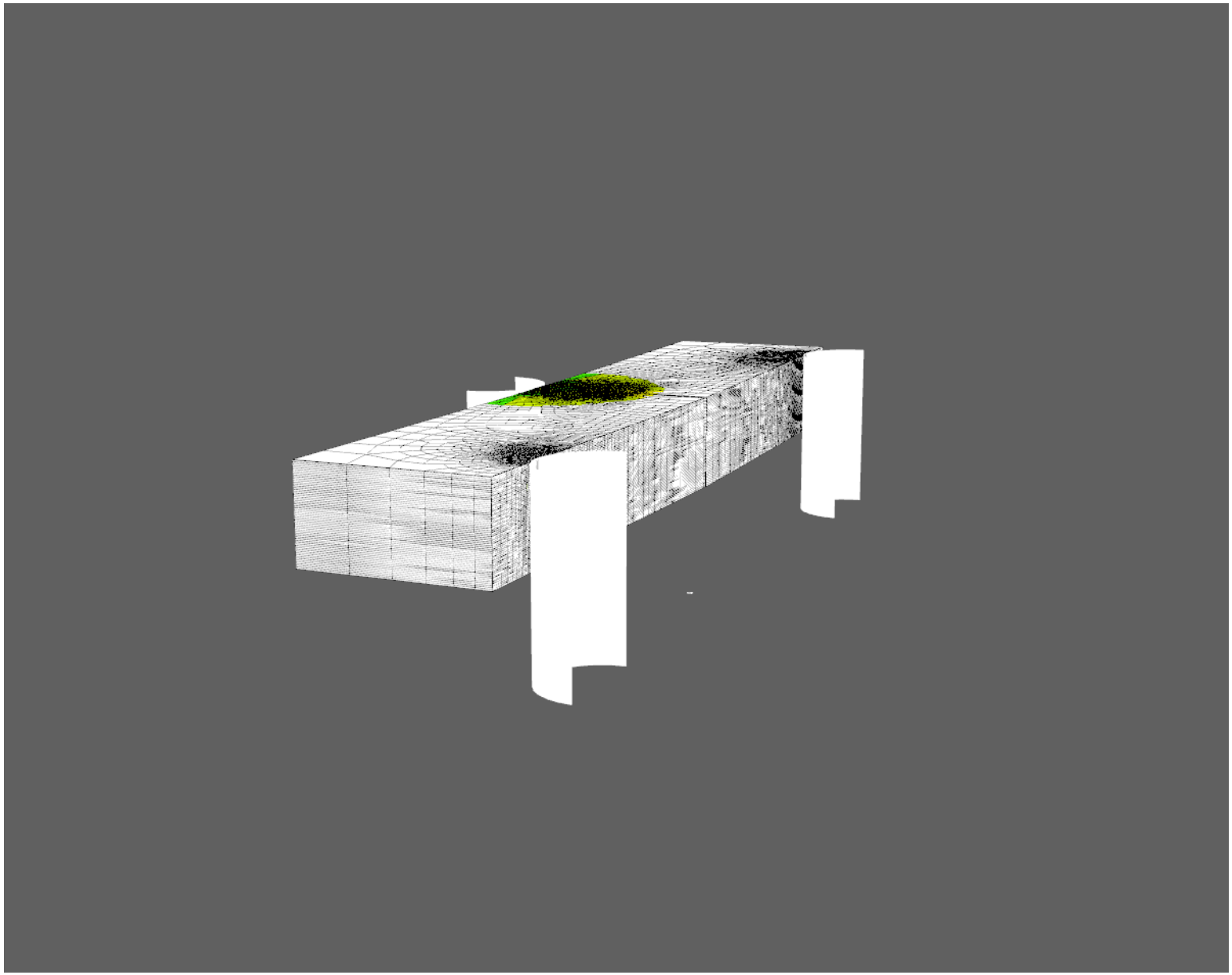

LODE ANGLE

Model: Bx2B proportional
Just before first failure.

Legend:

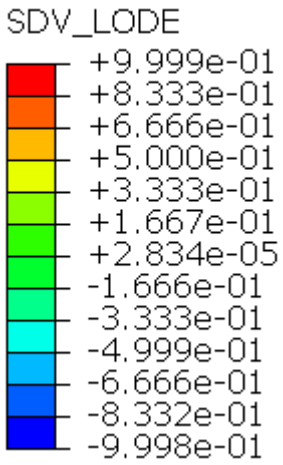

White elements have no value and are outside the subroutine domain.

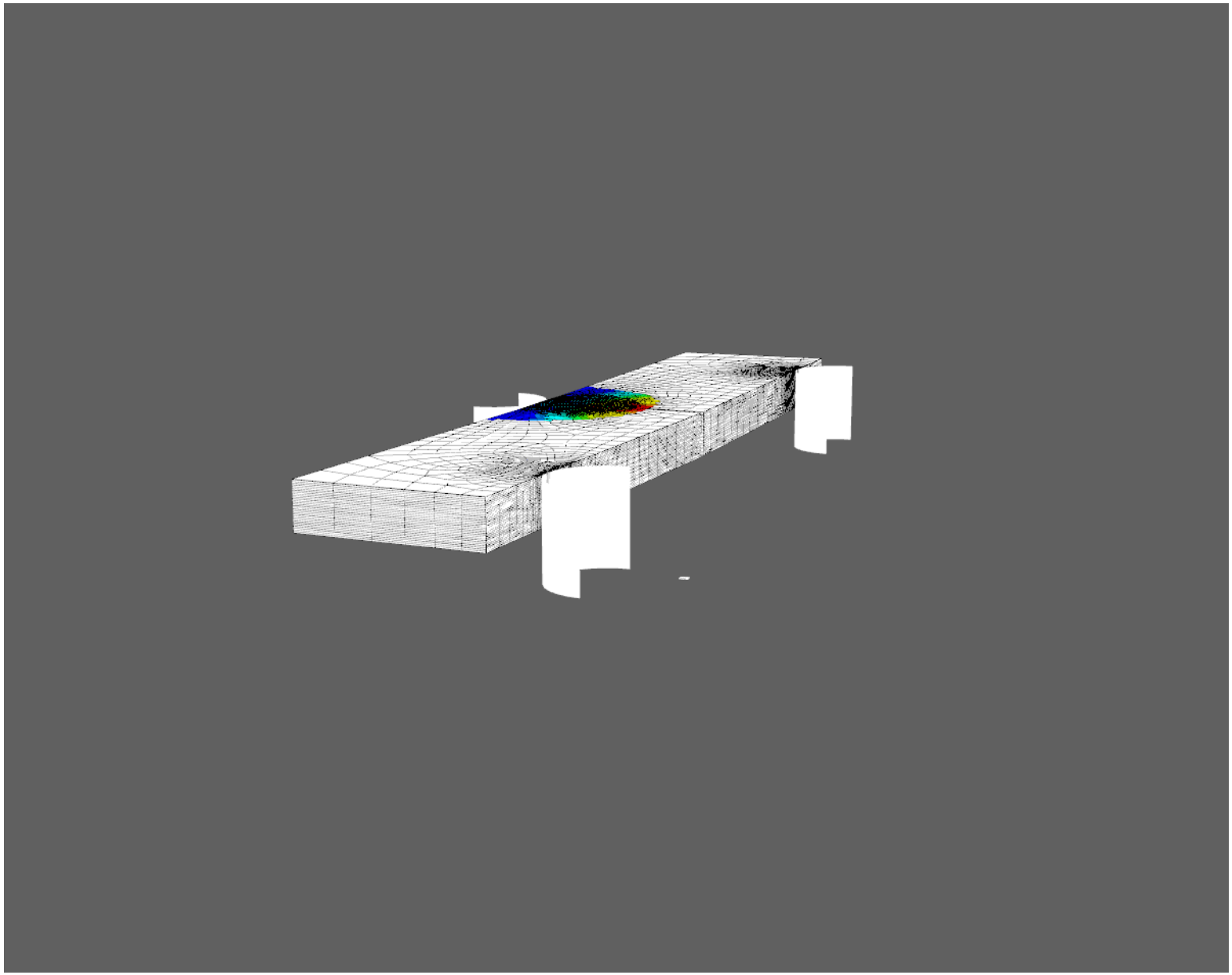

STRESS TRIAXIALITY

Model: Bx2B proportional
Just before first failure.

Legend:

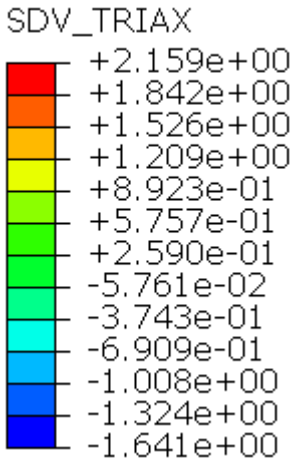

White elements have no value and are outside the subroutine domain.

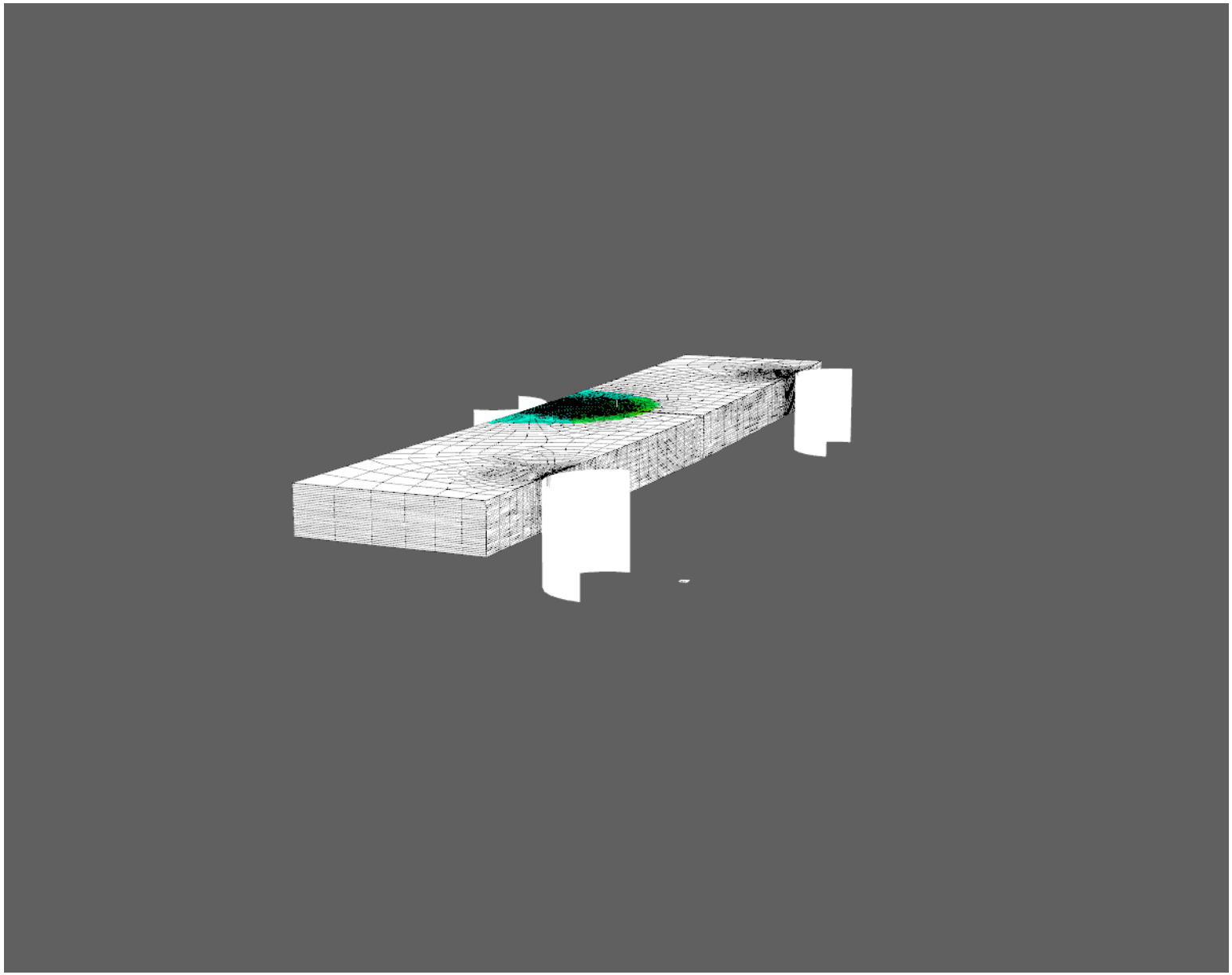

DAMAGE

Model: Bx2B
CMOD=6.24mm.

Legend:

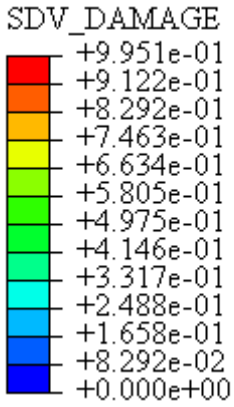

White elements have no value and are outside the subroutine domain.

All fully damaged elements are hidden from view.

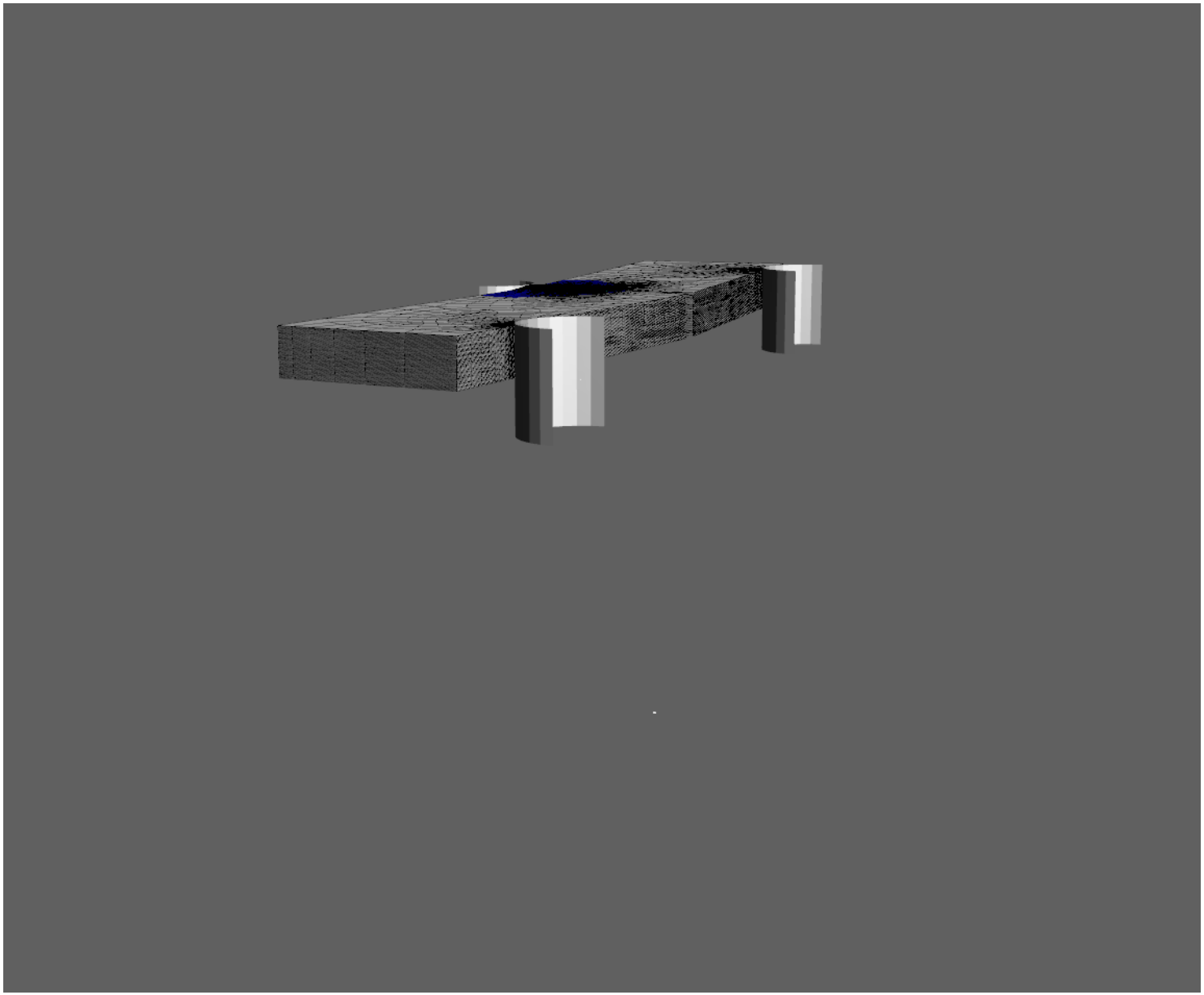

EQUIVALENT PLASTIC STRA

Model: Bx2B
CMOD=6.24mm.

Legend:

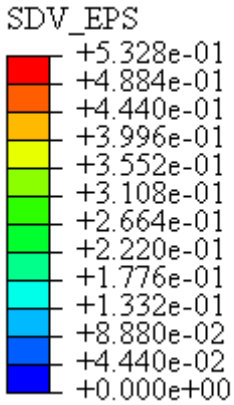

White elements have no value and are outside the subroutine domain.

All fully damaged elements are hidden from view.

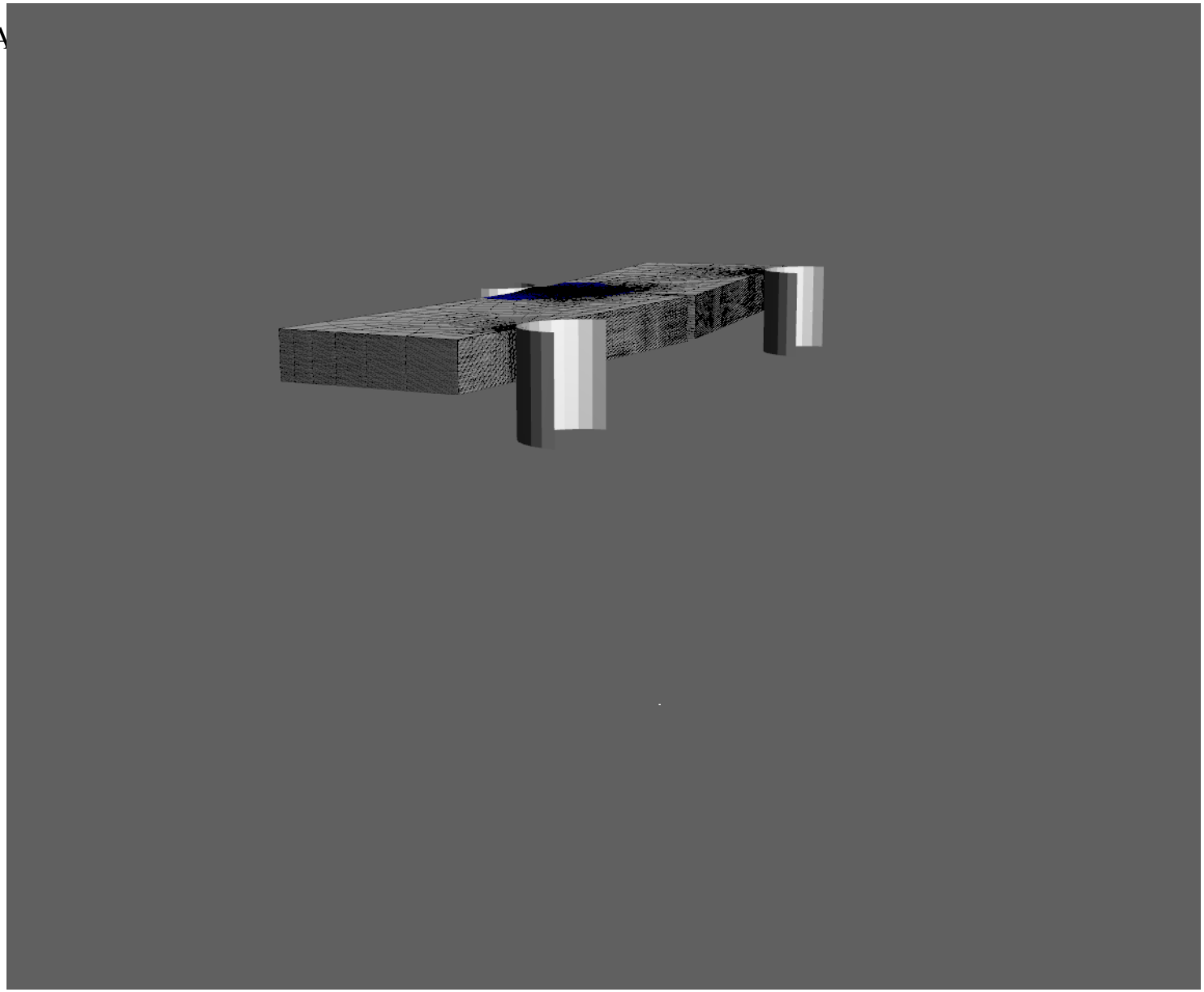

LODE ANGLE

Model: Bx2B
CMOD=6.24mm.

Legend:

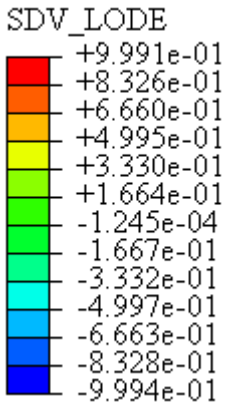

White elements have no value and are outside the subroutine domain.

All fully damaged elements are hidden from view.

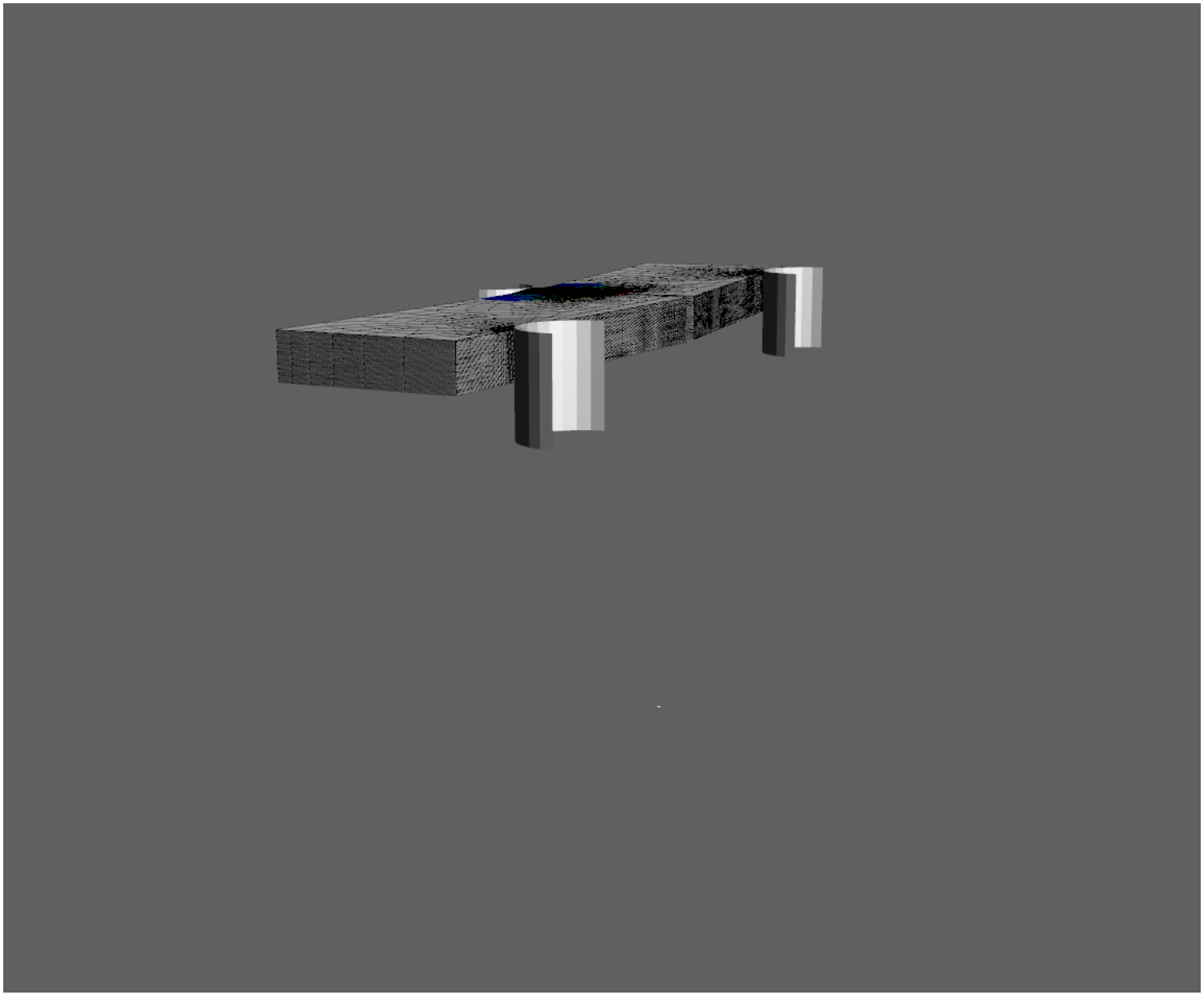

VON MISES STRESS

Model: Bx2B
CMOD=6.24mm.

Legend:

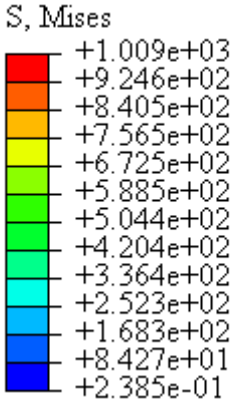

White elements have no value and are outside the subroutine domain.

All fully damaged elements are hidden from view.

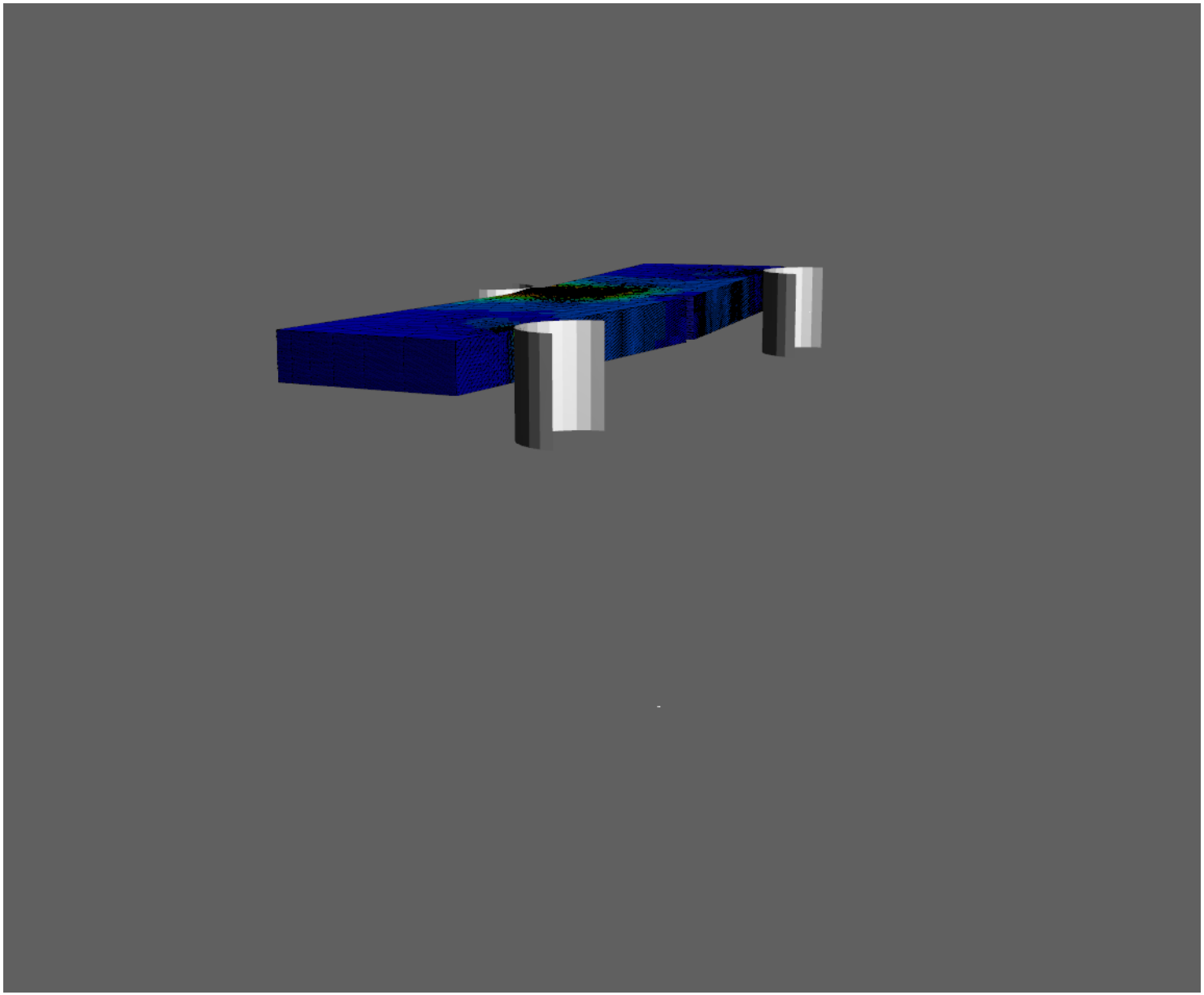

STRESS TRIAXIALITY

Model: Bx2B
CMOD=6.24mm.

Legend:

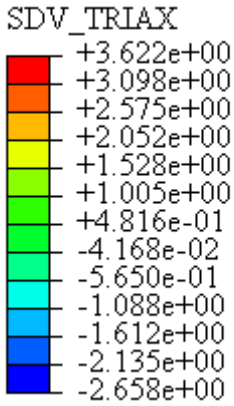

White elements have no value and are outside the subroutine domain.

All fully damaged elements are hidden from view.